Methods[1]

R. Tada, R.W. Murray, C.A. Alvarez Zarikian, W.T. Anderson Jr., M.-A. Bassetti, B.J. Brace, S.C. Clemens, M.H. da Costa Gurgel, G.R. Dickens, A.G. Dunlea, S.J. Gallagher, L. Giosan, A.C.G. Henderson, A.E. Holbourn, K. Ikehara, T. Irino, T. Itaki, A. Karasuda, C.W. Kinsley, Y. Kubota, G.S. Lee, K.E. Lee, J. Lofi, C.I.C.D. Lopes, L.C. Peterson, M. Saavedra-Pellitero, T. Sagawa, R.K. Singh, S. Sugisaki, S. Toucanne, S. Wan, C. Xuan, H. Zheng, and M. Ziegler[2]

Chapter contents

[1]Tada, R., Murray, R.W., Alvarez Zarikian, C.A., Anderson, W.T., Jr., Bassetti, M.-A., Brace, B.J., Clemens, S.C., da Costa Gurgel, M.H., Dickens, G.R., Dunlea, A.G., Gallagher, S.J., Giosan, L., Henderson, A.C.G., Holbourn, A.E., Ikehara, K., Irino, T., Itaki, T., Karasuda, A., Kinsley, C.W., Kubota, Y., Lee, G.S., Lee, K.E., Lofi, J., Lopes, C.I.C.D., Peterson, L.C., Saavedra-Pellitero, M., Sagawa, T., Singh, R.K., Sugisaki, S., Toucanne, S., Wan, S., Xuan, C., Zheng, H., and Ziegler, M., 2015. Methods. *In* Tada, R., Murray, R.W., Alvarez Zarikian, C.A., and the Expedition 346 Scientists, *Proc. IODP,* 346: College Station, TX (Integrated Ocean Drilling Program). doi:10.2204/iodp.proc.346.102.2015
[2]**Expedition 346 Scientists' addresses.**

Introduction, background, and operations

This chapter documents the procedures and methods employed in the various shipboard laboratories of the drillship R/V *JOIDES Resolution* during Integrated Ocean Drilling Program (IODP) Expedition 346. This information applies only to shipboard work described in the Expedition Reports section of the Expedition 346 *Proceedings of the Integrated Ocean Drilling Program* volume. Methods used by investigators for shore-based analyses of Expedition 346 data will be described in separate individual publications. This introductory section provides an overview of operations, curatorial conventions, depth scale terminology, and general core handling and analyses.

Authorship of the site chapters

All shipboard scientists contributed to this volume. However, certain sections were written primarily by discipline-based groups of scientists as listed below (authors are listed in alphabetical order; no seniority is implied):

Background and objectives: R.W. Murray, R. Tada
Operations: C.A. Alvarez Zarikian, M. Storms
Lithostratigraphy: M.-A. Bassetti, A.C.G. Henderson, K. Ikehara, A. Karasuda, L.C. Peterson, T. Sagawa, S. Toucanne, S. Wan, H. Zheng, M. Ziegler
Biostratigraphy: C.A. Alvarez Zarikian, B.J. Brace, S.J. Gallagher, A.E. Holbourn, T. Itaki, Y. Kubota, C.I.C.D. Lopes, M. Saavedra-Pellitero, R.K. Singh
Geochemistry: W.T. Anderson Jr., M.H. da Costa Gurgel, J. Dickens, A.G. Dunlea, C.W. Kinsley, K.E. Lee
Physical properties: L. Giosan, G.S. Lee
Paleomagnetism: S. Sugisaki, C. Xuan
Downhole measurements: J. Lofi
Stratigraphic correlation and sedimentation rates: S.C. Clemens, T. Irino

Site locations

GPS coordinates from precruise site surveys were used to position the vessel at all Expedition 346 sites. A Syquest Bathy 2010 CHIRP subbottom profiler was used to monitor seafloor depth on the approach to each site to reconfirm the depth profiles from precruise

doi:10.2204/iodp.proc.346.102.2015

surveys. Once the vessel was positioned at a site, the thrusters were lowered and a positioning beacon was dropped to the seafloor. The dynamic positioning control of the vessel used navigational input from the GPS system and triangulation to the seafloor beacon, weighted by the estimated positional accuracy. The final position for each hole of a given site was the mean position calculated from the GPS data collected over a significant portion of the time the hole was occupied. An inspection of the seafloor using the underwater camera system was conducted at IODP Sites U1428 and U1429 to ensure that they were free of obstructions (submarine cables, fishing lines, etc.) before the start of coring operations.

Coring and drilling operations

The full and half advanced piston corer (APC) systems and the extended core barrel (XCB) system were used during Expedition 346. Multiple holes were drilled at all sites to build a composite depth scale and a stratigraphic splice for continuous sampling after the cruise (see **"Sample depth calculations"** and **"Stratigraphic correlation and sedimentation rates"**).

The APC cuts soft-sediment cores with minimal coring disturbance relative to other IODP coring systems. After the APC core barrel is lowered through the drill pipe and lands near the bit, the drill pipe is pressured up until one or two shear pins that hold the inner barrel attached to the outer barrel fail. The inner barrel then advances rapidly ("fires") into the formation and cuts the core. The driller can detect a successful cut, or "full stroke," from the pressure gauge on the rig floor.

The depth limit of the APC, often referred to as APC refusal, is indicated in two ways: (1) the piston consistently fails to achieve a complete stroke (as determined from the pump pressure reading) because the formation is too hard and limited core recovery is achieved or (2) excessive force (>60,000 lb; ~267 kN as an example) is required to pull the core barrel out of the formation. When a full stroke could not be achieved, one or more additional attempts were typically made, and each time the bit was advanced by the length of recovered core. Note that this resulted in a nominal recovery of ~100% based on the assumption that the barrel penetrated the formation by the length of core recovered. During Expedition 346, there were a number of partial strokes that still returned nearly full core liners. In these cases, the partial strokes were not viewed as refusal and additional full APC cores were attempted. When a full or partial stroke was achieved but excessive force could not retrieve the barrel, the core barrel was sometimes "drilled over," meaning after the inner core barrel was successfully shot into the formation, the drill bit was advanced to total depth to free the APC barrel.

The standard (full) APC system contains a 9.5 m long core barrel. In addition to this standard 9.5 m APC system, Expedition 346 used the newly engineered half APC coring system extensively. The half APC system uses a 4.7 m long core barrel. In most instances, the half APC was deployed after the full APC reached refusal. During use of the half APC, the same criteria were applied in terms of refusal as for the full APC system. Use of this new technology allowed for significantly greater continuous APC sampling depths to be attained than would have otherwise been possible without this system. For example, the half APC enabled us to recover the deepest piston core in Deep Sea Drilling Project (DSDP)/Ocean Drilling Program (ODP)/IODP history (Core 346-U1427A-81H from 486.5 to 490.4 m core depth below seafloor, Method A [CSF-A]). This achievement was also the deepest continuously recovered piston cored sequence, initiated at the seafloor and penetrating 490.4 m solely by piston coring (see **"Operations"** in the "Site U1427" chapter [Tada et al., 2015c]).

Nonmagnetic core barrels were used during all full and half APC deployments. Orientation using the FlexIT tool (see **"Paleomagnetism"**) was used on standard 9.5 m APC cores, taken most commonly in the earliest deep hole of each site. Formation temperature measurements were made to obtain temperature gradients and heat flow estimates using the third-generation advanced piston corer temperature tool (APCT-3) (see **"Downhole measurements"**).

The XCB system was used to advance the hole when half APC refusal occurred before the target depth was reached. The XCB is a rotary system with a small cutting shoe that extends below the large rotary APC/XCB bit. The smaller bit can cut a semi-indurated core with less torque and fluid circulation than the main bit, optimizing recovery. The XCB cutting shoe (bit) extends ~30.5 cm ahead of the main bit in soft sediment but retracts into the main bit when hard formations are encountered. The XCB core barrels are 9.5 m long.

The bottom-hole assembly (BHA) is the lowermost part of the drill string. A typical APC/XCB BHA consists of a drill bit (outer diameter = 11 7/16 inch), a bit sub, a seal bore drill collar, a landing saver sub, a modified top sub, a modified head sub, a nonmagnetic drill collar (for APC/XCB), a number of 8 inch (~20.32 cm) drill collars, a tapered drill collar, six joints (two stands) of 5½ inch (~13.97 cm) drill pipe,

and one crossover sub. A lockable flapper valve was used to enable collection of downhole logs without dropping the bit when APC/XCB coring.

The rotary core barrel (RCB) system was not deployed during Expedition 346.

Drilling disturbance

Cores may be significantly disturbed as a result of the drilling process and contain extraneous material as a result of the coring and core handling process. In formations with loose layers, material from intervals higher in the borehole may be washed down by drilling circulation, accumulate at the bottom of the hole, and be sampled with the next core. The uppermost 10–50 cm of each core must therefore be examined critically during description for potential "cave-in." Common coring-induced deformation includes the concave-downward appearance of originally horizontal bedding. Piston action may result in fluidization (flow-in) at the bottom of APC cores. Retrieval from depth to the surface may result in elastic rebound. Gas that is in solution at depth may become free and drive core segments within the liner apart. When gas content is high, as was the case at many of the sites drilled during Expedition 346, pressure must be relieved for safety reasons before the cores are cut into segments. This is accomplished by drilling holes into the liner, which forces some sediment as well as gas out of the liner. After gas was released, segmented sediments were slid back together with a mechanical pusher to close voids. This procedure may affect physical properties. Drilling disturbances are described in the "Lithostratigraphy" sections in each site chapter and are graphically indicated on the core summary graphic reports.

Core handling

Cores recovered during Expedition 346 were extracted from the core barrel in plastic liners. Except for when a series of cores were recovered for optically stimulated luminescence (OSL) dating (IODP Sites U1424 and U1425), core liners were carried from the rig floor to the core processing area on the catwalk outside the Core Laboratory and cut into ~1.5 m long sections. The exact section length was noted and later entered into the database as "created length" using the Sample Master application. This number was used to calculate recovery. Headspace samples were taken from selected section ends (at least one per core) using a syringe for immediate hydrocarbon analysis as part of the shipboard safety and pollution prevention program. Similarly, microbiology samples were taken immediately after the core was sectioned. Whole-round samples for interstitial water were cut on the catwalk. Core catcher samples were taken for biostratigraphic analysis. When catwalk sampling was complete, liner caps (blue = top; colorless = bottom; yellow = bottom; whole-round cut) were glued with acetone onto liner sections, and the sections were placed in core racks in the laboratory for analysis.

Sampling for optical dating of sediment using OSL was conducted in Holes U1424C and U1425C and involved special core handling procedures. Dedicated holes for OSL studies were planned intentionally to be cored during the night to minimize the core's exposure to light. Cores were cut into 1.5 m whole-round sections directly on the drill floor. Then, in sequence as the core was pulled out of the core barrel, the whole rounds were placed into 1.5 m long precut opaque aluminum-lined pouches, labeled, sealed, and stored in the refrigerated core storage.

Curatorial procedures

The numbering of sites, holes, cores, and samples followed standard IODP procedure. A full curatorial sample identifier consists of the following information: expedition, site, hole, core number, core type, section number, and offset in centimeters measured from the top of a given section. For example, a sample identification of "346-U1425A-1H-2, 10–12 cm," represents a sample taken from the interval between 10 and 12 cm below the top of Section 2 of Core 1 ("H" designates that this core was taken with the APC system and "X" designates XCB cores) of Hole A of Site U1425 during Expedition 346. The "U" preceding the hole number indicates that the hole was drilled by the United States Implementing Organization (USIO) platform, the *JOIDES Resolution*. Half APC cores were also given the "H" designation, and the usage of the half APC system was noted in the core tech summary sheet by the drillers.

Shipboard core analysis

Whole-round core sections were immediately run through the Special Task Multisensor Logger (STMSL) after being cut on the catwalk. The STMSL measures density and magnetic susceptibility at a 5 cm resolution and is used to aid in real-time stratigraphic correlation. The whole-round core sections were run through the Whole-Round Multisensor Logger (WRMSL; measuring *P*-wave velocity, density, and magnetic susceptibility) and the Natural Gamma Radiation Logger (NGRL) (see **"Physical properties"**). For most of Expedition 346, we ran all cores through the whole-round core loggers only once, prior to thermal equilibrium. We studied the effect of tem-

perature on the gamma ray attenuation (GRA) and magnetic susceptibility measurements and found it to be negligible.

Core sections were allowed to reach equilibrium with laboratory temperature (after ~4 h) prior to being split. Each section from a given core was split lengthwise from bottom to top into working ("W") and archive ("A") halves. Investigators should note that older material might have been transported upward on the split face of each section during splitting. As part of the measurements plan for each site, the working half of each section was run on the physical properties gantry, which includes the *P*-wave caliper and vane shear, prior to being sampled for shipboard analysis (biostratigraphy, physical properties, geochemistry, and bulk X-ray diffraction [XRD] mineralogy). The archive half of each section for each core was scanned on the Section Half Imaging Logger (SHIL) and measured for color reflectance and magnetic susceptibility on the Section Half Multisensor Logger (SHMSL). At the same time, the archive halves were described macroscopically as well as microscopically by means of smear slides. Finally, the archive halves were run through the cryogenic magnetometer. Both halves of the core were then put into labeled plastic tubes that were sealed and transferred to cold storage space aboard the ship.

At the end of the expedition, all archive and working halves were transported from the ship to permanent cold storage at the IODP core repository at Kochi University, in Kochi, Japan.

Sample depth calculations

The primary depth scale types are based on the measurement of the drill string length deployed beneath the rig floor (drilling depth below rig floor [DRF] and drilling depth below seafloor [DSF]), the length of each core recovered (core depth below seafloor [CSF] and core composite depth below seafloor [CCSF]), and the length of the logging wireline deployed (wireline log depth below rig floor [WRF], wireline log depth below seafloor [WSF], and wireline log matched depth below seafloor [WMSF]). All units are in meters. Depths of samples and measurements are calculated at the applicable depth scale either by fixed protocol (e.g., CSF) or by combinations of protocols with user-defined correlations (e.g., CCSF). The definition of these depth scale types, and the distinction in nomenclature, should keep the user aware that a nominal depth value at two different depth scale types usually does not refer to exactly the same stratigraphic interval in a hole (see **"Stratigraphic correlation and sedimentation rates"** for detailed information).

Depths of cored intervals are measured from the drill floor based on the length of drill pipe deployed beneath the rig floor (DRF scale). The depth of the cored interval is referenced to the seafloor (DSF scale) by subtracting the seafloor depth at the time of the first hole from the DRF depth of the interval. In most cases, the seafloor depth is the length of pipe deployed minus the length of the mudline core recovered. However, some of the seafloor depths were determined by offset from a previous known measurement of depth, or by tagging the seafloor with the camera system in place.

Standard depths of cores in meters below the seafloor (CSF-A scale) are determined based on the assumption that (1) the top depth of a recovered core corresponds to the top depth of its cored interval (at DSF scale) and (2) the recovered material is a contiguous section even if core segments are separated by voids when recovered. Voids in the core are closed by pushing core segments together, if possible, during core handling. This convention is also applied if a core has incomplete recovery, in which case the true position of the core within the cored interval is unknown and should be considered a sample depth uncertainty, up to the length of the core barrel used, when analyzing data associated with the core material. Standard depths of samples and associated measurements (CSF-A scale) are calculated by adding the offset of the sample or measurement from the top of its section, and the lengths of all higher sections in the core, to the top depth of the cored interval.

A soft to semisoft sediment core from less than a few hundred meters below seafloor expands upon recovery (typically a few percent to as much as 15%), so the length of the recovered core exceeds that of the cored interval. Therefore, a stratigraphic interval may not have the same nominal depth at the DSF and CSF scales in the same hole. When core recovery (the ratio of recovered core to cored interval times 100%) is >100%, the CSF depth of a sample taken from the bottom of a core will be deeper than that of a sample from the top of the subsequent core (i.e., the data associated with the two core intervals overlap at the CSF-A scale).

Core composite depth scales (CCSF) are constructed for all sites drilled during Expedition 346 to mitigate the CSF-A core overlap or coring gap problems and to create as continuous a stratigraphic record as possible. Using shipboard core logger–based physical property data, verified with core photos, core depths in adjacent holes at a site are vertically shifted to correlate between cores recovered in adjacent holes. This process produces the CCSF-A depth scale. The

correlation process results in affine tables, indicating the vertical shift of cores at the CCSF scale relative to the CSF-A scale. Once the CCSF scale is constructed, a splice can be defined that best represents the stratigraphy of a site by utilizing and splicing the best portions of individual sections and cores from each hole at a site. This process produces the CCSF-D depth scale, which is strictly correct only along the splice. Because of core expansion, the CCSF-A/CCSF-D depths of stratigraphic intervals are typically 10%–15% deeper than their CSF-A depths. CCSF-A construction also reveals that coring gaps on the order of 1–1.5 m may occur between two subsequent cores, despite the apparent >100% recovery.

Lithostratigraphy

The primary lithostratigraphic procedures used during Expedition 346 include visual core description, sediment classification, digital color imaging, XRD, and smear slide description. Color spectrophotometry and point source magnetic susceptibility data acquired prior to core description are described in detail in **"Physical properties."** Carbonate, organic matter (CHNS analysis), and geochemical measurements are described in detail in **"Geochemistry."**

Core preparation

The standard method of splitting cores into working and archive halves (either using a piano wire or a saw) can affect the appearance of the split-core surface and obscure fine details of lithology and sedimentary structure. When necessary during Expedition 346, the archive halves of cores were gently scraped across, rather than along, the core section using a stainless steel or glass scraper to prepare the surface for unobscured sedimentologic examination and digital imaging. Scraping parallel to bedding with a freshly cleaned tool prevented cross-stratigraphic contamination. Cleaned sections were then described in conjunction with measurements using the SHIL, discussed below, and SHMSL (see **"Physical properties"**).

Lithologic classification scheme

Sediments recovered during Expedition 346 are composed of biogenic, siliciclastic, and volcaniclastic components. They were described using a classification scheme derived from those of ODP Leg 155 (Shipboard Scientific Party, 1995), IODP Expedition 303 (Expedition 303 Scientists, 2006), IODP Expedition 339 (Expedition 339 Scientists, 2013), and Stow (2005). The biogenic component is composed of the skeletal debris of calcareous and siliceous microfauna (e.g., foraminifers and radiolarians), microflora (e.g., calcareous nannofossils, diatoms, and silicoflagellates), and macrofossil shell fragments. The siliciclastic component is composed of mineral and rock grains derived from igneous, sedimentary, and metamorphic rocks. The volcaniclastic fraction ranges from rock fragments to fine-grained tephra derived from volcanic sources. The relative proportion of these three components is used to define the major classes of sediments in this scheme (Fig. **F1**).

Sediment nomenclature for Expedition 346 follows the general guidelines of the ODP sediment classification scheme (Mazzullo et al., 1988), with the exception that a separate "mixed sediment" category was not used during Expedition 346. As a result, biogenic sediments are those that contain >50% biogenic grains and <50% siliciclastic/volcaniclastic grains, whereas siliciclastic/volcaniclastic sediments are those that contain >50% siliciclastic/volcaniclastic grains and <50% biogenic grains. During Expedition 346, no shallow-water biogenic materials were encountered except as accessory components; therefore, these categories are not addressed below. Sediment grain-size divisions for the siliciclastic and volcaniclastic components are based on Wentworth (1922), with nine major textural categories defined on the basis of the relative proportions of sand-, silt-, and clay-sized particles (Fig. **F2**), which are slightly modified from that of Expeditions 303 (Expedition 303 Scientists, 2006) and 339 (Expedition 339 Scientists, 2013). The term "clay" is only used to describe particle size and is applied to both clay minerals and all other clastic grains <4 µm in size. Size-textural qualifiers were not used for biogenic sediment names (e.g., nannofossil clay implies that the dominant component is detrital clay rather than clay-sized nannofossils).

The lithologic names assigned to these sediments consist of a principal name and modifiers based on composition and degree of lithification and/or texture as determined from visual description of the cores and from smear slide observations. For sediment that contains >90% of one component (either the siliciclastic/volcaniclastic or biogenic component), only the principal name is used. For sediment with >90% siliciclastic components, the principal name is based on the textural characteristics of all sediment particles. For sediment with >90% volcaniclastic components, the name describes the texture as follows (Fisher and Schmincke, 1984):

- Volcanic breccia: sediment composed of pyroclasts >64 mm in diameter.
- Volcanic lapilli: sediment composed of pyroclasts between 2 and 64 mm in diameter.

- Volcanic ash: sediment composed of pyroclasts <2 mm in diameter.

During Expedition 346, volcanic breccia and volcanic lapilli were not encountered except as accessory components, and the term "tephra" was used in place of volcanic ash.

For sediment containing a greater proportion of siliciclastic grains than volcaniclastic grains and >10% volcaniclastic grains, the principal name is based on the textural characteristics of all sediment particles, with volcaniclastic components as major (25%–50%) or minor (10%–25%) modifiers (Fig. F3). For example, sediment composed of 80% detrital silty clay and 20% volcanic ash is called "silty clay with tephra," and sediment composed of 70% detrital sandy silt and 30% volcanic ash is called "tephra-rich sandy silt." For sediment containing a higher proportion of volcaniclastic grains than siliciclastic grains, the principal name is based on the texture of volcaniclastic grains with major or minor modifiers indicating the textural characteristics of all sediment particles. For example, sediment composed of 80% volcanic ash and 20% detrital silt is called "tephra with silt," and sediment composed of 70% volcanic ash and 30% detrital silt is called "silty tephra." For sediment with >90% biogenic components, the name applied indicates the most limited group of grains that exceed the 90% threshold value. For example, sediment composed of >90% calcareous nannofossils is called "nannofossil ooze," sediment composed of 50% foraminifers and 45% calcareous nannofossils is called "calcareous ooze," and sediment composed of 40% foraminifers, 40% calcareous nannofossils, and 15% diatoms is called "calcareous ooze with diatoms" (Fig. F1).

For sediment that contains a significant mixture of siliciclastic/volcaniclastic and biogenic components (between 25% and 75% of both siliciclastic/volcaniclastic and biogenic components), the principal name is determined by the most abundant component. If the siliciclastic component is more abundant, the principal name is based on the textural characteristics of all sediment particles (both siliciclastic/volcaniclastic and biogenic) (Fig. F1). If the volcaniclastic component is more abundant, the principal name is based on the textural characteristics of the volcaniclastic grains. If the biogenic component is more abundant, the principal name is either (1) based on the predominant biogenic component if that component forms >75% of the biogenic particles or (2) the more encompassing term "biogenic ooze."

If one component forms 75%–90% of the sediment, then the principal name is followed by a minor modifier (e.g., "with diatoms"), with the minor modifier based on the most abundant component that forms 10%–25% of the sediment. If the minor component is biogenic, then the modifier describes the most limited group of grains that exceeds the 10% abundance threshold. If the minor component is siliciclastic, the minor modifier is based on the texture of the siliciclastic fraction.

If one component forms 50%–75% of the sediment, then the principal name is preceded by a major modifier that is based on the component that forms 25%–50% of the sediment. If the less abundant component is biogenic, then the major modifier describes the most limited group of grains that exceeds the 25% abundance threshold (e.g., nannofossil versus calcareous versus biogenic). If the less abundant component is siliciclastic, the major modifier is based on the texture of the siliciclastic fraction.

The following terms describe lithification that varies depending on the dominant composition:

- Sediment composed predominantly of calcareous, pelagic organisms (e.g., calcareous nannofossils and foraminifers):
  - Ooze: sediment can be deformed with a finger.
  - Chalk: sediment cannot be easily deformed manually.
- Sediment composed predominantly of siliceous microfossils (diatoms, radiolarians, and siliceous sponge spicules):
  - Ooze: sediment can be deformed with a finger.
  - Diatomite/Radiolarite/Spiculite: sediment cannot be easily deformed manually.
- Sediment composed of a mixture of calcareous pelagic organisms and siliceous microfossils and sediment composed of a mixture of siliceous microfossils:
  - Ooze: sediment can be deformed with a finger.
  - Indurated sediment: sediment cannot be easily deformed manually.
- Sediment composed predominantly of siliciclastic material:
  - If the sediment can be deformed easily with a finger, no lithification term is added and the sediment is named for the dominant grain size (i.e., sand, silt, or clay).
  - "-stone" suffix: more consolidated material, (e.g., claystone).
- Sediment composed of sand-sized volcaniclastic grains:
  - Tephra layer: sediment can be deformed easily with a finger.
  - Tuff: more consolidated material.

Sediment compositions are indicated in the Graphic lithology column of the visual core description (VCD) sheets using the lithologic patterns found in

Figure F4. If the primary lithology for an interval of core has a major modifier, then the graphic symbol used reflects both the major modifier and principal sediment name. The minor modifiers of sediment lithologies are not included in the Graphic lithology column.

Visual core descriptions

VCD sheets provide a summary of the data obtained during shipboard analysis of each core (Fig. F5). Detailed observations of each section were recorded using the DESClogik software, which provides data that can be used in Strater to generate a simplified, annotated graphical description (VCD) for each core. Site, hole, and depth (in meters CSF-A; previously called meters below seafloor [mbsf]) are given at the top of the VCD sheet, with the corresponding depths of core sections along the left margin (depth acronyms follow the IODP Depth Scale Terminology [www.iodp.org/program-policies/procedures/guidelines/]). Columns on the VCD sheets include Lithologic unit, Core image, Graphic lithology, Tephra distribution, Coring disturbance intensity, Sedimentary structures, Lithological accessories, Bioturbation intensity, Shipboard samples, and Age. Profiles of GRA density, magnetic susceptibility, natural gamma radiation (NGR), and reflectance (L*, a*, and b*) are also included. These columns are discussed in more detail below.

Graphic lithology

Lithologies of the core intervals recovered are represented on the VCD sheets by graphic patterns in the Graphic lithology column, using the symbols illustrated in Figure F4. A maximum of two different lithologies (for interbedded sediments) can be represented within the same core interval. The major modifier of a primary lithology is shown using a modified version of the primary lithology pattern. A secondary lithology present as interbeds within the primary lithology is shown by a pattern along the right side of the column, with a solid vertical line dividing the primary and secondary lithologies. Lithologic abundances are rounded to the nearest 10%; lithologies that constitute <10% of the core are generally not shown but are listed in the written core description at the top of the VCD. However, some distinctive secondary lithologies, such as tephra layers, are included graphically in the Graphic lithology column as the primary lithology for a thin stratigraphic interval. Relative abundances of lithologies reported in this way are useful for general characterization of the sediment but do not constitute precise, quantitative observations.

Lithologic accessories

Lithologic, diagenetic, and paleontologic accessories, such as nodules, sulfides, and shells, are indicated on the VCD sheets. The symbols used to designate these features are shown in Figure F6. The following terminology was used to describe the abundance of lithologic accessories in written core descriptions:

Trace = 1 observed per section of core.
Rare = 2–10 observed per section of core.
Common = 10–20 observed per section of core.
Abundant = 20–50 observed per section of core.
Dominant = >50 observed per section of core.

Clasts

When clasts >2 mm were present, this was noted in core descriptions using the same abundance terminology as for lithologic accessories (e.g., trace, rare, common, abundant, and dominant). Where only holes or depressions caused by clasts were observed, the working half was also examined to better estimate clast abundance. Details on the lithology and shape of large lonestones and diamict clasts are provided on the written core descriptions and/or the DESClogik General interval comments column.

Tephra type

Occurrence of tephra layers is recorded in an additional column on the VCD sheets using the symbols shown in Figure F6. The type of tephra is defined visually and classified as

V = vitric (primarily volcanic glass shards).
P = pumice (white to yellowish pumice grains).
S = scoria (black–dark gray scoria grains).

Characteristics of tephra layers, such as grain size, color, and sedimentary structures and characteristics of their components, such as glass type (bubble-walled, pumice-walled, or fibrous), glass morphology, associated heavy minerals, and rock fragments, were recorded.

Bioturbation

Four levels of bioturbation are recognized using a scheme similar to that of Droser and Bottjer (1986). Bioturbation intensity is classified as

1 = none.
2 = slight.
3 = heavy.
4 = complete.

These levels are illustrated by numeric scale in the Bioturbation intensity column of the VCD sheet. Recognizable biogenic structures and trace fossils were additionally noted.

Stratification and sedimentary structures

The locations and types of stratification and sedimentary structures visible on the prepared surfaces of the split cores are shown in the Sedimentary structures column of the VCD sheet. Symbols in this column indicate the locations and scales of stratification, as well as the locations of individual bedding features and any other sedimentary features, such as scours, ripple laminations, and fining-upward, coarsening-upward, or bigradationally bedded intervals (Fig. F6).

In the written description, layers and bedding thickness were further described and classified following terminology based on Stow (2005):

Thin lamination = <3 mm thick.
Medium lamination = 0.3–0.6 cm thick.
Thick lamination = 0.6–1 cm thick.
Very thin bed = 1–3 cm thick.
Thin bed = 3–10 cm thick.
Medium bed = 10–30 cm thick.
Thick bed = 30–100 cm thick.
Very thick bed = >100 cm thick.

Descriptive terms for bed boundaries, such as sharp, erosive, gradual, irregular, and bioturbated, are noted in DESClogik.

Sediment disturbance

Core disturbance from the drilling process can impact the integrity of the stratigraphic sequence. Drilling disturbance, if any, is documented for both soft and firm sediment using the following classification scheme:

- Slightly disturbed: bedding contacts are slightly bent or bowed in a concave-downward appearance.
- Moderately disturbed: bedding is moderately deformed but probably still in the correct stratigraphic sequence.
- Heavily disturbed: sediment is completely deformed and may show no traces of original bedding or structure.

In addition to this first-order assessment of disturbance, a number of other terms (Fig. F6) may appear on the VCD to characterize drilling disturbance. Some of the more common types observed include

- Flow-in: soupy, displaced sediment pulled into the core liner during APC coring.
- Fall-in: downhole contamination resulting from loose material falling from the drill hole walls into the top of the core. The uppermost 10–15 cm of each core was inspected during description for potential fall-in.
- Bowed: bedding contacts are slightly to moderately deformed but still subhorizontal and continuous.
- Soupy or mousselike: intervals are water saturated and have lost all aspects of original bedding.
- Biscuit: sediment of intermediate stiffness shows vertical variations in the degree of disturbance. Softer intervals are washed and/or soupy, whereas firmer intervals are relatively undisturbed.
- Cracked or fractured: firm sediment is broken but not displaced or rotated significantly.
- Fragmented or brecciated: firm sediment is pervasively broken and may be displaced or rotated.

Shipboard samples

Sample material taken for shipboard sedimentologic and chemical analyses consisted of interstitial water whole rounds and Rhizon samples, microbiology whole rounds and syringes, micropaleontology samples, smear slides, discrete samples for XRD and carbonate analysis, and samples for physical properties (moisture and density [MAD]) and paleomagnetic studies. In addition, a micropaleontology sample was obtained from the core catcher of most cores. XRD samples for bulk analysis were routinely taken from Section 1 of each core adjacent to the paleomagnetic sample and at other levels of lithologic interest. Carbonate analyses were routinely taken from interstitial water squeeze cakes at the rate of two per core and at additional levels where requested. Thick (>1 cm) tephra layers were also sampled for the establishment of age models and correlations between holes and cores.

Color

During Expedition 346, the dominant sediment colors for each core are recorded in the summary at the top of the VCD sheets using standard Munsell color names (Munsell Color Company, Inc., 2009).

Remarks

The written description at the top of the VCD sheets for each core contains a summary of primary and secondary lithologies present, as well as notable features such as sedimentary structures, grading, and disturbances resulting from the coring process.

Smear slides

Smear slide samples were taken from archive halves during core description when there was either a major lithologic change or tephra layer. A small amount of sediment was removed with a wooden toothpick, dispersed evenly in deionized water on a 25 mm × 75

mm glass slide, and dried on a hot plate at a low setting. A drop of mounting medium (Norland Optical) and a 22 mm × 30 mm cover glass were added, and the slide was placed in an ultraviolet (UV) light box for ~15 min. Once fixed, each slide was scanned at 100×–200× with a transmitted light petrographic microscope using an eyepiece micrometer to assess grain-size distributions in clay (<4 µm), silt (4–63 µm), and sand (>63 µm) fractions. An eyepiece micrometer was calibrated once for each magnification and combination of ocular and objective, using an inscribed stage micrometer.

Relative abundance (percent) of each grain size and type was estimated by microscopic examination. Note that smear slide analyses tend to underestimate the abundance of sand-sized and larger grains (e.g., foraminifers, radiolarians, and siliciclastic/volcaniclastic sand) because these are difficult to incorporate into the smear. Biogenic silica, which is transparent and isotropic, can also be difficult to quantify. After scanning for grain-size distribution, several fields were examined at 200×–500× for mineralogic and microfossil identification.

Standard petrographic techniques were employed to identify commonly occurring minerals and biogenic groups, as well as important accessory minerals and microfossils. The smear slide analysis data worksheet used during these analyses is shown in (Fig. F7), and the data generated are included in the core descriptions. These tables provide information about the sample location, description of where the smear slide was taken, the estimated abundances of texture (i.e., sand, silt, and clay), and the relative composition of individual components in the sediment (i.e., tephra, siliciclastics, detrital carbonate, biogenic carbonate, and biogenic silica). Relative abundances of identified components such as mineral grains, microfossils, and biogenic fragments were assigned on a semiquantitative basis using the following abbreviations:

Tr = trace (<1% in field of view [FOV]).
R = rare (1%–5% in FOV).
C = common (5%–25% in FOV).
A = abundant (25%–75% in FOV).
D = dominant (>75% in FOV).

In addition, an assessment of fossil preservation was made using the following abbreviations:

P = poor.
M = moderate.
G = good.

Digital color imaging

The SHIL captures continuous high-resolution images of the archive-half surface for analysis and description. Images were collected shortly after core splitting and surface scraping in an effort to avoid color changes resulting from excessive sediment drying and oxidation of the surface. The shipboard system uses a commercial line-scan camera lens (AF Micro Nikon; 60 mm; 1:2.8 D), with illumination provided by a custom assembly of three pairs of LED strip lights that provide constant illumination over a range of surface elevations. Each LED pair has a color temperature of 6,500 K and emits 90,000 lux at 3 inches. The resolution of the line-scan camera was set at 20 pixels/mm. Available files include the original high-resolution TIFF image with a grayscale and ruler, as well as reduced JPEG images cropped to show only section-half surfaces. High-resolution color data (red, green, and blue) were acquired by digital color imaging.

X-ray diffraction analysis

Samples were prepared for XRD analysis in order to make qualitative to semiquantitative bulk mineral estimates. The XRD results combined with smear slide estimates and visual descriptions were used to assist in lithologic classification. In general, one 2.5 cm^3 sample was routinely taken for analysis in Section 1 of each core for APC samples or every two cores for half APC samples adjacent to the paleomagnetic sample. Additional limited samples were taken and analyzed based on visual core observations (e.g., color variability and visual changes in lithology and texture) and smear slides. Samples analyzed for bulk mineralogy were freeze-dried in the case of unlithified samples and ground by hand (soft sediment) or in an agate ball mill (rock), as necessary. Prepared samples were top-mounted onto a sample holder and analyzed using a Bruker D-4 Endeavor diffractometer mounted with a Vantec-1 detector using nickel-filtered CuKα radiation. The standard locked coupled scan settings were as follows:

Voltage = 40 kV.
Current = 40 mA.
Goniometer scan = 4°–70°2θ.
Step size = 0.0087°2θ.
Scan speed = 0.2 s/step.
Divergence slit = 0.3 mm.

Shipboard results yielded only qualitative results of the presence and relative abundances of the most common mineral components.

Diffractograms of bulk samples were evaluated with the aid of the EVA software package, which allowed for mineral identification and basic peak characterization (e.g., baseline removal and maximum peak intensity). Files were created that contained d-spacing values, diffraction angles, and peak intensities with background removed. These files were scanned by

the EVA software to find d-spacing values characteristic of a limited range of minerals, occasionally using aluminum oxide as an external standard to monitor data quality. Peak intensities were reported for each mineral identified to provide a semiquantitative measure of how each mineral identified varied downhole and among sites. Opal-A peak height was determined by the height of its peak at 22°2θ relative to the background level (Tada and Iijima, 1992), which is defined as the average of the intensities at 19° and 29°2θ. The abundance of opal-CT was measured by the height of the peak at 22°2θ when only typical opal-CT peaks occurred. Muscovite/illite and kaolinite/chlorite have similar diffraction patterns and were usually not distinguished shipboard. Digital files with the diffraction patterns are available from the LIMS database (**iodp.tamu.edu/tasapps/**).

Biostratigraphy

Preliminary age assignments for Expedition 346 were based on biostratigraphic analyses of calcareous nannofossils, planktonic foraminifers, radiolarians, and diatoms. Benthic foraminifers and ostracods were used primarily for paleoenvironmental interpretation. The biostratigraphy is tied to the geomagnetic polarity timescale (GPTS) (GTS2012) of Gradstein et al. (2012). Calcareous nannofossils, planktonic and benthic foraminifers, radiolarians, diatoms, and ostracods were examined in core catcher samples, and, where appropriate, additional samples were taken to refine biostratigraphic assignments. The preservation, abundance, and zonal assignment for selected samples and for each microfossil group were entered via DESCLogik into the LIMS database.

Calcareous nannofossils

Calcareous nannofossil zonal scheme and taxonomy

Nannofossil taxonomy follows Bown (1998) and Perch-Nielsen (1985). Bioevent ages were assigned based on the occurrence of calcareous nannofossils (dominant, present, or absent) in core catcher samples and in additional split-core sections, when necessary. Calibration of the identified events is derived mainly from Gradstein et al. (2012). The standard zonal schemes of Martini (1971) and Okada and Bukry (1980) are adopted (Fig. **F8;** Table **T1**). The first occurrences (FOs) of *Gephyrocapsa oceanica* and *Gephyrocapsa caribbeanica* denote the bases of Zones CN14a and CN13b, respectively. Ages and calibration sources for calcareous nannofossil datums are presented in Table **T1.**

Methods of study for calcareous nannofossils

Samples were prepared following the smear slide technique of Watkins and Bergen (2003) with Norland Optical mounting medium. Calcareous nannofossils were examined with a Zeiss polarized microscope at 1000× magnification. In addition, mudline samples were analyzed for calcareous nannofossils. Mudline samples were collected by emptying the sediment/water material from the top core liner into a bucket from which samples were pipetted for preparation of smear slides and scanning electron microscope (SEM) stubs.

Total calcareous nannofossil abundance within the sediment was recorded as

D = dominant (>90% of sediment particles).
A = abundant (50%–90% of sediment particles).
C = common (10%–50% of sediment particles).
F = few (1%–10% of sediment particles).
R = rare (<1% of sediment particles).
B = barren (none present).

Abundance of individual calcareous nannofossil taxa was recorded as

D = dominant (>100 specimens per FOV).
A = abundant (10–100 specimens per FOV).
C = common (1–10 specimens per FOV).
F = few (1 specimen per 1–10 FOVs).
R = rare (≤1 specimen per 10 FOVs).

Preservation of calcareous nannofossils was recorded as

G = good preservation (little or no evidence of dissolution and/or recrystallization; primary morphological characteristics unaltered or only slightly altered; specimens were identifiable to the species level).
M = moderate preservation (specimens exhibit some etching and/or recrystallization; primary morphological characteristics somewhat altered; however, most specimens were identifiable to the species level).
P = poor preservation (specimens were severely etched or overgrown; primary morphological characteristics largely destroyed; fragmentation has occurred; specimens often could not be identified at the species and/or generic level).

Radiolarians

Radiolarian zonal scheme and taxonomy

The radiolarian zonal scheme used during Expedition 346 is described in Morley and Nigrini (1995), Kamikuri et al. (2004, 2007), and Motoyama (1996, 2014) and was established for the Pacific mid to high

latitudes including the region's marginal seas. Some radiolarian datums established in the North Pacific (e.g., the rapid increase and rapid decrease of *Siphocampe arachnea* [Kamikuri et al., 2007]) are poorly constrained chronostratigraphically in the marginal seas' sediments. The last occurrence (LO) of *Axoprunum acquilonium* is reported at 0.33 Ma in the North Pacific (Kamikuri et al., 2007; Matul et al., 2002), although this datum may be older in the marginal sea according to results from DSDP Leg 31 and ODP Leg 127 (Alexandrovich, 1992; Ling, 1992; Motoyama, 1996). At ODP Sites 794, 795, and 797, the age of this datum may be 1.2–1.7 Ma (Alexandrovich, 1992).

For the East China Sea, the tropical Pacific radiolarian zones were used (Sanfilippo and Nigrini, 1998; Nigrini and Sanfilippo, 2001; Kamikuri et al., 2009).

Expedition 342 Scientists (2012) assigned GTS2012 ages to the tropical radiolarian datums (Table **T2**). All other datums were converted to GTS2012 from previous geologic timescales (Table **T3;** Fig. **F9**).

Methods of study for radiolarians

Sample preparation for light microscopy observation was conducted as follows:

1. Approximately 5 cm^3 of wet (core catcher) sediment was sieved and rinsed using a 45 µm mesh sieve.
2. When needed, samples were processed with 10% H_2O_2 and 15% hydrochloric acid (HCl) to remove calcium carbonate and clay infillings and resieved on a 45 µm mesh sieve.
3. Residues were dried on a slide, mounted with Norland optical adhesive, and covered with a 22 mm × 40 mm cover glass.
4. The adhesive was solidified by placing the slide under UV light for ~15 min.
5. Slides were partially examined at 50× to 400× for stratigraphic markers and other common taxa using a Zeiss Axioskop microscope.

Abundance estimates of the radiolarian assemblage are qualitative estimates of the concentration of radiolarians in individual sediment samples, using the following categories:

A = abundant (>10,000 specimens in a sample).
C = common (2,000–10,000 specimens in a sample).
F = few (500–2000 specimens in a sample).
R = rare (50–500 specimens in a sample).
VR = very rare (<50 specimens in a sample).
B = barren (0 specimens in a sample).

Abundance of individual radiolarian species was recorded as

A = abundant (>16% of the radiolarian assemblage).
C = common (4%–16% of the radiolarian assemblage).
F = few (1%–4% of the radiolarian assemblage).
R = rare (0.2%–1% of the radiolarian assemblage).
P = present (<0.2%).

Preservation of the radiolarian assemblage was recorded as

G = good (majority of specimens complete, with no or minor dissolution, recrystallization, and/or breakage).
M = moderate (minor but common dissolution, with a small amount of breakage of specimens).
P = poor (strong dissolution, recrystallization, or breakage; many specimens unidentifiable).

Diatoms

Diatom zonal scheme and taxonomy

Diatom biostratigraphy for Expedition 346 (Fig. **F10**) follows the work of Koizumi (1992) (ODP Leg 127/128), Barron and Gladenkov (1995) (ODP Leg 145), Yanagisawa and Akiba (1998), and Watanabe and Yanagisawa (2005). Although the majority of the biostratigraphy follows the work of Koizumi (1992), the zonal schemes are refined as needed.

Diatom ages for zones and datum events are calibrated to the GTS2012 timescale if there are changes from ATNTS2004 (Lourens et al., 2004) and also to be comparable with other microfossil datums (Fig. **F10;** Table **T4**). The LOs and FOs as defined by Yanagisawa and Akiba (1998) with modifications by Gladenkov (2003) are applied.

Diatoms are identified to the species level when possible. Key stratigraphic species were identified based on previous work of Koizumi (1992), Barron and Gladenkov (1995), and Yanagisawa and Akiba (1998).

Methods of study for diatoms

Diatom observations are based on smear slides from core catcher samples. If needed, additional smear slides are made from split-core sections in order to refine particular zone assignations or for age improvement. Smear slides are made by picking a small amount of unprocessed sediment with a disposable wood toothpick, spreading it on a slide, and diluting it with one or two drops of distilled water. The slide is then placed on a hot plate (30°–35°C) until the liquid on the slide evaporates. Norland optical adhesive is placed on the coverslip, and this coverslip is then glued to the slide. The adhesive was solidified by placing it under an UV lamp for 10–15 min.

Diatom total qualitative abundance is determined at 1000× magnification using phase contrast light. Observations are made on the two slide transects located at the center of the slide. This slide area is where the sediment is placed before spreading; thus, it is the area with the most consistent amount of sediment between all slides. The number of transects increases if any doubt in the species or their abundance occurs.

Diatom preservation was assessed by applying the following criteria:

G = good (valves are intact, including the most fragile species; some breaking occurs).
M = moderate (valves and most broken material show areolae and/or outside dissolution).
P = poor (extreme dissolution and/or fragmentation prevents species identification).

A question mark (?) regarding preservation is used when the sample does not allow an assessment of this property.

Diatom total abundance, a qualitative measure, is based on the amount of valves found in two slide transects:

D = dominant (>60% diatoms).
A = abundant (20%–60% diatoms).
C = common (5%–20% diatoms).
F = few (2%–5% diatoms).
R = rare (<2% diatoms).
B = barren (none present).

Diatom relative abundance is based on the assemblages found in two slide transects:

Ma = massive (>10 valves in two slide transects).
A = abundant (>5 valves in two slide transects).
C = common (3–5 valves in two slide transects).
F = few (2 valves in two slide transects).
R = rare (<2 valves in two slide transects).

For biostratigraphy purposes and in order to minimize biases because of the amount of sediment that is placed on the smear slides, the datums are defined by the presence of at least two specimens in two slide transects. This cutoff is chosen having taken into consideration the identification uncertainties and confidence levels discussed in Fatela and Taborda (2002) and the existence of laboratory cross contamination because of the presence of previous samples' sediment. Therefore, only relative diatom abundances defined as common or higher are considered for dating purposes. The number of transects is increased if any doubt arises regarding species identification or if only fragments of a particular species are present. The counting procedure and definition of counting units (diatom valves) follows Schrader and Gersonde (1978).

Foraminifers

Planktonic foraminiferal zonal scheme and taxonomy

The (sub)tropical planktonic foraminiferal zonal scheme for the Neogene (M, PL, and PT zones) follows Berggren et al. (1995a, 1995b) with modifications by Wade et al. (2011). For this expedition, the zonal scheme of Maiya (1978) was used, which is based on assemblage changes in the North Pacific Ocean and Japanese onshore sections as summarized in Miwa (2014). Additionally, datums from Lagoe and Thompson (1988) were used, which were recalibrated to the timescale of Cande and Kent (1992) by Lyle, Koizumi, Richter, et al. (1997). In order to maintain consistency, the ages of datums in Lagoe and Thompson (1988), Motoyama et al. (2004), and Miwa (2014) were converted to GTS2012 for Expedition 346.

The planktonic foraminiferal zonal scheme used is illustrated in Figure **F11.** Ages and calibration sources of planktonic foraminifer datums are presented in Tables **T5** and **T6.** Planktonic foraminiferal taxonomic concepts selectively follow those of Maiya et al. (1976), Takayanagi et al. (1976), Kennett and Srinivasan (1983), Bolli and Saunders (1985), Toumarkine and Luterbacher (1985), Loeblich and Tappan (1988), Spezzaferri and Premoli Silva (1991), Chaisson and Leckie (1993), Leckie et al. (1993), Spezzaferri (1994), Pearson (1995), Chaisson and Pearson (1997), Pearson and Chaisson (1997), and Pearson et al. (2006). A taxonomic list of planktonic foraminifer species from Tables **T5** and **T6** is given in Table **T7.**

Benthic foraminiferal taxonomy and paleodepth determination

Taxonomic assignments follow Tjalsma and Lohmann (1983), van Morkhoven et al. (1986), Miller and Katz (1987), Thomas (1990), Van Marle (1991), Katz and Miller (1991), Kato (1992), Jones (1994), Nomura (1995), Hanagata (2003), Hanagata and Hiramatsu (2005), Kaminski and Gradstein (2005), and Holbourn et al. (2013). The generic classification of Loeblich and Tappan (1988) was used and updated in some instances, in particular for uniserial taxa (Hayward, 2002). A taxonomic list of benthic foraminifers recorded during Expedition 346 is given in Table **T8.**

Paleodepth estimates were based on van Morkhoven et al. (1986) using the following categories:

Neritic = <200 m.
Bathyal = 200–2000 m.
Abyssal = >2000 m.

Methods of study for foraminifers

From each core catcher, 20–30 cm^3 of sediment was washed with tap water over a 63 µm wire mesh sieve. Indurated samples were soaked in a 3% hydrogen peroxide (H_2O_2) solution (with a small amount of Borax added) prior to washing. In addition, mudline samples from each hole were analyzed for planktonic and benthic foraminifers. Mudline samples were collected by emptying the sediment/water material from the top core liner of each hole into a bucket and then washed with tap water over a 63 µm wire mesh sieve. Tests using rose bengal were performed to confirm the presence of living ostracods and benthic foraminifers in the mudline sample. All samples were then dried in the sieves in a low-temperature oven at ~50°C and subsequently examined under a binocular light microscope. To avoid contamination of foraminifers between samples, the sieve was thoroughly cleaned, placed into a sonicator for at least 15 min, and then carefully checked. Species identifications for planktonic and benthic foraminifers were generally made on the >150 µm size fractions. The 63–150 µm size fraction was scanned for distinctive taxa. For Expedition 346, planktonic foraminiferal species distribution and range charts are presented in each site chapter. Benthic foraminiferal assemblage composition and paleodepth estimates were based on counts of ~100 specimens from the >150 µm size fractions, where possible. Relative percentages of benthic to planktonic tests were determined by counting specimens in four adjacent quadrants in three different locations on the picking tray.

Total abundance of foraminifers within the sediment was recorded as

A = abundant (>70% of sediment particles).
C = common (30%–70% of sediment particles).
R = rare (<30% of sediment particles).

The following abundance categories were estimated from visual examination of the dried sample for planktonic and benthic foraminifers:

D = dominant (>30% of foraminiferal assemblage).
A = abundant (10%–30% of foraminiferal assemblage).
F = few (5% to <10% of foraminiferal assemblage).
R = rare (1% to <5% of foraminiferal assemblage).
B = barren.

The preservation status of planktonic and benthic foraminifers was estimated as

VG = very good (no evidence of overgrowth, dissolution, or abrasion).
G = good (little evidence of overgrowth, dissolution, or abrasion).
M = moderate (calcite overgrowth, dissolution, or abrasion were common but minor).
P = poor (substantial overgrowth, dissolution, or fragmentation).

In addition, ostracods, pteropods, fish teeth, sponge spicules, and other bioclasts were examined in the >150 µm size fractions of the core catcher samples used for foraminifer analysis.

Abundance of pteropods, fish teeth, sponge spicules, and other bioclasts was noted as

C = common (>5 specimens per sample).
R = rare (1–5 specimens per sample).
B = barren.

Abundance of ostracods was noted as

A = abundant (>30 specimens per sample).
C = common (10–30 specimens per sample).
R = rare (<10 specimens per sample).
B = barren.

The preservation status of ostracods was estimated as

VG = very good (valves translucent; no evidence of overgrowth, dissolution, or abrasion).
G = good (valves semitranslucent; little evidence of overgrowth, dissolution, or abrasion).
M = moderate (calcite overgrowth, dissolution, or abrasion were common but minor).
P = poor (substantial overgrowth, dissolution, or fragmentation of the valves).

Geochemistry

The shipboard geochemistry program for Expedition 346 emerged with five concepts in mind. First, the primary objectives of the cruise revolve around paleoceanography, particularly the construction of detailed sedimentary records (see **"Introduction, background, and objectives"** and **"Stratigraphic correlation and sedimentation rates"**). As such, the probability of obtaining a continuous sedimentary splice at each drill site, without missing intervals, was maximized as possible.

Second, previous drilling in this region during Legs 127/128 (Tamaki, Pisciotto, Allan, et al., 1990; Ingle, Suyehiro, von Breymann, et al., 1990) demonstrated that sedimentary sequences throughout the region contain abundant authigenic minerals. This includes carbonates and silicates, which stem in part from dissolution of microfossils (Matsumoto, 1992; Nobes et al., 1992), as well as sulfides, which can react with oxygen during transport and storage. Sufficiently resolved interstitial water profiles are desirable to un-

derstand the location of authigenic mineral formation because mineral diagenesis impacts the sedimentary record and paleoceanographic objectives.

Third, melting of continental ice sheets decreased global ocean water salinity significantly over the last 20,000 years. For bottom water at a given location, the salinity decrease can be quantified by modeling interstitial water chloride or $\delta^{18}O$ profiles (e.g., McDuff, 1985; Schrag et al., 1996; Adkins et al., 2002). The magnitude of salinity change appears to have differed from one deepwater location to another, presumably because of variations in oceanography. Interstitial water profiles amenable for such work have not yet been generated in the northwest Pacific marginal seas.

Fourth, previous work, both on piston cores and on sediment recovered from drilling during Legs 127/128, has emphasized that deep-sea sediment across the Marginal sea spans a particularly wide range of chemical environments derived from microbially mediated organic carbon degradation (Masuzawa and Kitano, 1983; Murray et al., 1992). For example, some locations (Site 794) have a relatively modest maximum alkalinity (<12 mM) and little to no gas in interstitial water at depth; other locations (ODP Site 798) have very high alkalinity (>75 mM) and abundant methane within 100 m of the seafloor (Tamaki, Pisciotto, Allan, et al., 1990; Ingle, Suyehiro, von Breymann, et al., 1990). It is increasingly important to document and understand the deep biosphere across a broad range of sites, given overarching IODP goals.

Fifth, sampling with Rhizons (see **"Rhizons"**) is evolving to become a complementary approach for collecting interstitial water during drilling expeditions, especially from horizons within the upper 100 m of the sediment column. Such sampling seems especially useful during paleoceanography expeditions, where core flow can be fast and sediment preservation is at a premium. However, Rhizons have been used mostly without basic tests and without clear protocol.

To summarize, the Geochemistry group desired to generate high-quality data sets on a paleoceanography cruise that could enhance rather than hinder primary objectives.

Sample collection

General plan

In line with the paleoceanographic objectives of the expedition and general goals of IODP, we constructed a geochemistry sample plan before drilling began. The strategy accounts for three geochemists on each 12 h shift and a nominal water target of 30–40 mL for squeezed samples. The water budget reflects the desired quantity for a range of analyses, including routine shipboard measurements, several shore-based requests, and extra archive water for potential future work (Table **T9**). We document the original plan below, which includes our "predrilling" rationale, and discuss modifications and impacts of this plan in various site chapters.

Sampling plan for routine sampling over the upper sedimentary sequence (usually equivalent to APC recovery)

- Gather a water sample from within the core liner above the uppermost sediment recovered (typically Core 1H in Hole A). This "mudline" sample can be used for comparison with bottom water and interstitial water (Gieskes, 1975).
- Collect two whole-round samples per APC core in Hole A for interstitial water squeezing (IW-Sq). These IW-Sq samples would be collected at the base of Sections 1 and 4, such that they are evenly spaced down Hole A, and one whole-round sample (Section 1) would likely occur "off-splice." Whole-round samples from APC cores would begin at a 5 cm length and increase to a maximum of 10 cm downhole because porosity and water content would generally decrease with depth below the seafloor.
- Obtain two headspace (HS) gas samples per APC core in Hole A. These would be collected at the top of Sections 2 and 5, so as to pair with IW-Sq samples.
- Collect two sediment samples per APC core in Hole A to be analyzed for carbonate and organic carbon contents. These would be splits of interstitial water squeeze cakes, so as to minimize discrete sampling of sediment core.
- Obtain one whole-round interval, nominally one per core for the uppermost four cores and every alternate APC core in Hole A after that, for shore-based microbiology research. These would be 5 cm in length and, where appropriate, adjacent to whole-round IW-Sq samples.
- Obtain two syringe samples (~2.5 cm^3) on selected APC cores in Hole A for microbiological cell counts. These samples would be associated with the microbiology whole rounds or IW-Sq samples.

No routine geochemistry sampling was planned for Holes B or C.

Sampling plan for routine sampling over the lower sedimentary sequence (usually equivalent to XCB recovery)

- During XCB coring, the sediment often becomes "biscuited," and upward of half the material over a given depth interval is not appropriate for water sampling. To maintain a minimum pore water budget (Table T9), whole-round samples from XCB cores typically need to be thicker. On the other hand, at deep sediment depths, concentration changes in dissolved constituents often occur over longer depth intervals. This means that, for many purposes, interstitial water samples can be spaced farther apart. Thus, for XCB operations, we aimed to collect one 10 cm long whole-round sample per core for interstitial water squeezing in Hole A and over extended depths in Holes B or C should they surpass the total depth of Hole A. The samples would be taken consistently at the base of Section 1 such that, over depths spanned by more than one hole, the probability of collecting the sample off-splice was maximized.
- Obtain one HS gas sample per core at the top of Section 2, so as to pair with interstitial water samples taken for squeezing. This HS sample would be taken with a cork borer or from chips.
- Collect one sediment sample per core, a split of the squeeze cake, to analyze for carbonate and organic carbon contents.

The combined routine sampling plans would provide reasonably detailed interstitial water and gas profiles down the cored sedimentary section at all sites, as well as sufficient samples for requested shore-based microbiology work. It should also allow maximum stratigraphic correlation between three holes because no whole-round samples would be taken from Hole B or Hole C, except from XCB cores at deep depths, where decimeter-scale stratigraphic correlation between holes using various techniques (e.g., GRA, magnetic susceptibility, and NGR) often becomes very difficult (e.g., Wilkens et al., 2013).

This sampling strategy, however, will not generate tight depth constraints on chemical reaction horizons, such as the sulfate–methane transition (SMT). The plan also precludes shipboard investigations of probable interest; for example, variability in sediment chemistry over short depth increments (e.g., dark and light intervals) and the composition of unusual sedimentary features (e.g., nodules). Without additional "nonroutine" sampling, several basic studies would have to await initiation of shore-based investigations.

Sampling plan for nonroutine sampling

1. Collect one Rhizon water sample per section from the upper 50 m of one hole at selected sites to enable construction of $\delta^{18}O$ and Cl^- profiles that relate to changes in bottom water salinity since the Last Glacial Maximum.
2. Gather Rhizon water samples from several probable off-splice intervals of Hole A at several sites (e.g., upper 70 cm of Section 1 and all of Section 7). The purpose of this sampling would be to conduct tests of Rhizon sampling and to aid stratigraphic correlation through comparison of interstitial water chemistry profiles between Holes A and C.
3. Obtain higher resolution Rhizon water samples from depth intervals of Hole C where interstitial water analyses of Hole A show major changes in chemical gradients. This would allow definition of precise depths of certain microbial reaction zones. As part of this strategy, it is important to process the samples from Hole A as fast as possible, so as to guide the placement of the high-resolution Rhizon suite of samples.
4. Collect multiple squeeze and Rhizon samples across numerous intervals in holes specifically dedicated for geochemistry.

In all cases above, Rhizon sampling would commence after core sections pass through the STMSL and during the time (nominally 3–4 h) when cores equilibrate for NGR logging (see **"Stratigraphic correlation and sedimentation rates"**).

Rhizon sampling occurred in the Downhole Logging Laboratory located immediately adjacent to the lore loggers, thus minimizing impact on core flow. Basic physical properties logs (specifically GRA and magnetic susceptibility) would thus be obtained before Rhizon sampling, in the case that water removal over short distances (several centimeters) might impact overall stratigraphic correlation. Overall, core flow was not negatively impacted by the Rhizon sampling.

The following amendments allow for construction of detailed geochemical profiles across reaction zones but with a very low probability of preventing a continuous sedimentary splice. The amendments also provide a means to generate basic knowledge regarding sediment chemistry on ship before most sediment sampling and analysis occurs on shore.

- Collect Vacutainer (VAC) samples of selected gas voids at sites and across depth intervals where they occur.

- Collect supplementary sediment samples from the working half of Hole A, assuming sufficient time for sediment processing and analyses exists. These would be analyzed for carbonate and organic carbon contents. Generally, these would be splits of samples taken for physical property measurements (see **"Physical properties"**) or discrete samples of interesting sedimentary horizons (e.g., dark and light layers; Tada et al., 1992).
- Collect selected sediment samples from the working half of Hole A for examination by SEM. For example, SEM analyses of sulfide phases on the ship and later on shore may provide insight into the effects of sulfide oxidation upon surrounding sediment over time.

Gas hydrate recovery was a possibility at several drill sites, given that it was recovered at ODP Site 796 (Shipboard Scientific Party, 1990), in drill sites of the Ulleung Basin (e.g., Kim et al., 2013), and in piston cores along the western slope of Japan (e.g., Snyder et al., 2007). Along with the above plan, we submitted details on how these ephemeral solids would be handled. However, specimens of gas hydrate were not recovered during Expedition 346.

As can be seen by progressing through the "Geochemistry" sections in each site chapter, the sampling plans outlined above were modified extensively for several reasons. For example, the ability to generate a composite sediment record in almost "real time" with two holes (see **"Stratigraphic correlation and sedimentation rates"**) meant that a Hole C was not needed at most sites. The quick realization that Rhizons gave excellent interstitial water samples also opened exciting avenues for research.

Gas sampling

Volatile hydrocarbons and other gases in sediment were collected by two techniques: HS and VAC. Most gas samples were collected by the HS procedure, as required by IODP safety protocols, even though measured values are not easily interpreted at high gas concentrations (Paull et al., 2000).

For the HS procedure, 3–5 cm^3 of sediment was collected from the top of core sections on the catwalk using a graduated syringe or cork borer. Samples were extruded into a 21.5 cm^3 glass serum vial containing 5 mL of saturated NaCl solution. The vial was then sealed with a septum and metal crimp cap and lightly swirled. Measuring sediment volume and placing into a saturated NaCl solution remain nonroutine during IODP expeditions but allow for systematic semiquantification of interstitial gas volume at low gas concentrations (D'Hondt, Jørgensen, Miller, et al., 2003). Vials were then heated at 70°C for 30 min. After heating, a 5 cm^3 volume of gas from the headspace in the vial was sampled with a glass syringe for analysis by gas chromatography.

At sites with high gas concentrations at in situ pressure, gas voids develop during core recovery because of supersaturation at atmospheric pressure. Some of these voids were sampled using the Vacutainer approach (even though traditional vacuum containers were not used). A device with a heavy-duty needle and valve was pushed through the core liner. A closed syringe was attached and then filled with gas through the valve. A 5 cm^3 volume of the gas sample was directly analyzed by gas chromatography.

Interstitial water sampling

Interstitial water was extracted from sediment cores by two different techniques: squeezing of whole-round intervals and removal using Rhizon samplers. The first technique has been used routinely during scientific ocean drilling expeditions for nearly four decades (Manheim and Sayles, 1974; Sayles and Manheim, 1975; Gieskes, 1975), and resultant waters are commonly referred to as interstitial water samples. The second technique was first used for scientific drilling during IODP Expedition 302 in 2004 (Dickens et al., 2007) and has steadily become more common (e.g., Expedition 320/321 Scientists, 2010b; Schrum et al., 2012). Each technique appears to have advantages and disadvantages, but a series of unanswered questions surrounds the use of Rhizons. For these reasons, we have distinguished interstitial water samples as coming through a squeezer (IW-Sq) or a Rhizon (IW-Rh) and have dedicated part of our geochemistry program to tests involving Rhizon sampling. All whole-round and Rhizon samples were taken at room temperature (and pressure), although we are aware of potential temperature effects on interstitial water chemistry (Sayles and Manheim, 1975; Gieskes, 1975).

Whole rounds

Whole-round samples for squeezing (IW-Sq) were taken on the catwalk after a core was cut into 1.5 m (nominal) sections. The samples were taken to the Geochemistry Laboratory, where they were pushed out of the liner onto a tray, trimmed to remove potential contaminating sediment and water, and placed into a Manheim Ti squeezer (modified from Manheim and Sayles, 1974). When there was a backlog, such as occurs when several whole rounds are taken over a short duration, some whole rounds were stored in a refrigerator. For all squeezed samples, times from collection through squeezing did not exceed more than 2 h.

During extraction of interstitial water, gauge pressures as high as 24,000 lb force were applied to squeezers using a Carver laboratory hydraulic press. Emerging interstitial water passed through a prewashed (18.2 MΩ water) Whatman Number 1 filter fitted above a titanium screen within the squeezer and a 0.45 µm polysulfone disposable filter (Whatman Puradisc PES) outside the squeezer before entering a precleaned (10% HCl) 60 mL syringe. For the last three IODP drilling sites (U1428, U1429, and U1430), we also placed a 0.20 µm polysulfone disposable filter (Whatman Puradisc PES) between the 0.45 µm filter and the syringe in an effort to remove very small particles.

After squeezing, the compressed cylinder of sediment (squeeze cake) was removed and the squeezing apparatus was cleaned. Portions of the squeeze cake were used for shipboard sediment analyses (below), whereas the rest (>75%) was saved for future shore-based examination. Cleaning the squeezers involved initial scrubbing with water, thorough rinsing with 18.2 MΩ water, and air-drying of all components (including using compressed air) and oven-drying of the screens.

Rhizons

Rhizons are thin tubes of hydrophylic porous polymer. When inserted into a sediment core through a hole in the liner and attached to a collection tube and an evacuated syringe, they permit collection of small volumes (typically <12 mL) of interstitial water through suction filtering. Such interstitial water samples are collected without removal of whole rounds, thus preserving the sedimentary record. They also enable water sampling at very high depth resolution (<5 cm). For Expedition 346, the chosen samplers were Rhizon CCS 5 cm female Luers (flat tip and 2.5 mm outer diameter) from Rhizosphere Research Products (Netherlands).

A basic procedure for collecting Rhizon samples on drilled cores has been developed over the last few years. After a core section is cut on the catwalk and brought to the Core Laboratory, it is placed on the STMSL, which quickly generates a record of GRA and magnetic susceptibility along the section. This step is important because GRA and magnetic susceptibility records often form the backbone for stratigraphic correlation between holes, because GRA measurements closely correspond to wet bulk density, and because Rhizon sampling could potentially decrease wet bulk density over several centimeters. The latter effect occurs because water removal introduces air along the inside of the core liner (Dickens et al., 2007). The core is then turned so the plane separating the archive and working halves of the core is vertical. Small holes (~3 mm diameter) are drilled through the core liner along this vertical plane, and Rhizon samplers with accompanying tubes, valves, and 10 mL syringes are inserted. The time required to extract 10 mL of interstitial water is dependent on the porosity and permeability of the sediment as well as the strength of suction generated by the syringe. New syringes extracted interstitial water much more quickly than syringes that had been used and acid-washed. Interstitial water is extracted over 0.1–3 h (unless modified for a specific reason) as a core section equilibrates for NGR logging. The water sample is then taken to the Geochemistry Laboratory for analyses.

Despite this general procedure, numerous issues concerning Rhizon sampling of drilled cores remain. Do Rhizons need pretreatment before insertion? How much do they impact sediment properties, such as wet bulk density and construction of spliced sediment records? Do they render significantly different chemistry than squeezed samples? We conducted a series of tests during Expedition 346 to evaluate some of these questions. Results are reported in the site chapters of this volume.

Solid-phase sampling

Small volumes of sediment were taken from squeeze cakes or the discrete intervals of interesting sedimentary horizons from the working halves of cores. These samples were freeze-dried and subsequently powdered by hand with an agate mortar and pestle for chemical analyses. The samples generally contain 1–5 wt% salt, which precipitated from pore space during the freeze-drying process.

Microbiology sampling

Syringes

A set of sterilized 2.5 cm^3 syringes with the tapered tips removed was provided to the Geochemistry Laboratory before departure. These syringes were used to collect samples for cell counting.

After a core was sectioned on the catwalk and a whole-round IW-Sq was sliced off with an ethanol-sterilized spatula, a syringe was plunged into the center of the exposed core to collect a cylinder of sediment. While holding the plunger, about 2.0 cm^3 of sediment was ejected from the syringe into a tube containing 10% filtered formalin solution. The tubes were labeled and stored in a refrigerator at 4°C within 20 min after arrival on the catwalk.

Whole rounds

There was interest in collecting sediment for shore-based microbiological DNA/RNA analyses. Soon after

selected cores arrived on the catwalk, a 5 cm long whole-round interval of sediment was cut from the core using an ethanol-sterilized spatula. Typically, such whole-rounds were located directly above an IW-Sq sample, which meant near the bottom of Section 1 and included the interval that was sampled for microbial cell counting (above). The whole round was capped on both ends, placed in an opaque gray Ziploc bag, flushed with nitrogen, and heat sealed. This bag was placed in a clear plastic bag and heat sealed again. Samples were processed and stored in a –80°C freezer within 15 min after arrival on the catwalk.

General commentary

Before examining our analytical methods and ultimately traveling along our geochemical odyssey (see the "Geochemistry" section in each site chapter), we thought it appropriate to insert an interlude briefly commenting on four topics.

First, volatile gas concentrations determined on HS samples are imperfect measurements. The gases evolve as they pass from the pore space of a sediment plug into a headspace within a closed container. At low gas concentrations, the volume of sediment and headspace within the vial are important, as is the solubility of gas, which depends on temperature and salinity. Of course, gas solubility is also important at high gas concentrations, but in this case, much of the gas can escape sediment before the HS sample is even collected (Paull et al., 2000). Volatile gases measured by the HS technique during most drilling expeditions are presented as parts per million by volume (ppmv), although millimolar is a far more useful unit. We have maintained the use of ppmv but have measured the volume of sediment such that shore-based work might convert to mM with physical property measurements.

Second, the chemistry of seawater, and by extension interstitial water in the marine environment, can be expressed using several different units (e.g., Millero et al., 2008). Within the laboratory on board the *JOIDES Resolution*, the customary unit for reporting concentrations of dissolved species is molarity (M), or mole per liter of solution (seawater) (Gieskes et al., 1991; Murray et al., 2000). This differs from the unit expressed in much of the literature, including classic papers on interstitial water chemistry (e.g., Sayles and Manheim, 1975), which is mole per kilogram of solution (seawater). However, such reporting of mole per liter is common practice and convention in the water column chemistry community. Conversion between the two units is straightforward (Table **T10**). The reason why this subject arose during Expedition 346 is that deep waters of the marginal sea are slightly but noticeably fresher than most of the ocean. Below ~300 m water depth, these waters are typically referred to as Japan Sea Proper Water and have a salinity of ~34.05 (Sudo, 1986). This becomes important to understanding the interstitial water chemistry.

Third, most dissolved constituents have more than one species of significance. For example, in seawater, B can occur as $B(OH)_4$ or $B(OH)_3$ (Millero et al., 2008). We have avoided assigning charge to many dissolved constituents throughout this volume, in part to emphasize that the measured value typically reflects the sum of multiple species.

Fourth, the depth of most samples needs consideration. This reflects the vicissitudes of drilling, including the presence of core gaps and overlaps and differential stretching of sediment. When comparing samples between holes at a given site, it is typically appropriate to convert reported depths beneath the seafloor to a composite depth scale (see **"Stratigraphic correlation and sedimentation rates"**). However, when using concentration gradients to estimate fluxes, a justified depth below seafloor is more correct.

Gas analyses

Two gas chromatographs were used for gas analyses. One was specially calibrated for determining methane concentrations, and the other was calibrated for determining higher hydrocarbon concentrations. Both gas chromatographs are Agilent 6890 models equipped with a 2.4 m × 3.2 mm stainless steel column packed with 80/100 mesh HayeSep R and a flame ionization detector. The instruments quickly measure concentrations of methane (C_1), ethane (C_2), ethene ($C_{2=}$), propane (C_3), and propene ($C_{3=}$).

The gas syringe was directly connected to the gas chromatograph through a 1 cm^3 sample loop, and 5.0 mL gas was injected. Helium was used as the carrier gas, and the gas chromatograph was programmed to start with an oven temperature of 80°C held for 8.25 min before ramping at 40°C/min to 150°C, with a final holding time of 5 min. Data were collected and evaluated with an Agilent Chemstation data-handling program. Chromatographic response was calibrated against known standards provided by Scott Specialty Gases.

Interstitial water analyses

IAPSO

The general standard used for interstitial water analyses was International Association for the Physical Sciences of the Oceans (IAPSO) standard seawater. This was Batch P154 obtained from OSIL Envi-

ronmental Instruments and Systems. However, IAPSO is not fully appropriate for certain interstitial water analyses (e.g., samples with very high concentrations of Ba or Fe).

Salinity

Salinity was analyzed with a Fisher Model S66366 portable salinity refractometer named Erik. A few drops of sample were applied to the daylight plate assembly with an eye dropper, and the measurement was read through the eye piece. Typical measurement precision is ±1‰, and blanks were analyzed routinely to check for contamination.

Alkalinity and pH

We began with the strict goal of pH and alkalinity being generally measured immediately after squeezing or Rhizon extraction. The pH was measured with a combination glass electrode (Brinkman pH electrode), and alkalinity was determined by Gran titration with an autotitrator (Metrohm 794 Titrino). Three milliliters of interstitial water was titrated with 0.1 M HCl at 25°C. The electrode was calibrated using a series of buffers with a pH of 4, 7, and 10. Standard ratios were calculated by running a series of standard solutions of different concentrations of Na_2CO_3 (5, 20, 40, 50, and 100 mM) and IAPSO seawater. The standard correction factor was specified before each analysis depending on the alkalinity.

IAPSO seawater was analyzed every ~12 h or after a period of nonuse to check accuracy. Concentrations were typically within 5% of the expected value for IAPSO (2.325 mM), and correction factors were adjusted if the measured value was outside of the accepted range (2.21–2.44 mM). Alkalinity is reported in millimolar units throughout this report, rather than milliequivalents per liter (meq/L), following previous discussion (Gieskes et al., 1991).

As will become obvious later in the site chapters of this volume, alkalinity was measured on some samples 24 h after collection. This is not ideal because alkalinity of interstitial water samples generally decreases over time (Gieskes, 1975). However, the change in alkalinity is not as great as perceived.

Chlorinity

Chloride concentrations were measured by titration with 0.1 M silver nitrate ($AgNO_3$) using a Metrohm 785 DMP Titrino autotitration system. Interstitial water aliquots of 0.5 mL were diluted with 30 mL of dilute nitric acid to keep precipitated flocculent well separated, which increased the probability of contact between Cl^- and Ag^+ during titration. IAPSO seawater standard was analyzed to check precision and accuracy (expected chlorinity = 559 mM). The instrument was recalibrated if it was not within 0.5% of the expected concentration (556.2–561.8 mM). A recalibration was not required during Expedition 346 because the standard checks always fell within range.

Ion chromatography

In June 2013, a new Metrohm 850 professional ion chromatograph with an 858 professional sample processor was added to the Geochemistry Laboratory. In principle, this instrument can measure concentrations of major anions (Cl^-, SO_4^{2-}, and Br^-) and major cations (Ca^{2+}, Na^+, Mg^{2+}, and K^+). Only anion measurements from ion chromatography are reported for Expedition 346 drilling sites because instrument problems precluded meaningful analyses of cation concentrations (although these were quantified using inductively coupled plasma–atomic emission spectroscopy [ICP-AES], see below).

Interstitial water was diluted 1:100 with 18.2 MΩ deionized water in preparation for ion chromatography analysis. The IAPSO seawater standard was diluted by various amounts (1:80 to 1:500) to create a six-point calibration curve. The r^2 for the calibration curve was always >0.99, and relative standard deviation varied from 0.8% to 3.4%.

Accuracy was checked by running 1:100 dilution of IAPSO standard seawater every ~10 samples, and a new calibration curve was run if measured concentrations deviated from the expected values (28.9 mM for SO_4^{2-} and 0.865 mM for Br^-). Precision was 3% for SO_4^{2-} and Br^-.

After instrument repairs during the expedition, SO_4^{2-} concentrations approached ~2 mM in samples deeper than the SMT boundary, whereas prior to the repairs they had approached zero. Procedural blanks were analyzed and repeatedly yielded zero SO_4^{2-}, indicating that there was no instrument contamination. The reason for the 2 mM results generated at depths where SO_4^{2-} should be completely absent is currently unknown.

Inductively coupled plasma–atomic emission spectroscopy

Suites of major (Ca, Mg, K, and Na) and minor (B, Ba, Fe, Li, Mn, Si, and Sr) elements were analyzed by ICP-AES with a Teledyne Prodigy high-dispersion ICP spectrometer.

The shipboard ICP-AES procedure is based on Murray et al. (2000) and the user manuals for new shipboard instrumentation with modifications as indicated. Samples and standards were diluted using 2% ultrapure HNO_3 spiked with 10 ppm Y with dilution

ratios of 1:200 for major element analyses (Na, K, Ca, and Mg) and 1:20 for trace element analyses (B, Mn, Fe, Sr, and Ba).

Samples were run in batches of typically 30–50 samples. With every batch run for minor elements (B, Ba, Fe, Li, Mn, Si, and Sr), an eight-point calibration curve was created using synthetic seawater spiked with minor elements to varying degrees and used to convert background-corrected intensities to concentrations. For major elements (Ca, Mg, K, and Na), a seven-point calibration curve was created using different dilution levels of IAPSO seawater. A drift solution was run every five samples. Blanks were run with every batch to check for contamination and allow for blank subtractions. The standard reference material, IAPSO seawater, was prepared three times using a separate pipette tip for each dilution, and all three were run as unknowns. The standard deviation of these triplicate analyses divided by the average value indicated the precision of each run. The IAPSO precision within a single run and between all runs was <2% of the measured value for Ca, K, Mg, Na, B, Li, and Sr. Concentrations of Ba, Fe, Mn, and Si in IAPSO commonly fell below detection limit and could not be used to quantify precision for these elements. The IAPSO values were compared to the known concentrations (for the conservative elements in IAPSO with known concentrations) to check that the results were accurate.

Each run used background-corrected intensities that were drift corrected, and a procedural blank was subtracted if there was significant drift (>5%). For some elements (e.g., Fe, Si, and B), the standards prepared with synthetic seawater showed a lower background level around the spectral peak than IAPSO standard seawater and pore water samples. The matrix difference is likely responsible, and in the future, spiking IAPSO with minor elements would aid in reducing this matrix affect. There was a spectral interference between Ba and Li when Ba concentrations were high. Samples with high Ba created a spectral peak that overlapped with the lower background point on the ICP-AES peak for Li. On sites with high Ba, Li was background corrected only using the right-hand background point (higher wavelength).

The Ba lines on the ICP were problematic at high concentrations because the instrument response was not linear at that range. Although the shape of the Ba profiles and relative intensities are likely accurate, Ba concentrations are too high and a correction is required using samples analyzed on shore after the expedition. In this report, unconstrained Ba concentrations are reported and the inaccuracies are noted in the specific site chapters when necessary.

Spectrophotometry

Dissolved ammonium (NH_4^+), phosphate (PO_4^{3-}), silica (H_4SiO_4), sulfide (HS^-), and "yellowness" were determined spectrophotometrically using an Agilent Cary 100 ultraviolet-visible (UV-VIS) light spectrophotometer. In general, interstitial water samples can have color either because of microbial reactions below the seafloor or because of addition of reagents in the laboratory. Colored samples were then "sipped" from a vial (~3 mL) into a cell and measured for absorbance at a specific wavelength. The size of the sample cell was 715 µL. Measurements of the first three species listed above are routine during scientific drilling expeditions (Gieskes et al., 1991), but a brief description of the methods is outlined below.

Ammonium concentrations were determined using the method of Solórzano (1969), which relies on the diazotization of phenol and the subsequent oxidation of the diazo compound by Chlorox to yield a blue color that is analyzed at 640 nm. With each run, standards were prepared to make a 13-point calibration curve covering the range of ammonium concentrations encountered in interstitial water samples. When concentrations exceeded the maximum calibration standard, which is common at sites with high levels of organic matter degradation, samples were diluted as necessary and corrected for the dilution after conversion to concentration. A standard was run independent of the calibration curve to check for accuracy, and sample replicates were run to check for precision. Precision was at 2% of the measured value, and results were accurate within precision.

Phosphate concentrations were determined using the method described by Strickland and Parsons (1968) as modified by Presley (1971). In this method, orthophosphate reacts with Mo(VI) and Sb(III) in an acidic solution to form an antimony-phosphomolybdate complex. Ascorbic acid reduces this complex, forming a blue color that is measured at 885 nm. Standards were prepared with each run to create a nine-point calibration curve to convert absorbance to concentration. Samples were diluted as necessary if concentrations exceeded the calibration range and were corrected after conversion to concentration. Precision and accuracy checks were quantified the same way as in the ammonium procedure. Precision was <0.5% of the measured value, and independent standard checks were accurate within precision.

Silica concentrations were determined by the molybdate method, where dissolved silica reacts with a molybdate reagent in an acid solution to form molybdosilicic acid. The complex then is reduced by

ascorbic acid to form molybdenum blue, which is measured at 812 nm. A 10-point calibration curve was analyzed with each run to convert absorbance to concentration. Precision, quantified similarly to ammonium and phosphate, was <0.5%, and independent standards were accurate within precision.

Total dissolved sulfide ($\Sigma H_2S = H_2S + HS^-$) was determined by the methylene blue method (Cline, 1969). As soon as the interstitial water was extracted by squeezing or Rhizons, 0.6 mL of 5 wt% zinc acetate was added to 3 mL of sample in a glass vial to fix the sulfide in solution. A mixed diamine reagent was added to the vial and reacted with the fixed sulfide to form methylene blue. The absorption of the blue color is measured at a wavelength of 670 nm. Concentrations were diluted as necessary for absorbance to fall within the calibration range and corrected after conversion to concentrations. A seven-point calibration curve was created from standards that were analyzed with each run. During every run for all analyses, samples and standards were analyzed in random order to ensure that downcore trends are not an artifact of varying instrument response.

Interstitial water can become visibly yellow at sites with high amounts of organic carbon degradation because certain dissolved organic compounds impart color (You et al., 1993; D'Hondt, Jørgensen, Miller, et al., 2003). At the beginning of Expedition 346, we decided to systematically quantify this yellowness by measuring the absorbance of samples at 325 nm. This wavelength was chosen because it had been used to examine the color of interstitial water at several previously drilled sites (You et al., 1993; D'Hondt, Jørgensen, Miller, et al., 2003). However, examination of absorbance at multiple wavelengths across a suite of samples showed that the color spectrum is complex, as known from studies of seawater color (Briucaud et al., 1981). Thus, analyses evolved as the expedition progressed so that samples were eventually measured for absorbance at 227, 325, and 375 nm. Initially, 1.0 mL aliquots of interstitial water were placed into vials with 2.0 mL of deionized water. These were measured for absorbance along with a standard in every batch, so the measurement could be compared with those determined elsewhere independent of instrument parameters, especially including the path length of light. However, at sites with interstitial water having low absorbance, samples were eventually analyzed without dilution, as this improves analytical precision. In all cases, the standard used for comparison was the internationally recognized JWBL standard, procured from Kilmarnock, Scotland. Postcruise data processing will use the standard to quantify the magnitude of yellowness in JWBL units for intersite, interlaboratory comparisons, but in this report, yellowness is reported in units of absorbances.

Solid-phase analyses

Sedimentary inorganic and organic carbon

Inorganic carbon (IC) contents were determined using a Coulometrics 5011 carbon dioxide coulometer. Samples of ~10 mg of freeze-dried, ground sediment were reacted with 2 M HCl. The evolved CO_2 was back-titrated to a colorimetric end-point. Carbonate content, reported as weight percent, was calculated from the IC content based on the assumption that all inorganic carbon exists as $CaCO_3$:

$$\text{wt\% } CaCO_3 = \text{wt\% IC} \times 8.33.$$

Analytical reproducibility was determined by replicate measurements of selected samples and internal standards. Expected errors (1σ), based on previous expeditions, range from 0.3 to 0.4 wt%.

Total carbon (TC) content was determined using a Thermo Electron Flash EA 1112 elemental analyzer equipped with a Thermo Electron packed GC column CHNS/NCS (polytetrafluoroethylene; length = 2 m; diameter = 6 mm × 5 mm) and thermal conductivity detector (TCD). Aliquots of 10 mg of freeze-dried, ground sediment in tin cups were combusted in the reactor oven of the instrument with a pulse of O_2. In cases of high carbonate, the sample amount was cut in half. Nitrogen oxides were reduced to N_2, and the mixture of gases produced (N_2, CO_2, H_2O, and SO_2) was separated by gas chromatography and measured by the TCD. The gas chromatograph oven temperature was held at 65°C. All EA measurements were calibrated by comparison to a pure sulfanilamide standard. Total organic carbon (TOC) was determined as the difference between TC and IC:

$$\text{wt\% TOC} = \text{wt\% TC} - \text{wt\% IC}.$$

The C/N ratio was determined and reported as an atomic percent (at%).

Paleomagnetism

Paleomagnetic samples and measurements

Paleomagnetic studies during Expedition 346 focused on measuring the natural remanent magnetization (NRM) of archive-half sections. NRM of archive-half sections of the first or the longest hole at each site were measured before and after alternating field (AF) demagnetization with a 20 mT peak field at every 5 cm interval resolution. Because of increased core flow and limited measurement time at the

paleomagnetism station, NRM of archive-half sections of the other holes at each site were usually measured only after 20 mT AF demagnetization at every 5 cm interval resolution.

We typically collected one oriented discrete sample per core from working-half sections for measuring NRM after complete stepwise AF demagnetization, bulk magnetic susceptibility, and anisotropy of magnetic susceptibility (as time permitted). Discrete samples were usually taken from Hole A at each site and from the lower part of the stratigraphic section of the deepest hole if the deepest hole is different from Hole A. Discrete samples were extracted by pushing plastic Natsuhara-Giken cubes (with 2 cm external edge length and an internal volume of ~7 cm^3) into working-half sections with the arrow marker on the cube pointing to the upward direction of the core (Fig. **F12A**). The sample *x*-axis is toward the double lines on the working-half sections and the up arrow marks the negative *z*-axis (Fig. **F12C**). To avoid potential acquisition of anhysteretic remanent magnetization (ARM) during AF demagnetization, which was observed in discrete sample measurements especially at high AF peak fields (see **"Paleomagnetism"** in the "Site U1422" chapter and **"Paleomagnetism"** in the "Site U1423" chapter [Tada et al., 2015a, 2015b]), we followed the Expedition 318 Scientists (2011) protocol to demagnetize and measure the discrete samples multiple times at each demagnetization level for discrete samples from some of the sites when time allows. At each demagnetization step, discrete samples were first demagnetized along all three axes with the samples placed in the "top-toward" orientation (Fig. **F12D**) followed by measurement. The samples were then demagnetized along all three axes at the same level with the samples placed in the "top-right" orientation followed by measurement. Finally, the samples were demagnetized again at the same level with the samples placed in the "away-up" orientation followed by measurement. For each demagnetization step, averaging the measurements acquired with the samples placed and demagnetized at the three orthogonal orientations should cancel any ARM acquired during AF demagnetization. When there was no time for this protocol, the NRM of the discrete samples was measured with the sample placed in the top-toward or "+*z*-axis toward magnetometer" orientation on the discrete sample tray.

Remanence measurements for all half-core sections and a majority of the discrete samples were made using a 2G Enterprises Model-760R superconducting rock magnetometer (SRM) equipped with direct-current superconducting quantum interference devices (DC-SQUIDs) and an in-line, automated AF demagnetizer capable of reaching a peak field of 80 mT. The coordinate system used for the SRM is shown in Figure **F12C** and **F12D.** The spatial resolution measured by the width at half-height of the pickup coils response is <10 cm for all three axes, although they integrate magnetization over a core length up to 30 cm. The magnetic moment noise level of the cryogenic magnetometer is ~2×10^{-10} Am^2. The practical noise level, however, is affected by the magnetization of the core liner and the background magnetization of the measurement tray, resulting in magnetizations of ~2×10^{-5} A/m that can be reliably measured.

At the beginning of every working shift (approximately every 12 h), we physically cleaned the sample tray with isopropyl alcohol and wiped the backside of the sample tray with antistatic solution. The sample tray was then AF demagnetized with a peak field of 80 mT, followed by remanence measurement to monitor any changes in the sample tray during the course of the expedition and to maintain accurate tray correction values.

NRM measurements of the archive-half core sections were made every 5 cm along the split-core sections, as well as over a 15 cm interval before the sample passed the center of the pick-up coils of the SQUID sensors and a 15 cm interval after the samples had passed through it. Data collected from the two 15 cm intervals beyond the sample are referred to as the leader and trailer measurements and serve the dual function of monitoring the background magnetic moment and allowing for future deconvolution analysis. Typically, we measured NRM before any demagnetization and after AF demagnetization with a peak field of 20 mT. Because core flow (the analysis of one core after the other) through the laboratory dictates the available time for measurements, which was ~2 h per core for Expedition 346, we did not always have time for the optimal number of demagnetization steps.

A suite of discrete samples, selected to characterize typical intervals or to help determine poorly resolved magnetostratigraphy, were subjected to progressive AF demagnetization and measured at 5 mT steps to a peak field of 60 mT and then 10 mT steps to 80 mT when time permitted. This was done to determine whether a characteristic remanent magnetization could be resolved and, if so, what level of demagnetization was required to resolve it. When core flow allowed, we used the SRM with in-line AF demagnetizer to measure NRM of discrete samples before and after AF demagnetization. Discrete samples were placed on a discrete sample tray with each sample separating the adjacent ones by 20 cm to avoid convolution effects of the SRM sensor responses. During busy core flow, we used an ASC D-2000 AF

demagnetizer together with an AGICO JR-6A spinner magnetometer (Fig. F13A, F13B) for remanence measurement of discrete samples before and after AF demagnetization. During measurement, discrete samples were placed in the "automatic folder" of the JR-6A as shown in Figure F13C. Following measurement, the JR-6A data were transformed from the instrument coordinate system to the core coordinate system.

Remanence measurement for the archive-half sections and discrete samples were saved as SRM and DSC files and uploaded to the shipboard LIMS database. To process the shipboard paleomagnetic measurement data, we export formatted data files from both Web Tabular Reports and LIMS Reports. During Expedition 346, we used a modified version of the UPmag program (Xuan and Channell, 2009) to process the shipboard paleomagnetic measurement data and plot and compare downcore variations of various paleomagnetic parameters, as well as to analyze demagnetization data on orthogonal and equal area projections.

During Expedition 346, low-field magnetic susceptibility was measured on whole-core sections using the STMSL and the WRMSL and was measured on archive-half core sections using the SHMSL (see "Physical properties"). The WRMSL and STMSL are equipped with Bartington Instruments MS2C sensors with an internal diameter of 80 mm, which corresponds to a coil diameter of 88 mm. The sensors have a nominal resolution of ~2 × 10^{-6} SI (Blum, 1997). The "units" option for the meters was set on SI units, and the values were stored in the database in raw meter units. To convert to true SI volume susceptibilities, these raw units were multiplied by ~0.68 × 10^{-5} (Blum, 1997). The SHMSL is equipped with a Bartington Instruments MS2E point sensor that measures the susceptibility of an integrated volume of approximately 10.5 mm × 3.8 mm × 4 mm, where 10.5 mm is the length perpendicular to the core axis, 3.8 mm is the width in the core axis, and 4 mm is the depth. Magnetic susceptibility was typically measured every 2.5, 5, or 10 cm for the whole-core sections and every 1 or 2 cm for the split-core sections. We multiply the SHMSL acquired susceptibility stored in the database by a factor of (67/80) × 10^{-5} to empirically convert the measurement to SI volume susceptibilities.

Coring and core orientation

Cores were collected using nonmagnetic core barrels, except at depths where overpull weight was large enough to cause damage to the more expensive nonmagnetic core barrel. In addition, the BHA included a Monel (nonmagnetic) drill collar when the FlexIT core orientation tool was used. The FlexIT tool, which was used for the first hole at each site that succeeded in taking mudline (typically Hole A), uses three orthogonally mounted fluxgate magnetometers to record the orientation of the double lines scribed on the core liner with respect to magnetic north. The tool also has three orthogonally mounted accelerometers to monitor the movement of the drill assembly and help determine when the most stable, and thus useful, core orientation data were gathered. The tool declination, inclination, total magnetic field, and temperature are recorded internally at regular intervals until the tool's memory capacity is filled. For a measurement interval of 6 s, which is what we used, the tool can typically be run for ~24 h, although we aimed to switch tools at least every 8–12 h.

Standard operating procedures for the FlexIT tool are described in the IODP "Core Orientation Standard Operating Procedure" manual (available from the IODP Cumulus database iodp.tamu.edu/tasapps/). This involves synchronizing the instrument to a PC running the FlexIT software and inserting the tool inside a pressure casing. The enclosed tool is then installed on the sinker bars that reside above the core barrel. The double lines on the core liner are aligned relative to the tool. Prior to firing the APC, the core barrel is held stationary (along with the pipe and BHA) for several minutes. During this time, the data are recorded to constrain the core orientation. When the APC fires, the core barrel is assumed to maintain the same orientation, although this and past cruises have found evidence that the core barrel can rotate and/or the core liner can twist as it penetrates the sediment.

Magnetostratigraphy

Magnetic polarity zones (magnetozones) were assigned based on changes in inclinations, as well as distinct ~180° alternations in declination that occur along each stratigraphic section. Sediment disturbance because of coring or geological processes (slumping, faulting, etc.) often leads to distorted and unreliable paleomagnetic directional records and largely alters the sediment fabric. We examined high-resolution shipboard core photographs including both LSIMG (core sections) and COREPHOTO (core composites) from LIMS Reports for each core section (see "Lithostratigraphy") to mark disturbed intervals and avoided using paleomagnetic data from those intervals for magnetostratigraphic interpretations. Once a polarity stratigraphy was established

for a given hole, we correlated the pattern to the GPTS. This was done in close collaboration with the shipboard biostratigraphy team.

During Expedition 346, we used inclination and declination of NRM after 20 mT AF demagnetization for the determination of magnetozones. For cores with FlexIT tool data, declinations were first corrected for core orientation. Magnetostratigraphy for each site was constructed by correlating the magnetozones with the most recent GPTS (Gradstein et al., 2012) summarized in Table **T11** and Figure **F14.** Polarity boundary ages for Chrons C1n–C13n in the Gradstein et al. (2012) timescale are orbitally tuned. We followed the chron terminology of Gradstein et al. (2012) listed in Table **T11.**

Physical properties

High-resolution physical property measurements were made during Expedition 346 to provide information on the bulk physical character of sediment. Such data enhance our understanding of the physicochemical context and history for oceanic deposits and augment lithologic unit characterization while facilitating the correlation of downhole logging data with discrete core measurements and core descriptions. As such, physical property data play a major role in the following tasks:

- Hole-to-hole and site-to-site stratigraphic correlation for construction of composite stratigraphic sections;
- Detection of discontinuities and lateral inhomogeneities, either caused naturally or by the drilling process;
- Obtaining information about differences in the composition and texture of sediment;
- Detection of orbital cycles and tuning to reference sections for stratigraphic purposes; and
- Identification of major seismic reflectors and construction of synthetic seismic profiles.

First, physical properties were measured on whole-round core sections. Core sections are generally 1.5 m in length, so a typical coring length (stroke) of 9.5 m yields six sections plus a shorter seventh section or two shorter sixth and seventh sections. Two core logging systems were used on each section: (1) the STMSL was used on sections immediately after they were sectioned on the catwalk, and (2) at Site U1422 the WRMSL was used on core sections that had warmed to ambient laboratory temperature (20°–21°C). The STMSL houses a GRA bulk densitometer and a magnetic susceptibility sensor loop. The WRMSL employs, in order, a GRA bulk densitometer, a magnetic susceptibility sensor loop, and a compressional *P*-wave velocity sensor.

Simultaneous use of STMSL and WRMSL

Analysis of IODP Site U1423 data demonstrated that thermally equilibrated and unequilibrated GRA and magnetic susceptibility data sets were equivalent to within ±1–2 instrument units. Accordingly, beginning with Site U1423 (and for all sites thereafter), the STMSL and WRMSL were used simultaneously in anticipation of exceptionally fast core recovery at shallow-water sites (300–700 m). We used both tracks in parallel to process each core immediately after recovery (unequilibrated), effectively doubling our speed. This allowed the stratigraphic correlators to assess the alignment of core gaps among holes in real time (before the next core was taken). In this manner, minor adjustments to bit depth prevented gap alignment and missing sections.

The top half of each core (e.g., Sections 1–3) was typically run on the WRMSL and the bottom half (e.g., Sections 4–7) on the STMSL using the exact same settings. These data were all recorded as WRMSL in the LIMS database. In this mode, *P*-wave data was typically collected only on Sections 1–3 because there is no *P*-wave logger on the STMSL.

After STMSL and WRMSL scanning, the whole-round sections were thermally equilibrated and logged through the NGRL. Thermal conductivity was then measured on certain whole-round sections (Section 3 of each core in one hole per site, usually Hole A) by inserting a needle probe into the section through a small hole drilled through the plastic core liner close to the middle of the section. The sections were then split into working and archive halves.

Discrete samples were collected from the working halves, primarily from Hole A, to measure wet bulk density, dry bulk density, water content, porosity, and grain density with MAD procedures. Holes B and C were sampled for MAD samples only to fill significant gaps in the Hole A sample series or if unusual sediment was recovered with no equivalent in Hole A. Automated vane shear device strength measurements on split cores were also taken for Hole A. Archive halves were measured with the SHMSL for obtaining color reflectance (via an Ocean Optics sensor) and magnetic susceptibility using a discrete point-source Bartington probe. A full discussion of

all methodologies and calculations used aboard the *JOIDES Resolution* in the Physical Properties Laboratory is available in Blum (1997).

Special Task Multisensor and Whole-Round Multisensor Loggers

In addition to their intrinsic value for the scientific party, high-resolution STMSL and WRMSL GRA (porosity evaluation) bulk density and magnetic susceptibility data were collected for shipboard core-to-core correlation between drill holes and constructing composite stratigraphic sections. Both tasks had to be completed within a reasonable time to not encumber downstream core processing and sample collection. The quality of STMSL and WRMSL data is highly dependent on the structural integrity of the sediment (cracks, voids, biscuiting, etc.) and the presence of any gaps between the sediment and the core liner. GRA bulk density and magnetic susceptibility were measured nondestructively on all whole-round core sections. *P*-wave velocity was measured until the acoustic signal disappeared because of high attenuation, which typically occurs in sections disturbed by gas expansion voids and cracks.

Gamma ray attenuation bulk density

Bulk density is a function of water-saturated porosity and grain density (dominant mineralogy) and influenced by grain packing and coring disturbance. To measure bulk density, the GRA densitometer uses a 10 mCi ^{137}Cs capsule as a gamma ray source (with the principal energy peak at 0.662 MeV) and a scintillation detector. The narrow collimated peak is attenuated as it passes through the center of the core. Incident photons are scattered by the electrons of the sediment by Compton scattering.

The attenuation of the incident intensity (I_0) is directly related to the electron density in the sediment core of diameter D that can be related to bulk density, provided the average attenuation coefficient (in micrometers) of the sediment is known (Evans, 1965; Harms and Choquette, 1965). Because the attenuation coefficient is similar for most common minerals and aluminum, bulk density is obtained through direct calibration of the densitometer using aluminum rods of different diameters mounted in a core liner filled with distilled water. The spatial resolution was <1 cm.

Magnetic susceptibility

Magnetic susceptibility is a measure of the degree to which a material can be magnetized by an external magnetic field. It provides information on the magnetic composition of the sediment that commonly can be related to mineralogical composition (e.g., terrigenous versus biogenic materials) and diagenetic overprinting. Magnetite and a few other iron oxides and sometimes monosulfides with ferromagnetic characteristics have a specific magnetic susceptibility several orders of magnitude higher than clay, which has paramagnetic properties. Carbonate layers, opal, water, and plastic (core liner) have small negative values of magnetic susceptibility. Calcareous and biogenic deposits with low clay and iron-bearing mineral debris content thus have values approaching the detection limit of magnetic susceptibility instruments.

Magnetic susceptibility was measured on thermally unequilibrated cores (except at Site U1422) using the STMSL and WRMSL units in parallel, with the Bartington Instruments MS2C system. The frequency at which the magnetic susceptibility loop operates is 565 Hz for the WRMSL and STMSL (Blum, 1997). The two units used in parallel were not frequency adjusted but were shielded from interfering with one another using ~2 cm thick aluminum shielding around the STMSL unit. The output of the magnetic susceptibility sensors can be set to centimeter-gram-second (cgs) units or SI units, the IODP standard. However, to obtain dimensionless SI volume-specific magnetic susceptibility values, the instrument units stored in the IODP database must be multiplied by a correction factor (0.68) to compensate for instrument scaling and the geometric ratio between core and loop dimensions (Blum, 1997).

Compressional *P*-wave velocity

P-wave velocity varies with the material's lithology, porosity, bulk density, state of stress, temperature, fabric, and/or degree of fracturing. In sediment and rock, velocity is controlled by the degree of consolidation and lithification, fracturing, and occurrence and abundance of free gas and gas hydrates. Together with bulk density, velocity data are used to calculate acoustic impedance and reflection coefficients to construct synthetic seismic profiles and to estimate the depth of specific seismic horizons.

The *P*-wave velocity sensor measures the ultrasonic *P*-wave velocity of the whole-round sample residing in the core liner. The *P*-wave logger transmits a 500 kHz *P*-wave pulse across the core section at a specified repetition rate.

Traveltime is determined by signal processing software that automatically detects the first arrival of the *P*-wave signal to a precision of 50 ns. Ultrasonic *P*-wave velocity is calculated after correcting for system propagation delay, liner thickness, and liner material velocity.

Natural Gamma Radiation Logger

The NGRL measures gamma rays emitted from whole-round core sections. Gamma rays detected by the logger arise primarily from the decay of U, Th, and K isotopes. In general, high counts identify fine-grained deposits containing K-rich clay minerals and their associated U and Th atoms. The NGR data also show stratigraphic details that aid in core-to-core correlations.

The main NGR detector unit consists of 8 sodium iodide (NaI) scintillator detectors set at a 20 cm interval surrounding the lower half of the section, 7 shielding plastic scintillator detectors, 22 photomultipliers, and passive lead shielding. The NaI detectors are covered by at least 8 cm of lead shielding. In addition, lead separators (~7 cm of low-background lead) are positioned between the NaI detectors. Half of the lead shielding closest to the NaI detectors is composed of low-background lead, whereas the outer half is composed of common lead. In addition to this passive lead shielding, the overlying plastic scintillators detect incoming high-energy gamma and muon cosmic radiation and cancel this signal from the total counted by the NaI detectors.

A measurement run consisted of counting on each core section for 5–10 min (at Position 1), depending on the pace of core recovery. This yields a total of 8 measurements per 150 cm section. For some analyses, Position 2 was chosen to avoid analyzing the disturbed uppermost part of the first section in a core. Therefore, NGR logging required 30–60 min measurement time per core and another ~10 min for core, software, and data handling. Additional information may be found in Vasiliev et al. (2011) and Dunlea et al. (2013).

Thermal conductivity

After NGR measurements were completed, thermal conductivity was measured with the TK04 (Teka Berlin) system using the needle-probe method in full-space configuration for whole-round sediment cores (Von Herzen and Maxwell, 1959). The needle probe contains a heater wire and calibrated thermistor. The probe was inserted into a 2 mm hole drilled through the liner along the splitting line of the core section. To avoid interference from airflow in the laboratory, an insulating jacket of foam rubber was placed over the core section during measurement of thermal conductivity. We also placed the core section inside a large plastic "coffin" to further reduce thermal disturbances.

Three measuring cycles (replicates) were automatically performed at each probe location (normally ~75 cm offset from the top of the section) to calculate average thermal conductivity in the core material. The instrument routinely performed a self-test, which included a drift measurement, at the beginning of each measurement cycle. Once the probe temperature stabilized, the heater circuit was closed and the temperature rise in the probe was recorded. Thermal conductivity was calculated from the rate of temperature rise while the heater current was flowing. Temperatures measured during the first 150 s of the heating cycle were fitted to an approximate solution of a constantly heated line source (for details, see Kristiansen, 1982; Blum, 1997). Thermal conductivity measurements were routinely taken in one hole per site and in one section per core, typically Section 3. Cores retrieved by XCB and RCB typically yield spurious results for thermal conductivity measurements because of the negative effects on the measurement from fluid convection through cracks in the sediment and thereby associated bad coupling of the probe to the sediment.

Moisture and density

After completion of thermal conductivity measurements, whole-round cores were split into working and archive halves. The working halves were placed on the sampling table for the collection of discrete samples to determine wet and dry bulk density, grain density, water content, and porosity. In soft sediment, ~10 cm^3 samples were collected with a plastic syringe 2 cm in diameter, which fits that of the glass vial. To accommodate the large volume of sediment cored and the Rhizon experiments that require MAD data (see **"Geochemistry"**), one or two MAD samples were usually taken and measured per core (usually at 5–7 cm offset from the top of Sections 2 and 5). These locations were selected to provide meaningful measurements for fluid flow by being close to the interstitial water samples in Sections 1 and 4 in addition to providing a judicious spread of samples at each site. This plan also provided the needed flexibility for Rhizon sampling and for choosing a third sample per core when needed for highly variable sediment such as upper organic-rich sediment. This third sample was chosen to complement the regular sample in Section 5 (i.e., the second sample was taken from a light layer if the regular sample was taken from the dark layer and vice versa) to cover the entire spectrum for these sediments' physical properties. For Rhizon sampling (see **"Geochemistry"**), MAD samples were collected in consultation with the Chemistry Laboratory usually at a rate of one sample per section.

Samples were placed in numbered, preweighed 16 mL Wheaton glass vials for wet and dry sediment mass measurements, drying in a convective oven for

24 h, and subject to wet and dry volume measurements. The weights of wet and dry sample masses were determined to a precision of 0.005 g using two Mettler Toledo electronic balances and a computer averaging system to compensate for the ship's motion. Dry sample volume was determined using a hexapycnometer system of a six-celled, custom-configured Micromeritics AccuPyc 1330TC helium-displacement pycnometer. The precision of each cell is <1% of the full-scale volume when properly calibrated and operated. Volume measurement was preceded by three purges of the sample chamber with helium warmed to ~28°C. Three measurement cycles were run for each sample. A reference volume (calibration sphere) was placed sequentially in one of the chambers to check for instrument drift and systematic error. The volumes of the numbered Wheaton vials were calculated before the cruise by multiplying each vial's weight against the average density of the vial glass. Dry mass and volume were measured after samples were heated in an oven at 105° ± 5°C for 24 h and allowed to cool in a desiccator. The procedures for the determination of these physical properties comply with the American Society for Testing and Materials (ASTM) designation (D) 2216 (ASTM International, 1990). The fundamental relation and assumptions for the calculations of all physical property parameters are discussed by Blum (1997) and summarized below.

Mass and volume calculation

Wet mass (M_{wet}), dry mass (M_{dry}), and dry volume (V_{dry}) were measured in the laboratory. The ratio of mass (rm) is a computational constant of 0.965 (i.e., 0.965 g of freshwater per 1 g of seawater). Salt precipitated in sediment pores during the drying process is included in the M_{dry} and V_{dry} values. The mass of the evaporated water (M_{water}) and salt (M_{salt}) in the sample are given by, respectively,

$$M_{water} = M_{wet} - M_{dry},$$

and

$$M_{salt} = M_{water}[s/(1 - s)],$$

where s is the assumed saltwater salinity (0.035%) corresponding to a pore water density (ρ_{pw}) of 1.024 g/cm^3 and a salt density (ρ_{salt}) of 2.22 g/cm^3. The corrected mass of pore water (M_{pw}), volume of pore water (V_{pw}), mass of solids excluding salt (M_{solid}), volume of salt (V_{salt}), volume of solids excluding salt (V_{solid}), and wet volume (V_{wet}) are, respectively,

$$M_{pw} = (M_{wet} - M_{dry})/rm,$$

$$V_{pw} = M_{pw}/\rho_{pw},$$

$$M_{solid} = M_{wet} - M_{pw},$$

$$M_{salt} = M_{pw} - (M_{wet} - M_{dry}),$$

$$V_{salt} = M_{salt}/\rho_{salt},$$

$$V_{wet} = V_{dry} - V_{salt} + V_{pw},$$

and

$$V_{solid} = V_{wet} - V_{pw}.$$

Calculation of bulk properties

For all sediment samples, water content (w) is expressed as the ratio of mass of pore water to wet sediment (total) mass:

$$w = M_{pw}/M_{wet}.$$

Wet bulk density (ρ_{wet}), dry bulk density (ρ_{dry}), sediment grain density (ρ_{solid}), porosity (ϕ), and void ratio (VR) are calculated as

$$\rho_{wet} = M_{wet}/V_{wet},$$

$$\rho_{dry} = M_{solid}/V_{wet},$$

$$\rho_{solid} = M_{solid}/V_{solid},$$

$$\phi = V_{pw}/V_{wet},$$

and

$$VR = V_{pw}/V_{solid}.$$

MAD properties reported and plotted in the "Physical properties" sections of all site chapters were calculated with the MADMax shipboard program.

Section Half Measurement Gantry

Shear strength measurement on split cores was performed using the automated vane shear device on the Section Half Measurement Gantry. We routinely measured one analysis per core in Hole A in Section 2 or 5. Measurements were usually taken at ~20 cm offset from top of section; however, if this interval did not provide good sediment (e.g., caused by high amounts of sand or cracks), different positions were chosen to generate viable data. Cores drilled with XCB or RCB generally often did not provide usable data because of bad sediment/liner contact and disturbed sediment, and thus were measured only in rare cases.

Vane shear strength ($S_{u[v]}$) can be determined by the torque (T) required to cause failure and a vane constant (K_v):

$$S_{u(v)} = T/K_v.$$

All vane shear strength measurements were obtained using a vane with a height of 12.7 mm and a blade length of 6.35 mm. Failure torque was determined by measuring the rotation of a torsional spring using a spring-specific relation between rotation angle and torque.

Section Half Multisensor Logger

Spectrophotometry (color reflectance) and magnetic susceptibility of the archive halves were measured with the SHMSL. Spurious results due to empty intervals, small cracks, and sediment disturbances caused by the drilling process and in places where the core surface is well below the level of the core liner were discarded. Additional detailed information about measurement and interpretation of spectral data can be found in Balsam et al. (1997, 1998), Balsam and Damuth (2000), and Giosan et al. (2002).

Color reflectance

Reflectance of visible light from the archive halves of sediment cores was measured using an Ocean Optics USB4000 spectrophotometer mounted on the automated SHMSL using a diffuse light source. Freshly split soft cores were covered with clear plastic wrap (Glad Wrap) and placed on the instrument track. Measurements with a circular footprint of 8 mm were taken at 1–2 cm spacing to provide a high-resolution stratigraphic record of color variations for visible wavelengths. The 1 cm resolution was employed for lithologic Unit I at sites in the marginal sea where this unit was color variegated. Each measurement recorded in 2 nm wide spectral bands from 400 to 900 nm was reported relative to the center of the measurement footprint. For core intervals that were sufficiently dry to run without Glad Wrap, it was noted that the resulting signal was very much cleaner than the same sections run with Glad Wrap covering.

Magnetic susceptibility

Magnetic susceptibility was measured with a Bartington Instruments MS2E point sensor (high-resolution surface scanning sensor) on discrete points along the SHMSL track. Because the SHMSL requires flush contact between the magnetic susceptibility point sensor and the split core, measurements were made on the archive halves of split cores covered with clear plastic wrap (Glad Wrap). Measurements were taken at 1–2 cm spacing (same as the reflectance measurements) and integrate a volume of 10.5 mm × 3.8 mm × 4 mm, where 10.5 mm is the length perpendicular to the core axis, 3.8 mm is the width in the core axis and 4 mm is the depth. For conversion of the instrument units stored in the IODP database, a correction factor (67/80) must be employed to correct for the relation of the sensor diameter and sediment thickness.

Downhole measurements

Downhole logs are used to determine physical, chemical, and structural properties of the formation penetrated by a borehole. The data are rapidly collected, continuous with depth, and measured in situ; they can be interpreted in terms of the stratigraphy, lithology, mineralogy, magnetic characteristics, and geochemical composition of the penetrated formation. Where core recovery is incomplete or disturbed, log data may provide the only way to characterize the borehole section. Where core recovery is good, log and core data complement one another and may be interpreted together.

Downhole logs measure formation properties on a scale that is intermediate between those obtained from laboratory measurements on core samples and geophysical surveys. They are useful in calibrating the interpretation of geophysical survey data (e.g., through the use of synthetic seismograms) and provide a necessary link for the integrated understanding of physical and chemical properties on all scales.

During Expedition 346, downhole measurements were taken in Holes U1423B, U1425B, U1427A, and U1430B.

Wireline logging

During wireline logging operations, the logs are recorded with a variety of Schlumberger logging tools combined into several tool strings, which are lowered into the hole after completion of coring operations. Two main tool strings were used during Expedition 346. The first tool string is a variation of the triple combination (triple combo) in which the porosity tool has been replaced by a Magnetic Susceptibility Sonde (MSS). We called this modified tool string the paleo combination (paleo combo), and it measured, from top to bottom, resistivity, NGR, density, caliper (borehole diameter), and magnetic susceptibility. The paleo combo was run first at each logged site. The second tool string is the Formation MicroScanner (FMS)-sonic, which provides sonic velocity, FMS resistivity images of the borehole wall, and caliper (Fig. **F15;** Table **T12**). In Hole U1430B, the tool strings were modified to maximize data acquisition in the lowest part of the hole. A short ver-

sion of the paleo combo was run first to acquire NGR, density, and magnetic susceptibility. Another short tool string was run, including resistivity at the top and gamma radiation at the bottom. The FMS-sonic was run as the third tool string. This strategy was successful in acquiring data as deeply as possible. Each tool string also contains an enhanced digital telemetry cartridge (EDTC) for communicating through the wireline to the Schlumberger data acquisition system (MAXIS unit) on the drillship.

In preparation for logging, the boreholes were flushed of debris by circulating drilling fluid and then filled with seawater (Holes U1423B and U1425B) or seawater-based logging gel (sepiolite mud mixed with seawater and weighted with barite; approximate density = 10.5 lb/gal; Holes U1427A and U1430B) to help stabilize the borehole walls. The BHA was pulled up to ~80 m WSF to cover the unstable upper part of the holes. The tool strings were then lowered downhole on a seven-conductor wireline cable before being pulled up at constant speed, typically ~500 m/h, to provide continuous measurements of several properties simultaneously.

Each tool string deployment is termed a logging "run." During each run, tool strings can be lowered down and pulled up the hole several times for control of repeatability or to improve the quality of the data. Each lowering or hauling up of the tool string while collecting data constitutes a "pass." Incoming data were recorded and monitored in real time on the MCM MAXIS logging computer. A wireline heave compensator (WHC) was used to minimize the effect of ship's heave on the tool position in the borehole (see below).

Logged sediment properties and tool measurement principles

The logged properties, and the principles used in the tools to measure them, are briefly described below. The main logs are listed in Table **T13.** More detailed information on individual tools and their geological applications may be found in Serra (1984, 1986, 1989), Schlumberger (1989, 1994), Rider (1996), Goldberg (1997), Lovell et al. (1998), and Ellis and Singer (2007). A complete online list of acronyms for the Schlumberger tools and measurement curves is at **www.apps.slb.com/cmd.**

Natural gamma radioactivity

The Hostile Environment Natural Gamma Ray Sonde (HNGS) was used on both the paleo combo and FMS-sonic tool strings (except in Hole U1423B) to measure NGR in the formation. It uses two bismuth germanate scintillation detectors and five-window spectroscopy to determine concentrations of K (in weight percent), Th (in parts per million), and U (in parts per million) from the characteristic gamma ray energies of isotopes in the ^{40}K, ^{232}Th, and ^{238}U radioactive decay series. The radioactive isotopes of these three elements dominate the natural radiation spectrum. The computation of the elemental abundances uses a least-squares method of extracting U, Th, and K elemental concentrations from the spectral measurements. The HNGS filters out gamma ray energies below 500 keV, eliminating sensitivity to bentonite or KCl in the drilling mud and improving measurement accuracy. The HNGS also provides a measure of the total spectral gamma ray (HSGR) emission and uranium-free or computed gamma ray (HCGR) emission that are measured in American Petroleum Institute units (gAPI). The HNGS response is influenced by the borehole diameter, and therefore the HNGS data are corrected for borehole diameter variations during acquisition.

An additional NGR sensor was housed in the EDTC, which was used primarily to communicate data to the surface. It includes a sodium iodide scintillation detector that measures the total NGR emission of the formation. It is not a spectral tool (does not provide U, Th, and K concentrations), but it provides high-resolution total gamma ray for each pass.

The inclusion of a HNGS sonde in every tool string allows use of the gamma ray data for precise depth match processing between logging strings and passes and for core-log integration.

Density and photoelectric factor

Formation density was measured with the Hostile Environment Litho-Density Sonde (HLDS). The sonde contains a radioactive cesium (^{137}Cs) gamma ray source (622 keV) and far and near gamma ray detectors mounted on a shielded skid, which is pressed against the borehole wall by a hydraulically activated eccentralizing arm (Fig. **F15**). Gamma rays emitted by the source undergo Compton scattering, in which gamma rays are scattered by electrons in the formation. The number of scattered gamma rays that reach the detectors is proportional to the density of electrons in the formation, which is in turn related to bulk density. Porosity may also be derived from this bulk density if the matrix (grain) density is known.

The HLDS also measures the photoelectric factor (PEF) caused by photoelectric absorption of low-energy gamma rays. Photoelectric absorption occurs when their energy falls below 150 keV as a result of being repeatedly scattered by electrons in the formation. The PEF is determined by comparing the

counts from the far detector in the high-energy region, where only Compton scattering occurs, with those in the low-energy region, where the count rates depend on both reactions. Because the PEF depends on the atomic number of the elements in the formation, it also varies according to the chemical composition of the minerals present and can be used for the identification of some minerals. For example, the PEF of calcite = 5.08 b/e$^-$, illite = 3.03 b/e$^-$, quartz = 1.81 b/e$^-$, and kaolinite = 1.49 b/e$^-$. Good contact between the tool and borehole wall is essential for good HLDS logs; poor contact results in underestimation of density values. Both the density correction and caliper measurement of the hole are used to check the contact quality. In Holes U1427A and U1430B, the PEF log should be used with caution, especially in the washouts, because barium in the logging mud may have swamped the signal despite correction from mud effect.

Electrical resistivity

The High-Resolution Laterolog Array (HRLA) tool provides six resistivity measurements with different depths of investigation (including the borehole, or mud resistivity, and five measurements of formation resistivity with increasing penetration into the formation). The tool sends a focused current into the formation and measures the intensity necessary to maintain a constant drop in voltage across a fixed interval, providing direct resistivity measurements. The array has one central (source) electrode and six electrodes above and below it, which serve alternatively as focusing and returning current electrodes. By rapidly changing the role of these electrodes, a simultaneous resistivity measurement at six penetration depths is achieved. The tool is designed to ensure that all signals are measured at exactly the same time and tool position, and to reduce the sensitivity to "shoulder bed" effects when crossing sharp beds thinner than the electrode spacing. The design of the HRLA, which eliminates the need for a surface reference electrode, improves formation resistivity evaluation compared to the traditional dual induction. The HRLA needs to be run centralized in the borehole for optimal results, so knuckle joints were used to centralize the HRLA while allowing the density and magnetic susceptibility tools to maintain good contact with the borehole wall (Fig. **F15**).

Calcite, silica, and hydrocarbons are electrical insulators, whereas ionic solutions such as pore water are conductors. Electrical resistivity, therefore, can be used to evaluate porosity for a given salinity and resistivity of the pore water. Clay surface conduction also contributes to the resistivity values, but at high porosities this is a relatively minor effect.

Acoustic velocity

The Dipole Shear Sonic Imager measures the transit times between sonic transmitters and an array of eight receivers. It combines replicate measurements, thus providing a direct measurement of sound velocity through formations that is relatively free from the effects of formation damage and an enlarged borehole (Schlumberger, 1989). Along with the monopole transmitters found on most sonic tools, it also has two crossed-dipole transmitters, which allow the measurement of shear wave velocity in addition to compressional wave velocity. Dipole measurements are necessary to measure shear velocities in slow formations with shear velocity less than the velocity of sound in the borehole fluid. Such slow formations are typically encountered in deep-ocean drilling.

Formation MicroScanner

The FMS provides high-resolution electrical resistivity–based images of borehole walls. The tool has four orthogonal arms and pads, each containing 16 button electrodes that are pressed against the borehole wall during logging. The electrodes are arranged in two diagonally offset rows of eight electrodes each. A focused current is emitted from the button electrodes into the formation, with a return electrode near the top of the tool. Resistivity of the formation at the button electrodes is derived from the intensity of current passing through the button electrodes.

Processing transforms the resistivity measurements into oriented high-resolution images that reveal the geologic structures of the borehole wall. Features such as bedding, stratification, fracturing, slump folding, and bioturbation can be resolved (Luthi, 1990; Pezard et al., 1990; Salimullah and Stow, 1992; Lovell et al., 1998). Because the images are oriented to magnetic north, further analysis can provide measurement of the dip and direction (azimuth) of planar features in the formation. In addition, when the corresponding planar features can be identified in the recovered core samples, individual core pieces can be reoriented with respect to true north.

Approximately 30% of a borehole with a diameter of 25 cm is imaged during a single pass. Standard procedure is to make two full passes up the borehole with the FMS to maximize the chance of getting full borehole coverage with the pads. The maximum extension of the caliper arms is 40.6 cm (16 inches). In holes with a diameter greater than this maximum, the pad contact at the end of the caliper arms will be inconsistent, and the FMS images may appear out of focus and too conductive. Irregular (rough) borehole walls will also adversely affect the images if contact with the wall is poor.

Magnetic Susceptibility Sonde

The MSS is a nonstandard wireline tool designed by Lamont-Doherty Earth Observatory (LDEO). It measures the ease with which formations are magnetized when subjected to the Earth's magnetic field. The ease of magnetization is ultimately related to the concentration and composition (size, shape, and mineralogy) of magnetizable material within the formation. These measurements provide one of the best methods for investigating stratigraphic changes in mineralogy and lithology because the measurement is quick, repeatable, and nondestructive and because different lithologies often have strongly contrasting susceptibilities. High-resolution susceptibility measurements aid significantly in paleoclimatic and paleoceanographic studies, such as those of Expedition 346, where construction of an accurate and complete stratigraphic framework is critical to reconstruct past climatic changes.

A single-coil sensor was used during Expedition 346 to provide high-resolution measurements (~10 cm) that are shallow reading (~3 cm depth of horizontal investigation). A dual-coil sensor provided lower resolution (~40 cm), deeper reading (~20 cm depth of horizontal investigation) measurements and acted as a quality control for the high-resolution readings because of its more robust nature. The MSS was run as a component of the Schlumberger paleo combo tool string, using a specially developed data translation cartridge.

Magnetic susceptibility data from both the high-resolution and deep-reading sensors are plotted as uncalibrated units. The MSS reading responses are affected by borehole size. The deep-reading sensor electronics are also highly influenced by temperature: higher temperatures lead to higher susceptibility measurements. The acquired magnetic susceptibility data tend to be affected by a nonlinear long period temperature-related drift superimposed on signal variability. Preliminary processing was performed offshore to remove the temperature drift by calculating a least-squares polynomial fit to the data and subtracting the calculated trend from the data set. The residual components from both the high-resolution and deep readings should be an indication of the magnetic signal variability in the formation. When the magnetic susceptibility signal in the sediment is very low, the detection limits of the tool may be reached. For quality control and environmental correction, the MSS also measures internal tool temperature, *z*-axis acceleration, and low-resolution borehole conductivity.

Acceleration and inclinometry

The General Purpose Inclinometer Tool (GPIT) was included in the FMS-sonic tool string to calculate tool acceleration and orientation during logging. Tool orientation is defined by three parameters: tool deviation, tool azimuth, and relative bearing. The GPIT utilizes a three-axis inclinometer and a three-axis fluxgate magnetometer to record the orientation of the FMS as the magnetometer records the magnetic field components (F_x, F_y, and F_z). Thus, the FMS images can be corrected for irregular tool motion, and the dip and direction (azimuth) of features in the FMS image can be determined. Corrections for cable stretching and/or ship heave using GPIT acceleration data (A_x, A_y, and A_z) allow precise determinations of log depths.

Log data quality

The main influence on log data quality is the condition of the borehole wall. Where the borehole diameter varies over short intervals because of washouts or ledges made of layers of harder material, the logs from tools that require good contact with the borehole wall (i.e., the FMS, density, and shallow-reading magnetic susceptibility tools) may be degraded. Deep investigation measurements such as gamma ray, resistivity, and sonic velocity, which do not require contact with the borehole wall, are generally less sensitive to borehole conditions. "Bridged" sections, where borehole diameter is much below the bit size, also cause irregular log results. The quality of the borehole is improved by minimizing the circulation of drilling fluid while drilling, flushing the borehole to remove debris, and logging as soon as possible after drilling and hole conditioning are completed.

The quality of the wireline depth determination depends on several factors. The depth of the logging measurements is determined from the length of the cable payed out from the winch on the ship. The seafloor is identified on the NGR log by the abrupt reduction in gamma ray count at the water/sediment boundary (mudline). Discrepancies between the drilling depth and the wireline log depth may occur. In the case of drilling depth, discrepancies are because of core expansion, incomplete core recovery, or incomplete heave compensation. In the case of log depth, discrepancies between successive runs occur because of incomplete heave compensation, incomplete correction for cable stretch, and cable slip. In the case of very fine sediment in suspension, the mudline can be an elusive datum. Tidal changes in

sea level affect both drilling and logging depths, although these were minimal in the studied region.

Wireline heave compensator

During wireline logging operations, the up-and-down motion of the ship causes a similar motion (heave) of the downhole logging tools. If the amplitude of this motion is large, depth discrepancies can be introduced into the logging data. The risk of damaging downhole instruments is also increased. A WHC system was thus designed to compensate for the vertical motion of the ship and maintain a steady motion of the logging tools to ensure high-quality logging data acquisition (Liu et al., 2013; Iturrino et al., 2013). The WHC uses a vertical accelerometer (motion reference unit [MRU]) positioned under the rig floor near the ship's center of gravity to calculate the vertical motion of the ship with respect to the seafloor. It then adjusts the length of the wireline by varying the distance between two sets of pulleys through which the cable passes in order to minimize downhole tool motion. Real-time measurements of uphole (surface) and downhole acceleration are made simultaneously by the MRU and the EDTC, respectively. An LDEO-developed software package allows these data to be analyzed and compared in real time, displaying the actual motion of the logging tool string and enabling monitoring of the efficiency of the compensator. During Expedition 346, the WHC was used during downhole logging acquisition at Site U1425.

Logging data flow and log depth scales

Data for each wireline logging run were monitored in real time and recorded using the Schlumberger MAXIS 500 system. The initial logging data were referenced to the rig floor (WRF). After logging was completed, the data were shifted to a seafloor reference (WSF), which was based on the step in gamma radiation at the sediment/water interface.

The data were transferred on shore to LDEO, where standardized data processing took place. The main part of the processing is depth matching to remove depth offsets between data from different logging runs, which results in a new depth scale: wireline log matched depth below seafloor (WMSF). Also, corrections are made to certain tools and logs (e.g., FMS imagery is corrected for tool acceleration, including sonde "stick and slip"), documentation for the logs (with an assessment of log quality) is prepared, and the data are converted to ASCII for the conventional logs and GIF for the FMS images. Schlumberger GeoQuest's GeoFrame software package is used for most of the processing of the wireline logging data collected. The data were transferred back to the ship within a few days of logging, and this processed data set was made available to the science party (in ASCII and DLIS formats) through the shipboard IODP logging database and shipboard servers.

Figures presented in the downhole logging sections often combine several depth scales (CSF-A, WSF, and WMSF) and mbsf depth is often used as a general depth term.

In situ temperature measurements

During Expedition 346, in situ temperature measurements were made with the APCT-3 in Hole A. Most commonly, at least four in situ temperature measurements were made at each site. The APCT-3 fits directly into the coring shoe of the APC and consists of a battery pack, a data logger, and a platinum resistance-temperature device calibrated over a temperature range from 0° to 30°C. Before entering the borehole, the tool is first stopped at the mudline for 5 min to thermally equilibrate with bottom water. However, the lowest temperature recorded during the run down was occasionally preferred to the average temperature at the mudline as an estimate of the bottom water temperature because it was more repeatable, and bottom water is expected to have the lowest temperature in the profile. When the APC is plunged into the formation, there is an instantaneous temperature rise from frictional heating. This heat gradually dissipates into the surrounding sediment as the temperature at the APCT-3 equilibrates toward the temperature of the sediment. After the APC penetrated the sediment, it was held in place for 5 min as the APCT-3 recorded the temperature of the cutting shoe every second.

The equilibrium temperature of the sediment was estimated by applying a mathematical heat-conduction model to the temperature decay record (Horai and Von Herzen, 1985). The synthetic thermal decay curve for the APCT-3 is a function of the geometry and thermal properties of the probe and the sediment (Bullard, 1954; Horai and Von Herzen, 1985). The equilibrium temperature was estimated by applying a fitting procedure (Pribnow et al., 2000). However, where the APC did not achieved a full stroke or where ship heave pulled the APC up from full penetration, the temperature equilibration curve was disturbed and temperature determination was less accurate. The nominal accuracy of the APCT-3 temperature measurements is ±0.05°C.

The APCT-3 temperature data were combined with measurements of thermal conductivity (see **"Physical properties"**) obtained from whole-core samples to obtain heat flow values. Heat flow was calculated

according to the Bullard method, to be consistent with the synthesis of ODP heat flow data by Pribnow et al. (2000).

Stratigraphic correlation and sedimentation rates

Meeting the scientific objectives of Expedition 346 required recovery of complete stratigraphic sections. Such sections cannot be constructed from a single IODP hole because core-recovery gaps on the order of 20–50 cm occur between successive cores despite 100% or greater nominal recovery (e.g., Ruddiman, Kidd, Thomas, et al., 1987; Hagelberg et al., 1995; Acton et al., 2001). The construction of a complete stratigraphic section, referred to as a splice, requires combining stratigraphic intervals from two or more offset holes cored at the same site.

Core depth below seafloor (CSF-A) scale

The depth to the top of each core is based on the DSF scale. DSF is a drill string measurement, determined by the length of the drill string below the rig floor to the top of the cored interval minus the length of the drill string from the rig floor to the mudline (which is assumed to be the seafloor). The depth to a given position within a core is determined by adding to the core top depth the distance that position occurs from the top of the core. The distance the position occurs from the top of the core includes expansion due to relief of overburden as well as gas expansion. This depth scale is referred to as CSF-A (Fig. **F16**) and is equivalent to the historical DSDP, ODP, and IODP mbsf scale (IODP Depth Scales, **www.iodp.org/program-policies/procedures/guidelines/**). Error in the CSF-A scale includes pipe and BHA stretch and compression, tides, and uncompensated heave, as well as incomplete recovery and core expansion as a result of elastic rebound and gas. Tidal influence on this depth measurement was first predicted during ODP Leg 138 (Hagelberg et al., 1995) and proven during ODP Leg 202 (Mix, Tiedemann, Blum, et al., 2003). Because tidal variations are predictable, pipe offsets can be adjusted to account for these cyclical changes in sea level, which helps avoid core gap alignment among holes. During this expedition, tidal ranges were not a factor and were not accounted for. In any case, the goal of avoiding core gap alignment can be difficult to achieve with just two holes and sometimes even with three.

Core composite depth below seafloor (CCSF-A) scale

The goal of constructing a composite depth scale for a given site is to place specific coeval, laterally continuous features identified in all drilled holes into a common frame of reference by depth shifting individual cores (each starting on the CSF-A scale). The resulting CCSF-A scale is equivalent to the historical ODP and IODP meters composite depth (mcd) scale. In constructing the CCSF-A scale, the depths of the individual cores are shifted by a constant amount (there is no stretching or squeezing within individual cores). This provides good first-order correlation between cores from different holes, provides estimates of the length of coring gaps, and provides a basis upon which higher order composite depth scales are constructed; compositing is a prerequisite to developing the CCSF-D scale (spliced record). The CCSF-A scale is built by correlating features downhole from the sedimentological mudline (typically the top of a core with a well-preserved sediment/water interface). This establishes the top of the stratigraphic section and anchors the entire composite depth scale for all cores from all holes at a site. In practice, compositing is accomplished sequentially by establishing specific tie points among the various holes, working from the mudline (anchor) core to the bottom of the drilled section, as illustrated by the red tie point arrows in Figure **F16.** Core intervals between the tie points are used to construct the splice as discussed below. As such, tie points should be chosen such that disturbed intervals are avoided. The mudline (or anchor) core is typically the only core in which the depths are the same for both the CSF-A and CCSF-A scales. The CCSF-A scale very rarely (if ever) results in alignment of all features because of the differing effects of coring-induced stretching and squeezing among cores as well as hole-to-hole sedimentological differences (Fig. **F16**).

The vertical depth offset of every core in every hole is tabulated in an affine table. Conceptually, it should be possible to correlate (“tie”) each successive core in one hole to a core from an adjacent hole, all the way to the bottom of a drilled section, provided between-core gaps never come into alignment among all holes at a site and recovery is sufficiently high. Aligned coring gaps across all holes cored at a site may still occur, in which case cores below the gap are no longer tied to the mudline core but can often still be tied to one another. Such intervals are commonly referred to as “floating” spliced sections.

During the process of constructing the composite section, the CCSF-A depth becomes systematically larger than that of the CSF-A depth at equivalent horizons. This expansion, which is typically ~5%–15%, is mostly caused by decompression of the cores as they are brought to the surface, gas expansion, stretching that occurs as part of the coring process, and/or curation when, for example, material that has fallen downhole or gas expansion voids are curated as part of the core (e.g., Hagelberg et al., 1995; Acton et al., 2001).

Core composite depth below seafloor (CCSF-D) scale; the splice

Once the CCSF-A scale has been developed and the between-core gaps identified, a complete stratigraphic section (splice) is constructed by combining selected intervals between the previously established tie points. The depth scale is designated the CCSF-D scale (Fig. F16).

Although CCSF-D is merely a subset of the CCSF-A, this -D designation applies only to intervals included in the splice. Intervals not included in the primary splice, including any alternate splice(s), retain the CCSF-A scale. Should coring gaps happen to align across all holes drilled at a site, the spliced sections below are "appended" to those above and referred to as floating splice sections (i.e., not tied to the mudline). In this case, the amount of missing material between floating sections can be measured using downhole logs. Where no logs are available, the CSF-A scale provides a reasonably accurate estimate of the length of the missing section, especially when coring in calm seas.

Core composite depth below seafloor (CCSF-C) scale

Once the splice is constructed, it is sometimes possible (and often useful) to map into the splice those intervals not included in the splice itself. This can be accomplished using the core-log integration functionality in the Correlator software by treating the splice as a downhole log. The methodology is based on identification of correlative tie points at very high resolution (cycle by cycle), with linear adjustments of data between ties. This is designated as the CCSF-C scale and can be thought of as an "equivalent splice depth." In the best case scenario, the CCSF-C and CCSF-D scales are equivalent. In reality, they are only equivalent to the extent that the correlations are accurate. These depth-depth mapping functions, if available, are provided in table form for specific sites. At core boundaries, where strong stretching and compression are prevalent, these detailed depth maps are less accurate. Users are encouraged to plot data on the CCSF-C scale along with the same set of data on the splice (CCSF-D scale) in order to assess whether or not the CCSF-C scale is sufficiently accurate for the intended use.

Measurements and methods for correlation

The composite sections and splices are based on the stratigraphic correlation of data sets acquired from the WRMSL, STMSL, digitized red, green, and blue (RGB) color data extracted from core images acquired from the SHIL, and reflectance data from the SHMSL. During this expedition we used the WRMSL and STMSL in parallel as described in detail in **"Physical properties."** This allowed stratigraphic correlation to take place in real time such that bit depth could be adjusted as necessary to avoid alignment of core gaps among holes.

The data sets used for compositing and splicing include magnetic susceptibility, GRA, and various color reflectance data sets (e.g., R, G, and B and L*, a*, and b*). Magnetic susceptibility and GRA were measured at 2.5 or 5 cm intervals, whereas R, G, and B values were calculated at 0.5 cm intervals in the form of 0.5 cm averages measured continuously along a 1.5 cm wide strip centered on digital color SHIL images. Details on instrument calibrations, settings, and measurement intervals for Expedition 346 are given in **"Lithostratigraphy"** and **"Physical properties."**

Compositing and splicing was accomplished using Correlator software (v 1.695), from which we generated standard affine tables (listings of the vertical offset [m] added to each core in order to generate the CCSF-A scales) and splice interval tables (listings of the specific core intervals used to construct the splice). These tables were uploaded into the LIMS database, from which all users are able to attach the appropriate depth scale to any data set. In most cases, the detailed splice was constructed on the basis of blue (B) data acquired after the cores were split and imaged.

At sites with significant gas expansion, where voids developed within the liner, holes were drilled to relieve the pressure, and voids were reduced using plungers. In addition, the splitting process sometimes caused sediment to be moved upsection (sections are split bottom to top). Curators then further consolidated voids within each section on both the working and archive halves. For these reasons, the WRMSL and STMSL magnetic susceptibility and GRA data may not agree with the blue data when plotted on the CCSF-D scale.

Age models and sedimentation rates

Preliminary age models and sedimentation rates were generated for each site considering all available datums generated by the Biostratigraphy, Paleomagnetism, and Lithostratigraphy (tephra) groups. Based on these shipboard results, the most likely depth-age relationship was constructed based on the following criteria:

- Paleomagnetic datums, where present, were used preferentially.
- Where appropriate, the depth-age line was set between the lower and upper limits given by LO and FO, respectively, of biostratigraphic datums.
- Within a lithologic unit, the number of inflection points was minimized.

Linear or higher order fits were applied to the data satisfying above criteria to generate preliminary age models. The age model was then used to assess sedimentation rates between lithologic boundaries established by the Lithostratigraphy group.

References

Acton, G.D., Borton, C.J., and the Leg 178 Shipboard Scientific Party, 2001. Palmer Deep composite depth scales for Leg 178 Sites 1098 and 1099. *In* Barker, P.F., Camerlenghi, A., Acton, G.D., and Ramsay, A.T.S. (Eds.), *Proc. ODP, Sci. Results,* 178: College Station, TX (Ocean Drilling Program), 1–35. **doi:10.2973/odp.proc.sr.178.202.2001**

Adkins, J.F., McIntyre, K., and Schrag, D.P., 2002. The salinity, temperature, and $\delta^{18}O$ of the glacial deep ocean. *Science,* 298(5599):1769–1773. **doi:10.1126/science.1076252**

Alexandrovich, J.M., 1992. Radiolarians from Sites 794, 795, 796, and 797 (Japan Sea). *In* Pisciotto, K.A., Ingle, J.C., Jr., von Breymann, M.T., Barron, J., et al., *Proc. ODP, Sci. Results,* 127/128 (Pt. 1): College Station, TX (Ocean Drilling Program), 291–307. **doi:10.2973/odp.proc.sr.127128-1.134.1992**

ASTM International, 1990. Standard method for laboratory determination of water (moisture) content of soil and rock (Standard D2216–90). In *Annual Book of ASTM Standards for Soil and Rock* (Vol. 04.08): Philadelphia (Am. Soc. Testing Mater.). [revision of D2216-63, D2216-80]

Balsam, W.L., and Damuth, J.E., 2000. Further investigations of shipboard vs. shore-based spectral data: implications for interpreting Leg 164 sediment composition. *In* Paull, C.K., Matsumoto, R., Wallace, P., and Dillon, W.P. (Eds.), *Proc. ODP, Sci. Results,* 164: College Station, TX (Ocean Drilling Program), 313–324. **doi:10.2973/odp.proc.sr.164.222.2000**

Balsam, W.L., Damuth, J.E., and Schneider, R.R., 1997. Comparison of shipboard vs. shore-based spectral data from Amazon Fan cores: implications for interpreting sediment composition. *In* Flood, R.D., Piper, D.J.W., Klaus, A., and Peterson, L.C. (Eds.), *Proc. ODP, Sci. Results,* 155: College Station, TX (Ocean Drilling Program), 193–215. **doi:10.2973/odp.proc.sr.155.210.1997**

Balsam, W.L., Deaton, B.C., and Damuth, J.E., 1998. The effects of water content on diffuse reflectance spectrophotometry studies of deep-sea sediment cores. *Mar. Geol.,* 149(1–4):177–189. **doi:10.1016/S0025-3227(98)00033-4**

Barron, J.A., and Gladenkov, A.Y., 1995. Early Miocene to Pleistocene diatom stratigraphy of Leg 145. *In* Rea, D.K., Basov, I.A., Scholl, D.W., and Allan, J.F. (Eds.), *Proc. ODP, Sci. Results,* 145: College Station, TX (Ocean Drilling Program), 3–19. **doi:10.2973/odp.proc.sr.145.101.1995**

Berggren, W.A, Hilgen, F.J., Langereis, C.G., Kent, D.V., Obradovich, J.D., Raffi, I., Raymo, M.E., and Shackelton, N.J., 1995a. Late Neogene chronology: new perspectives in high-resolution stratigraphy. *Geol. Soc. Am. Bull.,* 107(11):1272–1287. **doi:10.1130/0016-7606(1995)107<1272:LNCNPI>2.3.CO;2**

Berggren, W.A., Kent, D.V., Swisher, C.C., III, and Aubry, M.-P., 1995b. A revised Cenozoic geochronology and chronostratigraphy. *In* Berggren, W.A., Kent, D.V., Aubry, M.-P., and Hardenbol, J. (Eds.), *Geochronology, Time Scales and Global Stratigraphic Correlation*. Spec. Publ.—SEPM (Soc. Sediment. Geol.), 54:129–212. **doi:10.2110/pec.95.04.0129**

Blum, P., 1997. Physical properties handbook: a guide to the shipboard measurement of physical properties of deep-sea cores. *ODP Tech. Note,* 26. **doi:10.2973/odp.tn.26.1997**

Boersma, A., 1984. *A Handbook of Common Tertiary* Uvigerina: Stony Point, NY (Microclimates Press).

Bolli, H.M., and Saunders, J.B., 1985. Oligocene to Holocene low latitude planktic foraminifera. *In* Bolli, H.M., Saunders, J.B., and Perch-Nielsen, K. (Eds.), *Plankton Stratigraphy* (Vol. 1): *Planktic Foraminifera, Calcareous Nannofossils and Calpionellids:* Cambridge (Cambridge Univ. Press), 155–262.

Bown, P.R. (Ed.), 1998. *Calcareous Nannofossil Biostratigraphy:* Dordrecht, The Netherlands (Kluwer Academic Publ.).

Briucaud, A., Morel, A., and Prieur, L., 1981. Absorption by dissolved organic matter of the sea (yellow substance) in the UV and visible domains. *Limnol. Oceanogr.,* 26(1):43–53. **doi:10.4319/lo.1981.26.1.0043**

Brunner, C.A., 1992. Paleoenvironment and biostratigraphy of foraminifers at Sites 794, 795, 796, and 797 in the Japan Sea. *In* Pisciotto, K.A., Ingle, J.C., Jr., von Breymann, M.T., Barron, J., et al., *Proc. ODP, Sci. Results,* 127/128 (Pt. 1): College Station, TX (Ocean Drilling Program), 187–224. **doi:10.2973/odp.proc.sr.127128-1.124.1992**

Bullard, E.C., 1954. The flow of heat through the floor of the Atlantic Ocean. *Proc. R. Soc. London, Ser. A,* 222(1150):408–429. **doi:10.1098/rspa.1954.0085**

Cande, S.C., and Kent, D.V., 1992. A new geomagnetic polarity time scale for the Late Cretaceous and Ceno-

zoic. *J. Geophys. Res.: Solid Earth,* 97(B10):13917–13951. doi:10.1029/92JB01202

Chaisson, W.P., and Leckie, R.M., 1993. High-resolution Neogene planktonic foraminifer biostratigraphy of Site 806, Ontong Java Plateau (western equatorial Pacific). *In* Berger, W.H., Kroenke, L.W., Mayer, L.A., et al., *Proc. ODP, Sci. Results,* 130: College Station, TX (Ocean Drilling Program), 137–178. doi:10.2973/odp.proc.sr.130.010.1993

Chaisson, W.P., and Pearson, P.N., 1997. Planktonic foraminifer biostratigraphy at Site 925: middle Miocene–Pleistocene. *In* Shackleton, N.J., Curry, W.B., Richter, C., and Bralower, T.J. (Eds.), *Proc. ODP, Sci. Results,* 154: College Station, TX (Ocean Drilling Program), 3–31. doi:10.2973/odp.proc.sr.154.104.1997

Chapronière, G.C.H., Styzen, M.J., Sager, W.W., Nishi, H., Quinterno, P.J., and Abrahamsen, N., 1994. Late Neogene biostratigraphic and magnetostratigraphic synthesis, Leg 135. *In* Hawkins, J., Parson, L., Allan, J., et al., *Proc. ODP, Sci. Results,* 135: College Station, TX (Ocean Drilling Program), 857–877. doi:10.2973/odp.proc.sr.135.116.1994

Cline, J.D., 1969. Sectrophotometric determination of hydrogen sulfide in natural waters. *Limnol. Oceanogr.,* 14(3):454–458. doi:10.4319/lo.1969.14.3.0454

D'Hondt, S.L., Jørgensen, B.B., Miller, D.J., et al., 2003. *Proc. ODP, Init. Repts.,* 201: College Station, TX (Ocean Drilling Program). doi:10.2973/odp.proc.ir.201.2003

Dickens, G.R., Koelling, M., Smith, D.C., Schneiders, L., and the IODP Expedition 302 Scientists, 2007. Rhizon sampling of pore waters on scientific drilling expeditions: an example from the IODP Expedition 302, Arctic Coring Expedition (ACEX). *Sci. Drill.,* 4:22–25. doi:10.2204/iodp.sd.4.08.2007

Droser, M.L., and Bottjer, D.J., 1986. A semiquantitative field classification of ichnofabric. *J. Sediment. Res.,* 56(4):558–559. doi:10.1306/212F89C2-2B24-11D7-8648000102C1865D

Dunlea, A.G., Murray, R.W., Harris, R.N., Vasiliev, M.A., Evans, H., Spivack, A.J., and D'Hondt, S., 2013. Assessment and use of NGR instrumentation on the *JOIDES Resolution* to quantify U, Th, and K concentrations in marine sediment. *Sci. Drill.,* 15:57–63. doi:10.2204/iodp.sd.15.05.2013

Ellis, D.V., and Singer, J.M., 2007. *Well Logging for Earth Scientists* (2nd ed.): New York (Elsevier).

Evans, H.B., 1965. GRAPE—a device for continuous determination of material density and porosity. *Trans. SPWLA Annu. Logging Symp.:* 6(2):B1–B25. http://www.spwla.org/cgi-bin/shop.pl?choice=display;item_id=82

Expedition 303 Scientists, 2006. Site U1302–U1308 methods. *In* Channell, J.E.T., Kanamatsu, T., Sato, T., Stein, R., Alvarez Zarikian, C.A., Malone, M.J., and the Expedition 303/306 Scientists, *Proc. IODP,* 303/306: College Station, TX (Integrated Ocean Drilling Program Management International, Inc.). doi:10.2204/iodp.proc.303306.102.2006

Expedition 318 Scientists, 2011. Methods. *In* Escutia, C., Brinkhuis, H., Klaus, A., and the Expedition 318 Scientists, *Proc. IODP,* 318: Tokyo (Integrated Ocean Drilling Program Management International, Inc.). doi:10.2204/iodp.proc.318.102.2011

Expedition 320/321 Scientists, 2010a. Methods. *In* Pälike, H., Lyle, M., Nishi, H., Raffi, I., Gamage, K., Klaus, A., and the Expedition 320/321 Scientists, *Proc. IODP,* 320/321: Tokyo (Integrated Ocean Drilling Program Management International, Inc.). doi:10.2204/iodp.proc.320321.102.2010

Expedition 320/321 Scientists, 2010b. Site U1331. *In* Pälike, H., Lyle, M., Nishi, H., Raffi, I., Gamage, K., Klaus, A., and the Expedition 320/321 Scientists, *Proc. IODP,* 320/321: Tokyo (Integrated Ocean Drilling Program Management International, Inc.). doi:10.2204/iodp.proc.320321.103.2010

Expedition 339 Scientists, 2013. Site U1385. *In* Stow, D.A.V., Hernández-Molina, F.J., Alvarez Zarikian, C.A., and the Expedition 339 Scientists, *Proc. IODP,* 339: Tokyo (Integrated Ocean Drilling Program Management International, Inc.). doi:10.2204/iodp.proc.339.103.2013

Expedition 342 Scientists, 2012. Paleogene Newfoundland sediment drifts. *IODP Prel. Rept.,* 342. doi:10.2204/iodp.pr.342.2012

Fatela, F., and Taborda, R., 2002. Confidence limits of species proportions in microfossil assemblages. *Mar. Micropaleontol.,* 45(2):169–174. doi:10.1016/S0377-8398(02)00021-X

Fisher, R.V., and Schmincke, H.-U., 1984. *Pyroclastic Rocks:* Berlin (Springer-Verlag).

Gieskes, J.M., 1975. Chemistry of interstitial waters of marine sediments. *Annu. Rev. Earth Planet. Sci.,* 3:433–453. doi:10.1146/annurev.ea.03.050175.002245

Gieskes, J.M., Gamo, T., and Brumsack, H., 1991. Chemical methods for interstitial water analysis aboard *JOIDES Resolution. ODP Tech. Note,* 15. doi:10.2973/odp.tn.15.1991

Giosan, L., Flood, R.D., and Aller, R.C., 2002. Paleoceanographic significance of sediment color on western North Atlantic drifts: I. Origin of color. *Mar. Geol.,* 189(1–2):25–41. doi:10.1016/S0025-3227(02)00321-3

Gladenkov, A.Y., 2003. Diatom biostratigraphy of the Neogene Milky River Formation, Alaska Peninsula, southwestern Alaska. *Proc. Calif. Acad. Sci.,* 54(3):27–64. http://researcharchive.calacademy.org/research/scipubs/pdfs/v54/proccas_v54_n03.pdf

Goldberg, D., 1997. The role of downhole measurements in marine geology and geophysics. *Rev. Geophys.,* 35(3):315–342. doi:10.1029/97RG00221

Gradstein, F.M., Ogg, J.G., Schmitz, M.D., and Ogg, G.M. (Eds.)., 2012. *The Geological Time Scale 2012:* Amsterdam (Elsevier).

Hagelberg, T.K., Pisias, N.G., Shackleton, N.J., Mix, A.C., and Harris, S., 1995. Refinement of a high-resolution, continuous sedimentary section for studying equatorial Pacific Ocean paleoceanography, Leg 138. *In* Pisias, N.G., Mayer, L.A., Janecek, T.R., Palmer-Julson, A., and van Andel, T.H. (Eds.), *Proc. ODP, Sci Results,* 138: College Station, TX (Ocean Drilling Program), 31–46. doi:10.2973/odp.proc.sr.138.103.1995

Hanagata, S., 2003. Miocene–Pliocene foraminifera from the Niigata oil-fields region, northeastern Japan. *Micropalaeontology,* 49(4):293–340. **doi:10.2113/49.4.293**

Hanagata, S., and Hiramatsu, C., 2005. Miocene–Pliocene foraminifera from the subsurface sections in the Yufutsu oil and gas field, Hokkaido. *Paleontol. Res.,* 9(4):273–298. **doi:10.2517/prpsj.9.273**

Hanagata, S., Motoyama, I., and Miwa, M., 2001. Geologic ages of the last occurrence of *Spirosigmoilinella compressa* and first occurrence of *Miliammina echigoensis* (benthic foraminifera), and their paleoceanographic implications: response to the latest Miocene–earliest Pliocene sea level changes. *J. Geol. Soc. Jpn.,* 107(2):101–116. (in Japanese with English abstract) **doi:10.5575/geosoc.107.101**

Harms, J.C., and Choquette, P.W., 1965. Geologic evaluation of a gamma-ray porosity device. *Trans. SPWLA Annu. Logging Symp.:* 6(2):C1–C37.

Hayward, B.W., 2002. Late Pliocene to middle Pleistocene extinctions of deep-sea benthic foraminifera ("*Stilostomella* extinction") in the southwest Pacific. *J. Foraminiferal Res.,* 32(3):274–307. **doi:10.2113/32.3.274**

Hoiles, P.W., Gallagher, S.J., Kitamura, A., and Southwood, J.M., 2012. The evolution of the Tsushima Current during the early Pleistocene in the Sea of Japan: an example from marine isotope stage (MIS) 47. *Global Planet. Change*, 92–93:162–178. **doi:10.1016/j.gloplacha.2012.05.015**

Holbourn, A., Henderson, A.S., and MacLeod, N., 2013. *Atlas of Benthic Foraminifera:* Chichester (John Wiley & Sons, Ltd.). **doi:10.1002/9781118452493**

Horai, K., and Von Herzen, R.P., 1985. Measurement of heat flow on Leg 86 of the Deep Sea Drilling Project. *In* Heath, G.R., Burckle, L.H., et al., *Init. Repts. DSDP,* 86: Washington, DC (U.S. Govt. Printing Office), 759–777. **doi:10.2973/dsdp.proc.86.135.1985**

Ingle, J.C., Jr., Suyehiro, K., von Breymann, M.T., et al., 1990. *Proc. ODP, Init. Repts.,* 128: College Station, TX (Ocean Drilling Program). **doi:10.2973/odp.proc.ir.128.1990**

Itaki, T., Komatsu, N., and Motoyama, I., 2007. Orbital- and millennial-scale changes of radiolarian assemblages during the last 220 kyrs in the Japan Sea. *Palaeogeogr., Palaeoclimatol., Palaeoecol.,* 247(1–2):115–130. **doi:10.1016/j.palaeo.2006.11.025**

Iturrino, G., Liu, T., Goldberg, D., Anderson, L., Evans, H., Fehr, A., Guerin, G., Inwood, J., Lofi, J., Malinverno, A., Morgan, S., Mrozewski, S., Slagle, A., and Williams, T., 2013. Performance of the wireline heave compensation system onboard D/V *JOIDES Resolution. Sci. Drill.,* 15:46–50. **doi:10.2204/iodp.sd.15.08.2013**

Jones, R.W., 1994. *The Challenger Foraminifera:* New York (Oxford Univ. Press).

Kamikuri, S., 2010. New late Neogene radiolarian species from the middle to high latitudes of the North Pacific. *Rev. Micropaleontol.,* 53(2):85–106. **doi:10.1016/j.revmic.2008.06.005**

Kamikuri, S., Motoyama, I., Nishi, H., and Iwai, M., 2009. Neogene radiolarian biostratigraphy and faunal evolution rates in the eastern equatorial Pacific ODP Sites 845 and 1241. *Acta Palaeontol. Pol.,* 54(4):713–742. **doi:10.4202/app.2008.0076**

Kamikuri, S., Nishi, H., and Motoyama, I., 2007. Effects of late Neogene climatic cooling on North Pacific radiolarian assemblages and oceanographic conditions. *Palaeogeogr., Palaeoclimatol., Palaeoecol.,* 249(3–4):370–392. **doi:10.1016/j.palaeo.2007.02.008**

Kamikuri, S., Nishi, H., Motoyama, I., and Saito, S., 2004. Middle Miocene to Pleistocene radiolarian biostratigraphy in the Northwest Pacific Ocean, ODP Leg 186. *Isl. Arc,* 13(1):191–226. **doi:10.1111/j.1440-1738.2003.00421.x**

Kaminski, M.A., and Gradstein, F.M., 2005. Atlas of Paleogene cosmopolitan deep-water agglutinated foraminifera. *Grzybowski Found. Spec. Publ.,* 10. **http://www.foraminifera.eu/atlas.html**

Kato, M., 1992. Benthic foraminifers from the Japan Sea: Leg 128. *In* Pisciotto, K.A., Ingle, J.C., Jr., von Breymann, M.T., Barron, J., et al., *Proc. ODP, Sci. Results,* 127/128 (Pt. 1): College Station, TX (Ocean Drilling Program), 365–392. **doi:10.2973/odp.proc.sr.127128-1.142.1992**

Katz, M.E., and Miller, K.G., 1991. Early Paleogene benthic foraminiferal assemblages and stable isotopes in the Southern Ocean. *In* Ciesielski, P.F., Kristoffersen, Y., et al., *Proc. ODP, Sci. Results,* 114: College Station, TX (Ocean Drilling Program), 481–512. **doi:10.2973/odp.proc.sr.114.147.1991**

Kennett, J.P., and Srinivasan, M.S., 1983. *Neogene Planktonic Foraminifera: A Phylogenetic Atlas:* Stroudsburg, PA (Hutchinson Ross).

Kim, J.-H., Torres, M.E., Hong, W.-L., Choi, J., Riedel, M., Bahk, J.-J., and Kim, S.-H., 2013. Pore fluid chemistry from the second gas hydrate drilling expedition in the Ulleung Basin (UBGH2): source, mechanisms and consequences of fluid freshening in the central part of the Ulleung Basin, East Sea. *Mar. Pet. Geol.,* 47:99–112. **doi:10.1016/j.marpetgeo.2012.12.011**

Koizumi, I., 1992. Diatom biostratigraphy of the Japan Sea: Leg 127. *In* Pisciotto, K.A., Ingle, J.C., Jr., von Breymann, M.T., Barron, J., et al., *Proc. ODP, Sci. Results,* 127/128 (Pt. 1): College Station, TX (Ocean Drilling Program), 249–289. **doi:10.2973/odp.proc.sr.127128-1.127.1992**

Kristiansen, J.I., 1982. The transient cylindrical probe method for determination of thermal parameters of earth materials [Ph.D. dissert.]. Åarhus Univ., Åarhus, Denmark.

Kucera, M., and Kennett, J.P., 2000. Biochronology and evolutionary implications of late Neogene California margin planktonic foraminiferal events. *Mar. Micropaleontol.,* 40(1–2):67–81. **doi:10.1016/S0377-8398(00)00029-3**

Lagoe, M.B., and Thompson, P.R., 1988. Chronostratigraphic significance of late Cenozoic planktonic foraminifera from the Ventura Basin, California: potential for improving tectonic and depositional interpretation. *J. Foraminiferal Res.,* 18(3):250–266. **doi:10.2113/gsjfr.18.3.250**

Leckie, R.M., Farnham, C., and Schmidt, M.G., 1993. Oligocene planktonic foraminifer biostratigraphy of Hole 803D (Ontong Java Plateau) and Hole 628A (Little Bahama Bank), and comparison with the southern high latitudes. *In* Berger, W.H., Kroenke, L.W., Mayer, L.A., et al., *Proc. ODP, Sci. Results,* 130: College Station, TX (Ocean Drilling Program), 113–136. **doi:10.2973/odp.proc.sr.130.012.1993**

Ling, H.-Y., 1992. Radiolarians from the Sea of Japan: Leg 128. *In* Pisciotto, K.A., Ingle, J.C., Jr., von Breymann, M.T., Barron, J., et al., *Proc. ODP, Sci. Results,* 127/128 (Pt. 1): College Station, TX (Ocean Drilling Program), 225–236. **doi:10.2973/odp.proc.sr.127128-1.125.1992**

Liu, T., Iturrino, G., Goldberg, D., Meissner, E., Swain, K., Furman, C., Fitzgerald, P., Frisbee, N., Chlimoun, J., Van Hyfte, J., and Beyer, R., 2013. Performance evaluation of active wireline heave compensation systems in marine well logging environments. *Geo-Mar. Lett.,* 33(1):83–93. **doi:10.1007/s00367-012-0309-8**

Loeblich, A.R., Jr., and Tappan, H., 1988. *Foraminiferal Genera and Their Classification:* New York (Van Nostrand Reinhold).

Lourens, L., Hilgen, F., Shackleton, N.J., Laskar, J., and Wilson, D., 2004. The Neogene period. *In* Gradstein, F.M., Ogg, J.G., and Smith, A. (Eds.), *A Geologic Time Scale 2004:* Cambridge (Cambridge Univ. Press), 409–440. **doi:10.1017/CBO9780511536045.022**

Lovell, M.A., Harvey, P.K., Brewer, T.S., Williams, C., Jackson, P.D., and Williamson, G., 1998. Application of FMS images in the Ocean Drilling Program: an overview. *In* Cramp, A., MacLeod, C.J., Lee, S.V., and Jones, E.J.W. (Eds.), *Geological Evolution of Ocean Basins: Results from the Ocean Drilling Program.* Geol. Soc. Spec. Publ., 131(1):287–303. **doi:10.1144/GSL.SP.1998.131.01.18**

Luthi, S.M., 1990. Sedimentary structures of clastic rocks identified from electrical borehole images. *In* Hurst, A., Lovell, M.A., and Morton, A.C. (Eds.), *Geological Applications of Wireline Logs*. Geol. Soc. Spec. Publ., 48(1):3–10. **doi:10.1144/GSL.SP.1990.048.01.02**

Lyle, M., Koizumi, I., Richter, C., et al., 1997. *Proc. ODP, Init. Repts.,* 167: College Station, TX (Ocean Drilling Program). **doi:10.2973/odp.proc.ir.167.1997**

Maiya, S., 1978. Late Cenozoic planktonic foraminiferal biostratigraphy of the oil-field region of northeast Japan. In *Cenozoic Geology of Japan:* Osaka, 35–60. (in Japanese, with abstract in English)

Maiya, S., Saito, T., and Sato, T., 1976. Late Cenozoic planktonic foraminiferal biostratigraphy of Northwest Pacific sedimentary sequences. *In* Takayanagi, Y., and Saito, T. (Eds.), *Progress in Micropaleontology:* New York (Micropaleontology Press), 395–422.

Manheim, F.T., and Sayles, F.L., 1974. Composition and origin of interstitial waters of marine sediments, based on deep sea drill cores. *In* Goldberg, E.D. (Ed.), *The Sea* (Vol. 5): *Marine Chemistry: The Sedimentary Cycle:* New York (Wiley), 527–568.

Martini, E., 1971. Standard Tertiary and Quaternary calcareous nannoplankton zonation. *In* Farinacci, A. (Ed.), *Proc. Second Planktonic Conf. Roma 1970:* Rome (Ed. Tecnosci.), 2:739–785.

Masuzawa, T., and Kitano, Y., 1983. Sulfate reduction and sulfide deposition in deep-sea sediments from the southwestern Japan Sea. *J. Oceanogr. Soc. Jpn.,* 39(5):251–258. **doi:10.1007/BF02070395**

Matsumoto, R., 1992. Diagenetic dolomite, calcite, rhodochrosite, magnesite, and lansfordite from Site 799, Japan Sea—implications for depositional environments and the diagenesis of organic-rich sediments. *In* Pisciotto, K.A., Ingle, J.C., Jr., von Breymann, M.T., Barron, J., et al., *Proc. ODP, Sci. Results,* 127/128 (Pt. 1): College Station, TX (Ocean Drilling Program), 75–98. **doi:10.2973/odp.proc.sr.127128-1.119.1992**

Matul, A., Abelmann, A., Tiedemann, R., Kaiser, A., and Nürnberg, D., 2002. Late Quaternary polycystine radiolarian datum events in the Sea of Okhotsk. *Geo-Mar. Lett.,* 22(1):25–32. **doi:10.1007/s00367-002-0093-y**

Mazzullo, J.M., Meyer, A., and Kidd, R.B., 1988. New sediment classification scheme for the Ocean Drilling Program. *In* Mazzullo, J., and Graham, A.G. (Eds.), *Handbook for shipboard sedimentologists*. ODP Tech. Note, 8:44–67. **doi:10.2973/odp.tn.8.1988**

McDuff, R.E., 1985. The chemistry of interstitial waters, Deep Sea Drilling Project Leg 86. *In* Heath, G.R., Burckle, L.H., et al., *Init. Repts. DSDP,* 86: Washington, DC (U.S. Govt. Printing Office), 675–687. **doi:10.2973/dsdp.proc.86.131.1985**

Miller, K.G., and Katz, M.E., 1987. Oligocene to Miocene benthic foraminiferal and abyssal circulation changes in the North Atlantic. *Micropaleontology,* 33(2):97–149. **doi:10.2307/1485489**

Millero, F.J., Feistel, R., Wright, D.G., and McDougall, T.J., 2008. The composition of Standard Seawater and the definition of the reference-composition salinity scale. *Deep-Sea Res., Part I,* 55(1):50–72. **doi:10.1016/j.dsr.2007.10.001**

Miwa, M., 2014. Foraminifera. In *Sekiyu Kogyo Binran (Petroleum Technology Handbook) 2013:* Tokyo (Jpn. Assoc. Pet. Technol.), 223–227. (in Japanese)

Mix, A.C., Le, J., and Shackleton, N.J., 1995. Benthic foraminiferal stable isotope stratigraphy of Site 846: 0–1.8 Ma. *In* Pisias, N.G., Mayer, L.A., Janecek, T.R., Palmer-Julson, A., and van Andel, T.H. (Eds.), *Proc. ODP, Sci. Results,* 138: College Station, TX (Ocean Drilling Program), 839–854. **doi:10.2973/odp.proc.sr.138.160.1995**

Mix, A.C., Tiedemann, R., Blum, P., et al., 2003. *Proc. ODP, Init. Repts.,* 202: College Station, TX (Ocean Drilling Program). **doi:10.2973/odp.proc.ir.202.2003**

Mohan, K., Gupta, A.K., and Bhaumik, A.K., 2011. Distribution of deep-sea benthic foraminifera in the Neogene of Blake Ridge, NW Atlantic Ocean. *J. Micropalaeontol.,* 30(1):33–74. **doi:10.1144/0262-821X10-008**

Morley, J.J., and Nigrini, C., 1995. Miocene to Pleistocene radiolarian biostratigraphy of North Pacific Sites 881, 884, 885, 886, and 887. *In* Rea, D.K., Basov, I.A., Scholl, D.W., and Allan, J.F. (Eds.), *Proc. ODP, Sci. Results,* 145:

College Station, TX (Ocean Drilling Program), 55–91. doi:10.2973/odp.proc.sr.145.107.1995

Motoyama, I., 1996. Late Neogene radiolarian biostratigraphy in the subarctic Northwest Pacific. *Micropaleontology,* 42(3):221–262. doi:10.2307/1485874

Motoyama, I., 2014. Radiolaria. In *Sekiyu Kogyo Binran (Petroleum Technology Handbook) 2013:* Tokyo (Jpn. Assoc. Pet. Technol.), 229–231. (in Japanese)

Motoyama, I., Niitsuma, N., Maruyama, T., Hayashi, H., Kamikuri, S., Shiono, M., Kanamatsu, T., Aoki, K., Morishita, C., Hagino, K., Nishi, H., and Oda, M., 2004. Middle Miocene to Pleistocene magneto-biostratigraphy of ODP Sites 1150 and 1151, northwest Pacific: sedimentation rate and updated regional geological timescale. *Isl. Arc,* 13(1):289–305. doi:10.1111/j.1440-1738.2003.00426.x

Munsell Color Company, Inc., 2009. *Munsell Soil Color Chart*: Grand Rapids, MI (Munsell Color Co., Inc.).

Murray, R.W., Brumsack, H.J., von Breymann, M.T., Sturz, A.A., Dunbar, R.B., and Gieskes, J.M., 1992. Diagenetic reactions in deeply buried sediments of the Japan Sea: a synthesis of interstitial-water chemistry results from Legs 127 and 128. *In* Tamaki, K., Suyehiro, K., Allan, J., McWilliams, M., et al., *Proc. ODP, Sci. Results,* 127/128 (Pt. 2): College Station, TX (Ocean Drilling Program), 1261–1274. doi:10.2973/odp.proc.sr.127128-2.177.1992

Murray, R.W., Miller, D.J., and Kryc, K.A., 2000. Analysis of major and trace elements in rocks, sediments, and interstitial waters by inductively coupled plasma–atomic emission spectrometry (ICP-AES). *ODP Tech. Note,* 29. doi:10.2973/odp.tn.29.2000

Nigrini, C., and Sanfilippo, A., 2001. Cenozoic radiolarian stratigraphy for low and middle latitudes with descriptions of biomarkers and stratigraphically useful species. *ODP Tech. Note,* 27. doi:10.2973/odp.tn.27.2001

Nobes, D.C., Murray, R.W., Kuramoto, S., Pisciotto, K.A., and Holler, P., 1992. Impact of silica diagenesis on physical property variations. *In* Pisciotto, K.A., Ingle, J.C., Jr., von Breymann, M.T., Barron, J., et al., *Proc. ODP, Sci. Results,* 127/128 (Pt. 1): College Station, TX (Ocean Drilling Program), 3–31. doi:10.2973/odp.proc.sr.127128-1.111.1992

Nomura, R., 1995. Paleogene to Neogene deep-sea paleoceanography in the eastern Indian Ocean: benthic foraminifera from ODP Sites 747, 757 and 758. *Micropaleontology,* 41(3):251–290. doi:10.2307/1485862

Okada, H., and Bukry, D., 1980. Supplementary modification and introduction of code numbers to the low-latitude coccolith biostratigraphic zonation (Bukry, 1973; 1975). *Mar. Micropaleontol.,* 5:321–325. doi:10.1016/0377-8398(80)90016-X

Paull, C.K., Lorenson, T.D., Dickens, G., Borowski, W.S., Ussler, W., III, and Kvenvolden, K., 2000. Comparisons of in situ and core gas measurements in ODP Leg 164 bore holes. *Ann. New York Acad. Sci.,* 912:23–31. doi:10.1111/j.1749-6632.2000.tb06756.x

Pearson, P.N., 1995. Planktonic foraminifer biostratigraphy and the development of pelagic caps on guyots in the Marshall Islands group. *In* Haggerty, J.A., Premoli Silva, I., Rack, F., and McNutt, M.K. (Eds.), *Proc. ODP, Sci. Results,* 144: College Station, TX (Ocean Drilling Program), 21–59. doi:10.2973/odp.proc.sr.144.013.1995

Pearson, P.N., and Chaisson, W.P., 1997. Late Paleocene to middle Miocene planktonic foraminifer biostratigraphy of the Ceara Rise. *In* Shackleton, N.J., Curry, W.B., Richter, C., and Bralower, T.J. (Eds.), *Proc. ODP, Sci. Results,* 154: College Station, TX (Ocean Drilling Program), 33–68. doi:10.2973/odp.proc.sr.154.106.1997

Pearson, P.N., Olsson, R.K., Huber, B.T., Hemleben, C., and Berggren, W.A. (Eds.), 2006. *Atlas of Eocene Planktonic Foraminifera*. Spec. Publ.—Cushman Found. Foraminiferal Res., 41.

Perch-Nielsen, K., 1985. Cenozoic calcareous nannofossils. *In* Bolli, H.M., Saunders, J.B., and Perch-Nielsen, K. (Eds.), *Plankton Stratigraphy:* Cambridge (Cambridge Univ. Press), 427–554.

Pezard, P., Lovell, M., and ODP Leg 126 Shipboard Scientific Party, 1990. Downhole images: electrical scanning reveals the nature of subsurface oceanic crust. *Eos, Trans. Am. Geophys. Union,* 71(20):709–718. doi:10.1029/90EO00178

Presley, B.J., 1971. Determination of minor and major inorganic constituents. *In* Winterer, E.L., Riedel, W.R., et al., *Init. Repts. DSDP,* 7: Washington, DC (U.S. Govt. Printing Office), 1749–1755. doi:10.2973/dsdp.proc.7.app1.1971

Pribnow, D., Kinoshita, M., and Stein, C., 2000. *Thermal Data Collection and Heat Flow Recalculations for Ocean Drilling Program Legs 101–180:* Hanover, Germany (Inst. Joint Geosci. Res., Inst. Geowiss. Gemeinschaftsauf. [GGA]). http://www-odp.tamu.edu/publications/heatflow/ODPReprt.pdf

Pujol, C., and Duprat, J., 1983. Quaternary planktonic foraminifers of the southwestern Atlantic (Rio Grande Rise) Deep Sea Drilling Project Leg 72. *In* Barker, P.F., Carlson, R.L., Johnson, D.A., et al., *Init. Repts. DSDP,* 72: Washington, DC (U.S. Govt. Printing Office), 601–615. doi:10.2973/dsdp.proc.72.128.1983

Rider, M.H., 1996. *The Geological Interpretation of Well Logs* (2nd ed.): Caithness (Whittles Publ.).

Ruddiman, W.F., Kidd, R.B., Thomas, E., et al., 1987. *Init. Repts. DSDP,* 94: Washington, DC (U.S. Govt. Printing Office). doi:10.2973/dsdp.proc.94.1987

Salimullah, A.R.M., and Stow, D.A.V., 1992. Application of FMS images in poorly recovered coring intervals: examples from ODP Leg 129. *In* Hurst, A., Griffiths, C.M., and Worthington, P.F. (Eds.), *Geological Application of Wireline Logs II.* Geol. Soc. Spec. Publ., 65(1):71–86. doi:10.1144/GSL.SP.1992.065.01.06

Sanfilippo, A., and Nigrini, C., 1998. Code numbers for Cenozoic low latitude radiolarian biostratigraphic zones and GPTS conversion tables. *Mar. Micropaleontol.,* 33(1–2):109–117, 121–156. doi:10.1016/S0377-8398(97)00030-3

Sayles, F.L., and Manheim, F., 1975. Interstitial solutions and diagenesis in deeply buried marine sediments: results from the Deep Sea Drilling Project. *Geochim. Cosmochim. Acta,* 39(2):103–127. doi:10.1016/0016-7037(75)90165-9

Schlumberger, 1989. *Log Interpretation Principles/Applications:* Houston (Schlumberger Educ. Serv.), SMP–7017.

Schlumberger, 1994. *IPL Integrated Porosity Lithology:* Houston (Schlumberger Wireline Testing), SMP-9270.

Schrader, H.J., and Gersonde, R., 1978. Diatoms and silicoflagellates. *In* Zachariasse, W.J., et al. (Eds.), *Micropaleontological Counting Methods and Techniques: An Exercise of an Eight Metres Section of the Lower Pliocene of Cap Rossello, Sicily.* Utrecht Micropaleontol. Bull., 17:129–176.

Schrag, D.P., Hampt, G., and Murray, D.W., 1996. Pore fluid constraints on the temperature and oxygen isotopic composition of the glacial ocean. *Science,* 272(5270):1930–1932. **doi:10.1126/science.272.5270.1930**

Schrum, H.N., Murray, R.W., and Gribsholt, B., 2012. Comparison of Rhizon sampling and whole round squeezing for marine sediment porewater. *Sci. Drill.,* 13:47–50. **doi:10.2204/iodp.sd.13.08.2011**

Serra, O., 1984. *Fundamentals of Well-Log Interpretation* (Vol. 1): *The Acquisition of Logging Data:* Amsterdam (Elsevier).

Serra, O., 1986. *Fundamentals of Well-Log Interpretation* (Vol. 2): *The Interpretation of Logging Data.* Amsterdam (Elsevier).

Serra, O., 1989. *Formation MicroScanner Image Interpretation:* Houston (Schlumberger Educ. Serv.), SMP-7028.

Shackleton, N.J., Baldauf, J.G., Flores, J.-A., Iwai, M., Moore, T.C., Jr., Raffi, I., and Vincent, E., 1995. Biostratigraphic summary for Leg 138. *In* Pisias, N.G., Mayer, L.A., Janecek, T.R., Palmer-Julson, A., and van Andel, T.H. (Eds.), *Proc. ODP, Sci. Results,* 138: College Station, TX (Ocean Drilling Program), 517–536. **doi:10.2973/odp.proc.sr.138.127.1995**

Shackleton, N.J., Crowhurst, S.J., Weedon, G.P., and Laskar, J., 1999. Astronomical calibration of Oligocene–Miocene time. *In* Shackleton N.J., McCave, I.N., and Graham, P.W. (Eds.), *Astronomical (Milankovitch) Calibration of the Geological Time-Scale.* Philos. Trans. R. Soc., A., 357(1757):1907–1929. **doi:10.1098/rsta.1999.0407**

Shepard, F.P., 1954. Nomenclature based on sand-silt-clay ratios. *J. Sediment. Res.,* 24(3):151–158. **doi:10.1306/D4269774-2B26-11D7-8648000102C1865D**

Shipboard Scientific Party, 1990. Site 796. *In* Tamaki, K., Pisciotto, K., Allan, J., et al., *Proc. ODP, Init. Repts.,* 127: College Station, TX (Ocean Drilling Program), 247–322. **doi:10.2973/odp.proc.ir.127.106.1990**

Shipboard Scientific Party, 1995. Explanatory notes. *In* Flood, R.D., Piper, D.J.W., Klaus, A., et al., *Proc. ODP, Init. Repts.,* 155: College Station, TX (Ocean Drilling Program), 47–81. **doi:10.2973/odp.proc.ir.155.104.1995**

Snyder, G.T, Hiruta, A., Matsumoto, R., Dickens, G.R., Tomaru, H., Takeuchi, R., Komatsubara, J., Ishida, Y., and Yu, H., 2007. Pore water profiles and authigenic mineralization in shallow marine sediments above the methane-charged system on Umitaka Spur, Japan Sea. *Deep-Sea Res., Part II,* 54(11–13):1216–1239. **doi:10.1016/j.dsr2.2007.04.001**

Solórzano, L., 1969. Determination of ammonia in natural waters by the phenol hypochlorite method. *Limnol. Oceanogr.,* 14(5):799–801. **doi:10.4319/lo.1969.14.5.0799**

Spezzaferri, S., 1994. Planktonic foraminiferal biostratigraphy and taxonomy of the Oligocene and lower Miocene in the oceanic record: an overview. *Palaeontographica Ital.,* 81.

Spezzaferri, S., and Premoli Silva, I., 1991. Oligocene planktonic foraminiferal biostratigraphy and paleoclimatic interpretation from Hole 538A, DSDP Leg 77, Gulf of Mexico. *Palaeogeogr., Palaeoclimatol., Palaeoecol.,* 83(1–3):217–263. **doi:10.1016/0031-0182(91)90080-B**

Stow, D.A.V., 2005. *Sedimentary Rocks in the Field: A Colour Guide:* London (Manson Publ.).

Strickland, J.D.H., and Parsons, T.R., 1968. *A Practical Handbook of Seawater Analysis.* Bull.—Fish. Res. Board Can., 167.

Sudo, H., 1986. A note on the Japan Sea Proper Water. *Prog. Oceanogr.,* 17(3–4):313–336. **doi:10.1016/0079-6611(86)90052-2**

Tada, R., and Iijima, A., 1992. Lithostratigraphy and compositional variation of Neogene hemipelagic sediments in the Japan Sea. *In* Tamaki, K., Suyehiro, K., Allan, J., McWilliams, M., et al., *Proc. ODP, Sci. Results,* 127/128 (Pt. 2): College Station, TX (Ocean Drilling Program), 1229–1260. **doi:10.2973/odp.proc.sr.127128-2.188.1992**

Tada, R., Koizumi, I., Cramp, A., and Rahman, A., 1992. Correlation of dark and light layers, and the origin of their cyclicity in the Quaternary sediments from the Japan Sea. *In* Pisciotto, K.A., Ingle, J.C., Jr., von Breymann, M.T., Barron, J., et al., *Proc. ODP, Sci. Results,* 127/128 (Pt. 1): College Station, TX (Ocean Drilling Program), 577–601. **doi:10.2973/odp.proc.sr.127128-1.160.1992**

Tada, R., Murray, R.W., Alvarez Zarikian, C.A., Anderson, W.T., Jr., Bassetti, M.-A., Brace, B.J., Clemens, S.C., da Costa Gurgel, M.H., Dickens, G.R., Dunlea, A.G., Gallagher, S.J., Giosan, L., Henderson, A.C.G., Holbourn, A.E., Ikehara, K., Irino, T., Itaki, T., Karasuda, A., Kinsley, C.W., Kubota, Y., Lee, G.S., Lee, K.E., Lofi, J., Lopes, C.I.C.D., Peterson, L.C., Saavedra-Pellitero, M., Sagawa, T., Singh, R.K., Sugisaki, S., Toucanne, S., Wan, S., Xuan, C., Zheng, H., and Ziegler, M., 2015a. Site U1422. *In* Tada, R., Murray, R.W., Alvarez Zarikian, C.A., and the Expedition 346 Scientists, *Proc. IODP,* 346: College Station, TX (Integrated Ocean Drilling Program). **doi:10.2204/iodp.proc.346.103.2015**

Tada, R., Murray, R.W., Alvarez Zarikian, C.A., Anderson, W.T., Jr, Bassetti, M.-A., Brace, B.J., Clemens, S.C., Dickens, G.R., Dunlea, A.G., Gallagher, S.J., Giosan, L., da Costa Gurgel, M.H., Henderson, A.C.G., Holbourn, A.E., Ikehara, K., Irino, T., Itaki, T., Karasuda, A., Kinsley, C.W., Kubota, Y., Lee, G.S., Lee, K.E., Lofi, J., Lopes, C.I.C.D., Peterson, L.C., Saavedra-Pellitero, M., Sagawa, T., Singh, R.K., Sugisaki, S., Toucanne, S., Wan, S., Xuan, C., Zheng, H., and Ziegler, M., 2015b. Site U1423. *In* Tada, R., Murray, R.W., Alvarez Zarikian, C.A., and the Expedition 346 Scientists, *Proc. IODP,* 346: College Station, TX (Integrated Ocean Drilling Program). **doi:10.2204/iodp.proc.346.104.2015**

Tada, R., Murray, R.W., Alvarez Zarikian, C.A., Anderson, W.T., Jr, Bassetti, M.-A., Brace, B.J., Clemens, S.C., Dickens, G.R., Dunlea, A.G., Gallagher, S.J., Giosan, L., da Costa Gurgel, M.H., Henderson, A.C.G., Holbourn, A.E., Ikehara, K., Irino, T., Itaki, T., Karasuda, A., Kinsley, C.W., Kubota, Y., Lee, G.S., Lee, K.E., Lofi, J., Lopes, C.I.C.D., Peterson, L.C., Saavedra-Pellitero, M., Sagawa, T., Singh, R.K., Sugisaki, S., Toucanne, S., Wan, S., Xuan, C., Zheng, H., and Ziegler, M., 2015c. Site U1427. *In* Tada, R., Murray, R.W., Alvarez Zarikian, C.A., and the Expedition 346 Scientists, *Proc. IODP,* 346: College Station, TX (Integrated Ocean Drilling Program). **doi:10.2204/iodp.proc.346.108.2015**

Takayanagi, T., Takayama, T., Sakai, T., Oda, M., and Kitazato, H., 1976. Microbiostratigraphy of some middle Miocene sequences in northern Japan. *In* Takayanagi, Y., and Saito, T. (Eds.), *Progress in Micropaleontology:Selected Papers in Honor of Prof. Kiyoshi Asano:* New York (Micropaleontol. Press), 356–381.

Tamaki, K., Pisciotto, K., Allan, J., et al., 1990. *Proc. ODP, Init. Repts.,* 127: College Station, TX (Ocean Drilling Program). **doi:10.2973/odp.proc.ir.127.1990**

Thomas, E., 1990. Late Cretaceous through Neogene deep-sea benthic foraminifers (Maud Rise, Weddell Sea, Antarctica). *In* Barker, P.F., Kennett, J.P., et al., *Proc. ODP, Sci. Results,* 113: College Station, TX (Ocean Drilling Program), 571–594. **doi:10.2973/odp.proc.sr.113.123.1990**

Thompson, P.R., Bé, A.W.H., Duplessy, J.-C., and Shackleton, N.J., 1979. Disappearance of pink-pigmented *Globigerinoides ruber* at 120,000 yr BP in the Indian and Pacific oceans. *Nature (London, U. K.),* 280(5723):554–558. **doi:10.1038/280554a0**

Tjalsma, R.C., and Lohmann, G.P., 1983. Paleocene–Eocene bathyal and abyssal benthic foraminifera from the Atlantic Ocean. *Micropaleontology, Spec. Publ.,* 4.

Toumarkine, M., and Luterbacher, H., 1985. Paleocene and Eocene planktic foraminifera. *In* Bolli, H.M., Saunders, J.B., and Perch-Nielsen, K. (Eds.), *Plankton Stratigraphy:* Cambridge (Cambridge Univ. Press), 87–154.

Turco, E., Bambini, A.M., Foresi, L., Iaccarino, S., Lirer, F., Mazzei, R., and Salvatorini, G., 2002. Middle Miocene high-resolution calcareous plankton biostratigraphy at Site 926 (Leg 154, equatorial Atlantic Ocean): palaeoecological and palaeobiogeographical implications. *Geobios,* 35(1):257–276. **doi:10.1016/S0016-6995(02)00064-5**

Usami, K., Ohi, T., Hasegawa, S., and Ikehara, K., 2013. Foraminiferal records of bottom-water oxygenation and surface-water productivity in the southern Japan Sea during 160–15 ka: associations with insolation changes. *Mar. Micropaleontol.,* 101:10–27. **doi:10.1016/j.marmicro.2013.03.006**

Van Marle, L.J., 1991. Eastern Indonesian late Cenozoic smaller benthic foraminifera. *Verh.—K. Ned. Akad. Wet., Afd. Natuurkd., Eerste Reeks,* 34.

van Morkhoven, F.P.C.M., Berggren, W.A., Edwards, A.S., and Oertli, H.J., 1986. Cenozoic cosmopolitan deep-water benthic foraminifera. *Bull. Cent. Rech. Explor.—Prod. Elf-Aquitaine,* 11.

Vasiliev, M.A., Blum, P., Chubarian, G., Olsen, R., Bennight, C., Cobine, T., Fackler, D., Hastedt, M., Houpt, D., Mateo, Z., and Vasilieva, Y.B., 2011. A new natural gamma radiation measurement system for marine sediment and rock analysis. *J. Appl. Geophys.,* 75:455–463. **doi:10.1016/j.jappgeo.2011.08.008**

Von Herzen, R., and Maxwell, A.E., 1959. The measurement of thermal conductivity of deep-sea sediments by a needle-probe method. *J. Geophys. Res.,* 64(10):1557–1563. **doi:10.1029/JZ064i010p01557**

Wade, B.S., Pearson, P.N., Berggren, W.A., and Pälike, H., 2011. Review and revision of Cenozoic tropical planktonic foraminiferal biostratigraphy and calibration to the geomagnetic polarity and astronomical time scale. *Earth-Sci. Rev.,* 104(1–3):111–142. **doi:10.1016/j.earscirev.2010.09.003**

Watanabe, M., and Yanagisawa, Y., 2005. Refined early to middle Miocene diatom biochronology for the middle- to high-latitude North Pacific. *Isl. Arc,* 14(2):91–101. **doi:10.1111/j.1440-1738.2005.00460.x**

Watkins, D.K., and Bergen, J.A., 2003. Late Albian adaptive radiation in the calcareous nannofossil genus *Eiffellithus*. *Micropaleontology,* 49(3):231–251. **doi:10.2113/49.3.231**

Wentworth, C.K., 1922. A scale of grade and class terms for clastic sediments. *J. Geol.,* 30(5):377–392. **doi:10.1086/622910**

Wilkens, R.H., Dickens, G.R., Tian, J., Backman, J., and the Expedition 320/321 Scientists, 2013. Data report: revised composite depth scales for Sites U1336, U1337, and U1338. *In* Pälike, H., Lyle, M., Nishi, H., Raffi, I., Gamage, K., Klaus, A., and the Expedition 320/321 Scientists, *Proc. IODP,* 320/321: Tokyo (Integrated Ocean Drilling Program Management International, Inc.). **doi:10.2204/iodp.proc.320321.209.2013**

Xuan, C., and Channell, J.E.T., 2009. UPmag: MATLAB software for viewing and processing U channel or other pass-through paleomagnetic data. *Geochem., Geophys., Geosyst.,* 10(10):Q10Y07. **doi:10.1029/2009GC002584**

Yanagisawa, Y., and Akiba, F., 1998. Refined Neogene diatom biostratigraphy for the northwest Pacific around Japan, with an introduction of code numbers for selected diatom biohorizons. *Chishitsugaku Zasshi,* 104(6):395–414. **doi:10.5575/geosoc.104.395**

You, C.-F., Gieskes, J.M., Chen, R.F., Spivack, A., and Gamo, T., 1993. Iodide, bromide, manganese, boron, and dissolved organic carbon in interstitial waters of the organic carbon–rich marine sediments: observations in the Nankai accretionary prism. *In* Hill, I.A., Taira, A., Firth, J.V., et al., *Proc. ODP, Sci. Results,* 131: College Station, TX (Ocean Drilling Program), 165–174. **doi:10.2973/odp.proc.sr.131.116.1993**

Publication: 28 March 2015
MS 346-102

Figure F1. Ternary plot showing classification scheme for sediments that are mixtures of pelagic biogenic and siliciclastic/volcaniclastic components, Expedition 346.

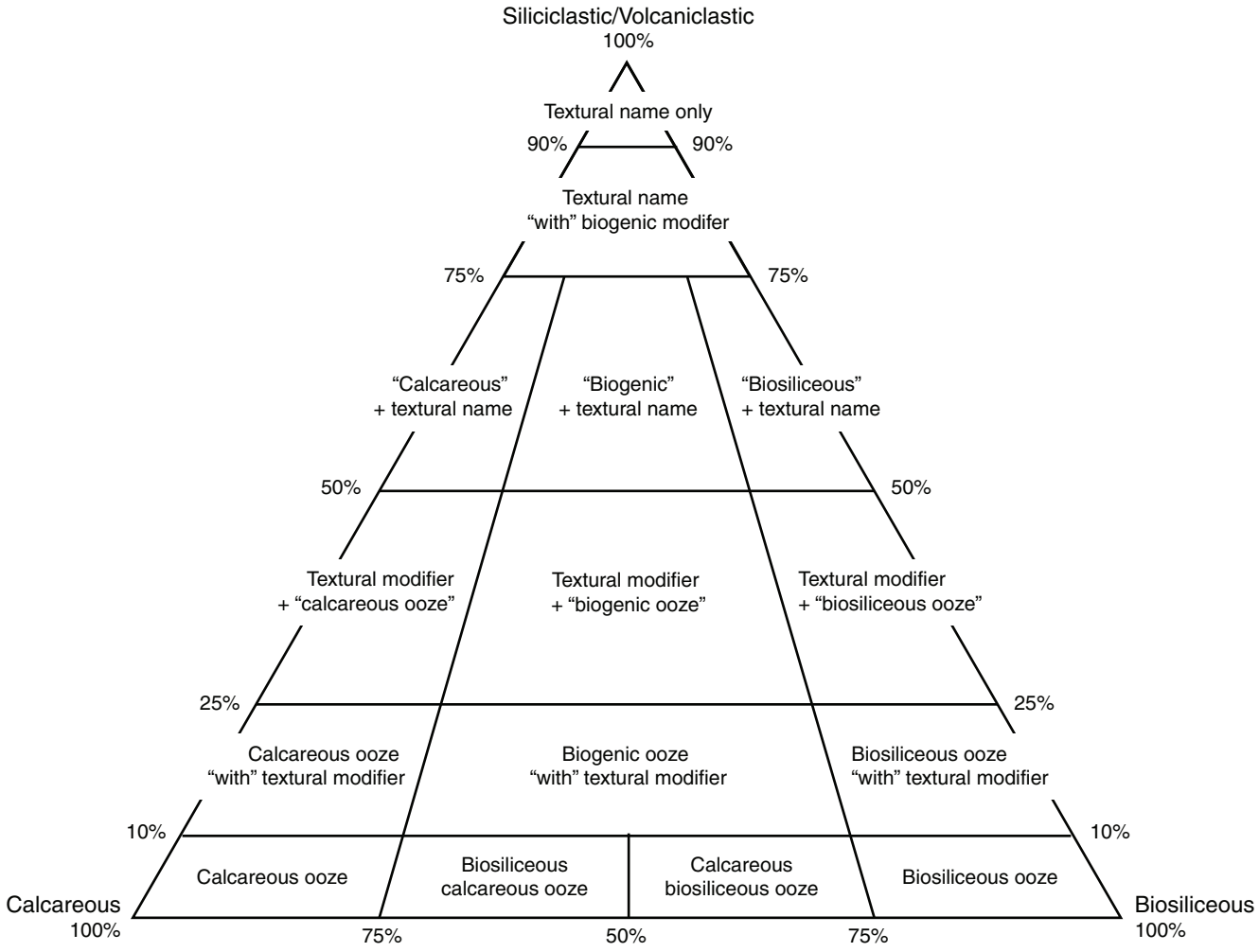

Figure F2. Ternary plot of lithology naming scheme for siliciclastic sediment/rock without gravel (modified from Shepard, 1954), Expedition 346.

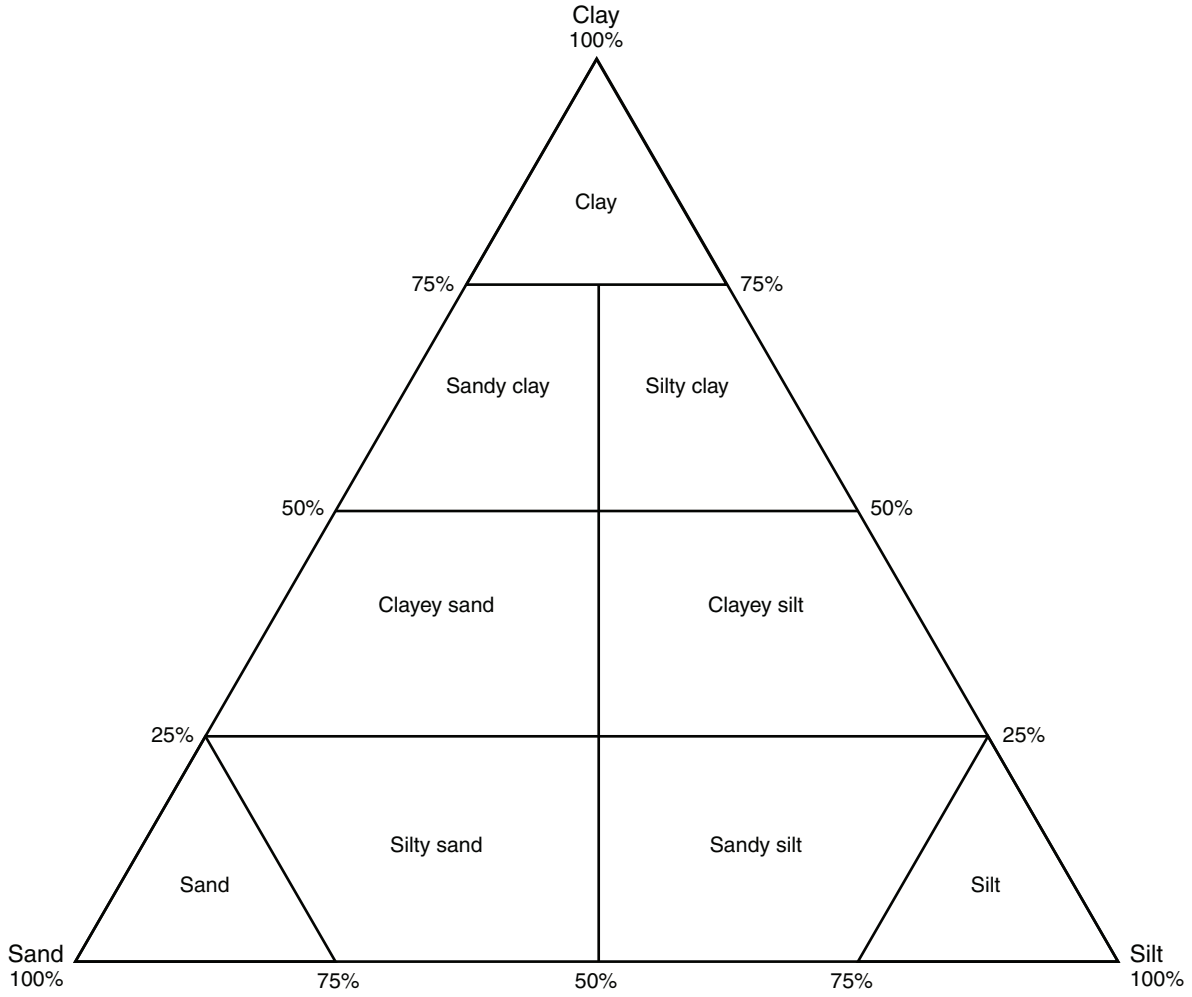

Figure F3. Classification scheme for sediments that are mixtures of volcanic grains and siliciclastic components, Expedition 346.

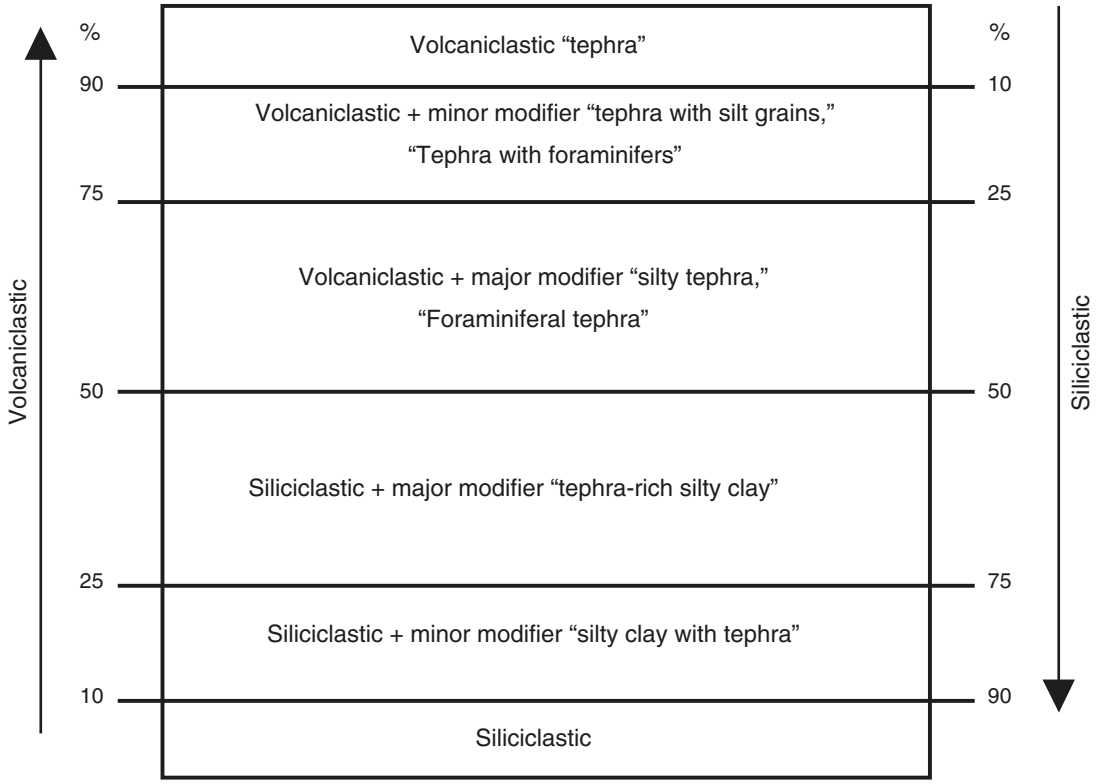

Figure F4. Graphic keys for lithology as used on visual core description sheets, Expedition 346.

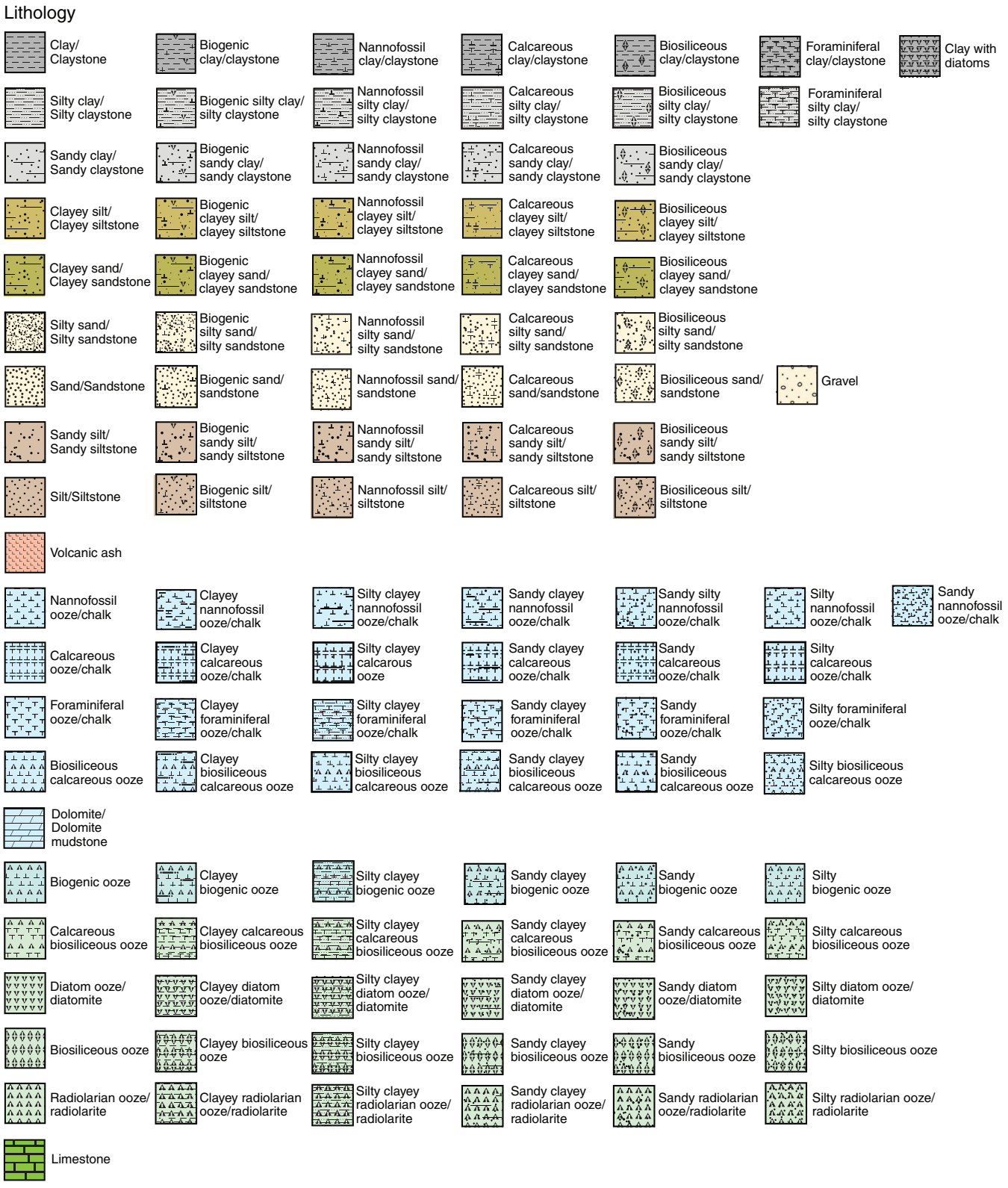

Figure F5. Example of a graphical visual core description (VCD) form generated for Expedition 346. GRA = gamma ray attenuation.

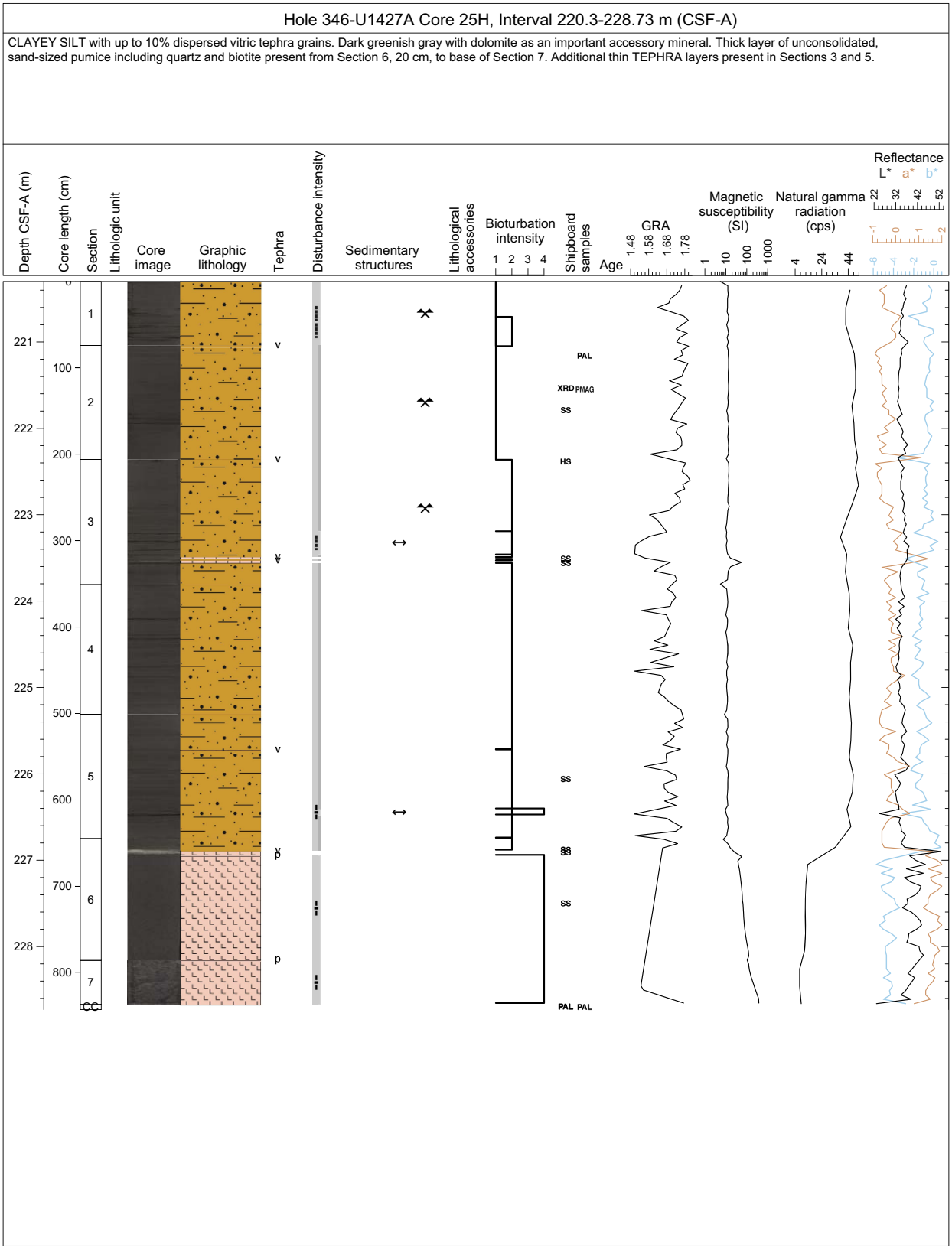

Figure F6. Legend used for visual core description forms including sedimentary structures, bioturbation index, lithologic accessories, drilling disturbance, and shipboard sample types, Expedition 346.

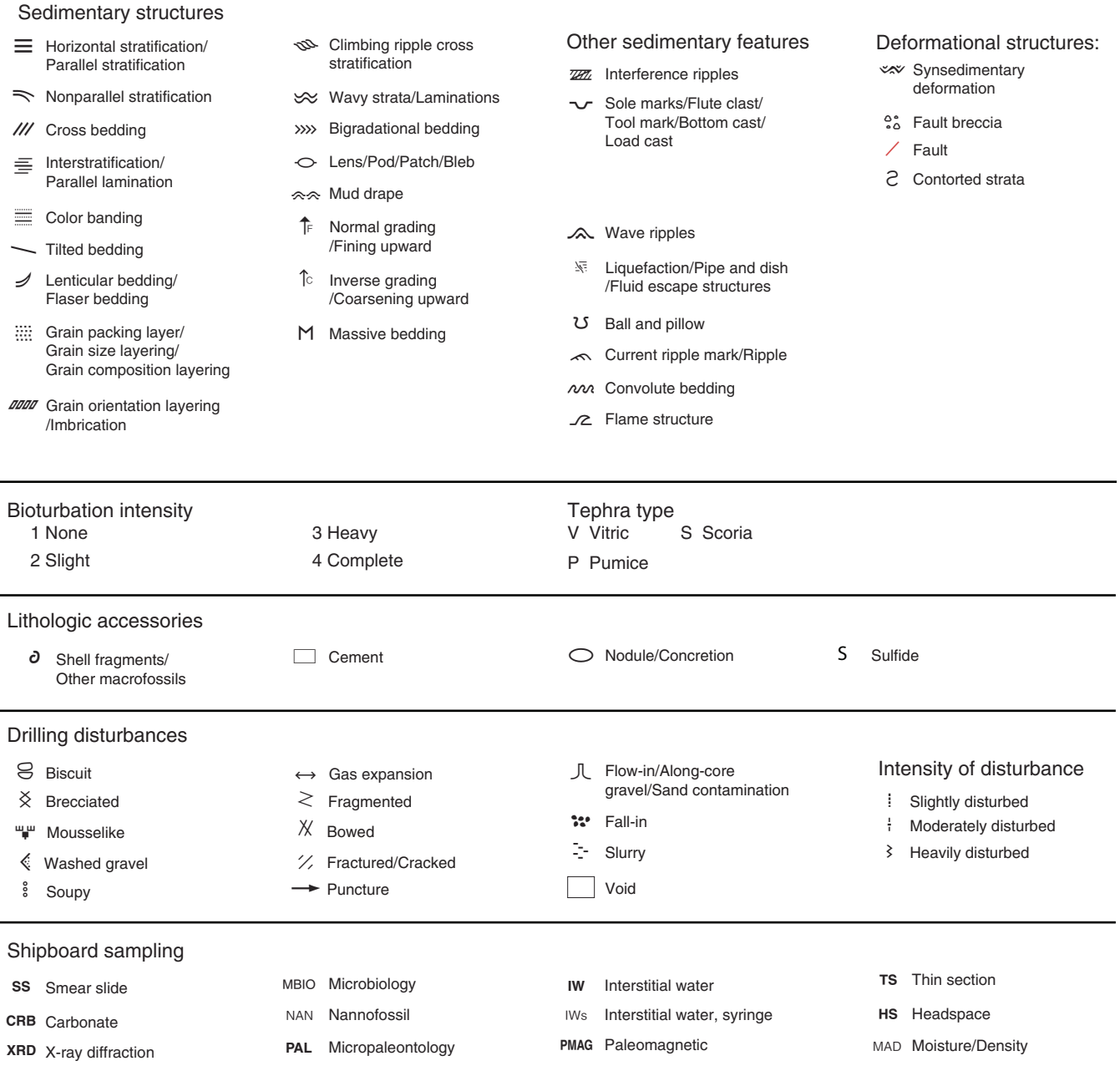

Figure F7. Smear slide description form, Expedition 346.

IODP Expedition 346 SMEAR SLIDE DESCRIPTION WORKSHEET

Leg	Site	Hole	Core	Section	Interval (cm) Top	Bottom

Observer	

Siliciclastic texture (%)		
Sand	Silt	Clay

Percent	Component
SILICICLASTIC GRAINS/MINERALS	
	Framework minerals
	Quartz
	Feldspar
	K-feldspar (Orthoclase, Microcline...)
	Plagioclase
	Rock fragments
	Sedimentary
	Igneous
	Metamorphic
	Accessory/trace minerals
	Micas
	Biotite
	Muscovite
	Chlorite
	Clay minerals
	Chert
	Heavy minerals
	Hornblende
	Augite
	Hypersthene
	Olivine
	Zircon
	Ferromagnesium minerals
	Authigenic minerals
	Barite
	Phosphorite/Apatite
	Zeolite
	Glauconite
	Opaque minerals
	Pyrite
	Magnetite
	Fe-oxide
	Carbonates
	Calcite
	Dolomite

Percent	Component
VOLCANICLASTIC GRAINS	
	Crystal grain
	Vitric grain (glass, pumice)
	Lithic grain
	Palagonite
BIOGENIC GRAINS	
	Calcareous
	Foraminifers
	Nannofossils
	Pteropods
	Sponge spicules
	Siliceous
	Radiolarians
	Diatoms
	Silicoflagellates
	Sponge spicules
	Dinoflagellates
	Others
	Pollen
	Organic debris
	Plant debris

Comments:

Fossil preservation	Abundance code
G = good	<1% = TR (trace)
M = moderate	1%-5% = R (rare)
P = poor	5%-25% = C (common)
	25%-75% = A (abundant)
	>75% = D (dominant)

Figure F8. Timescale used for Expedition 346 with calcareous nannofossil zones and datums through the interval 0–15 Ma. FCO = first common occurrence, LCO = last common occurrence. Bold = datums define zonal boundaries.

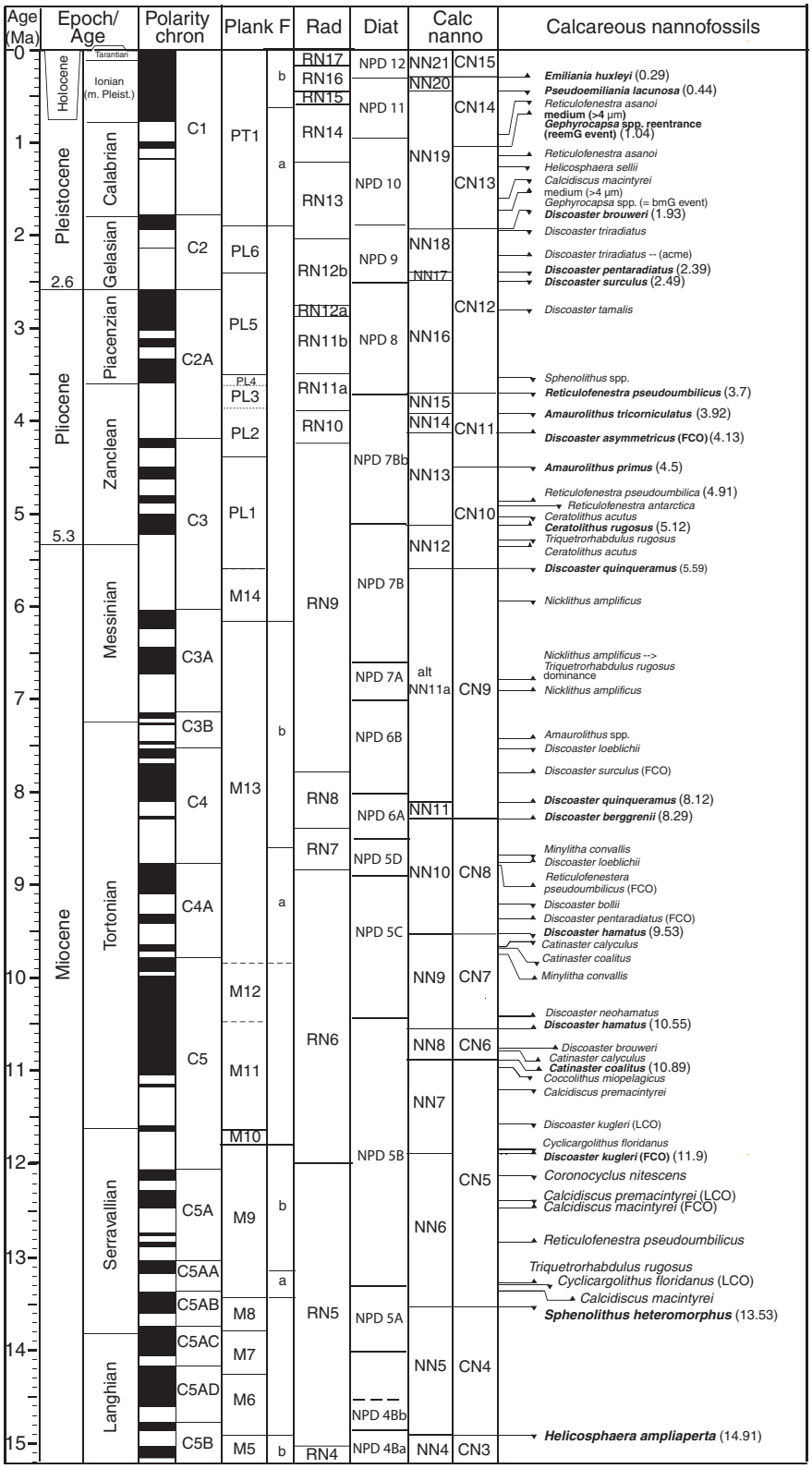

Figure F9. Timescale used for Expedition 346 with radiolarian zones and datums through the interval 0–15 Ma. Bold = datums define zonal boundaries. Two radiolarian zones of the mid- and low-latitude Pacific Ocean are mainly applied for the marginal sea west of Japan and the East China Sea, respectively. LCO = last common occurrence, RD = rapid decrease, RI = rapid increase, FCO = first common occurrence.

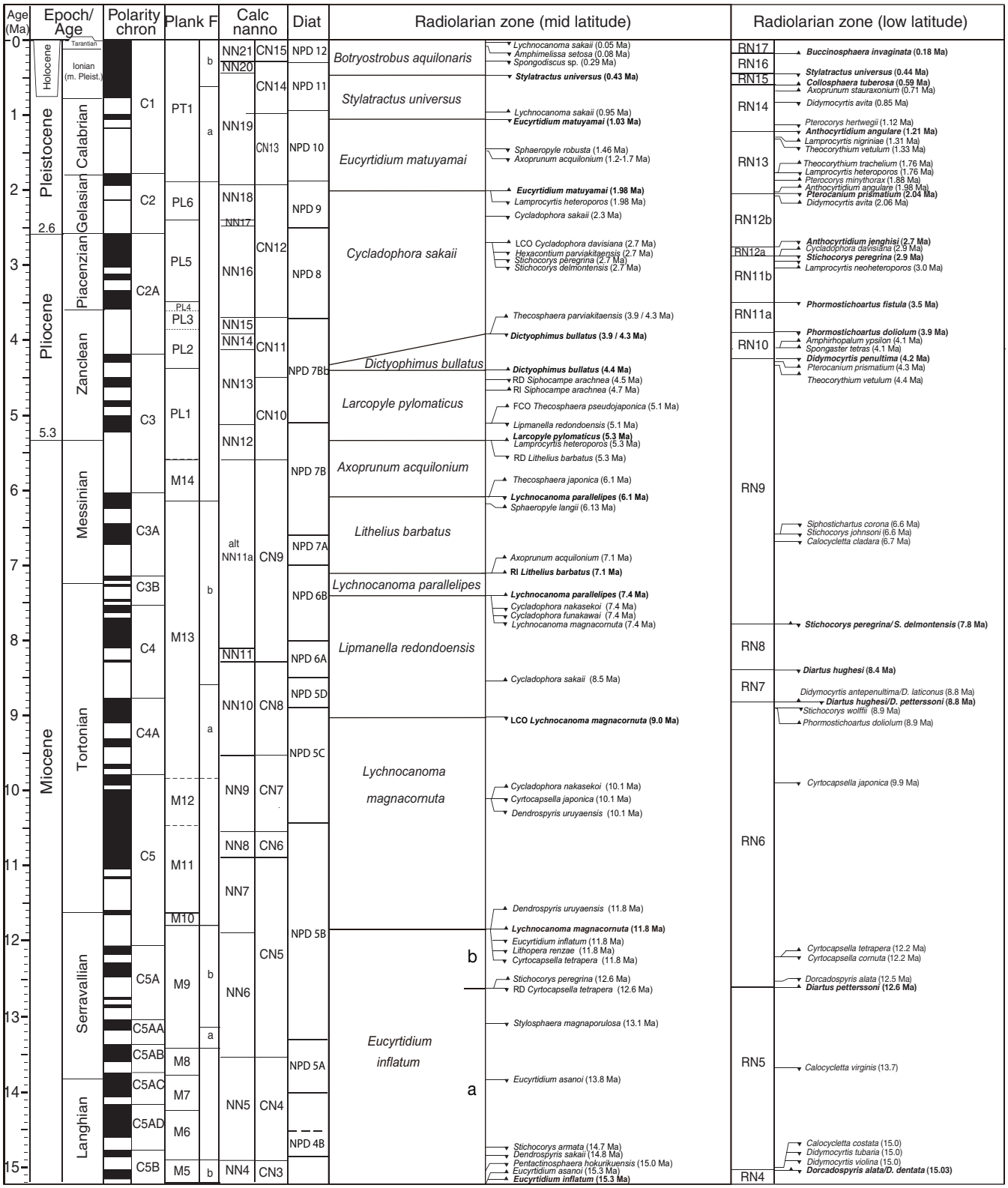

Figure F10. Timescale used for Expedition 346 with diatom zones and datums through the interval 0–15 Ma. LCO = last common occurrence, FCO = first common occurrence.

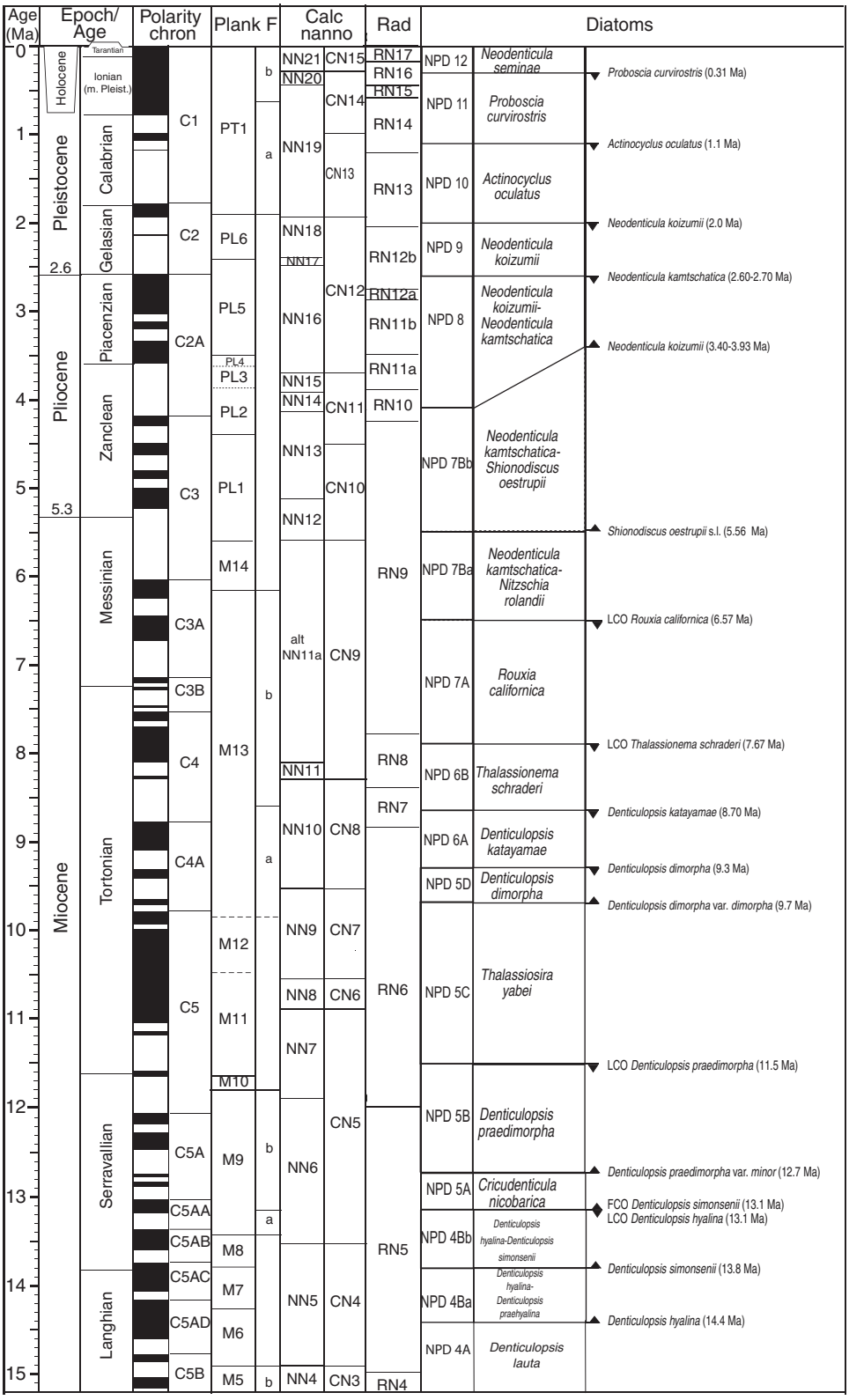

Figure F11. Timescale used for Expedition 346 with planktonic foraminiferal zones and datums through the interval 0–15 Ma. Gq. = *Globoquadrina*, Neo. = *Neogloboquadrina*, G. = *Globigerinoides*, Gr. = *Globorotalia*, Gt. = *Globoturborotalia*, Pull. = *Pulleniatina*, Dent. = *Dentoglobigerina*, HA = high abundance. Bold = datums define zonal boundaries.

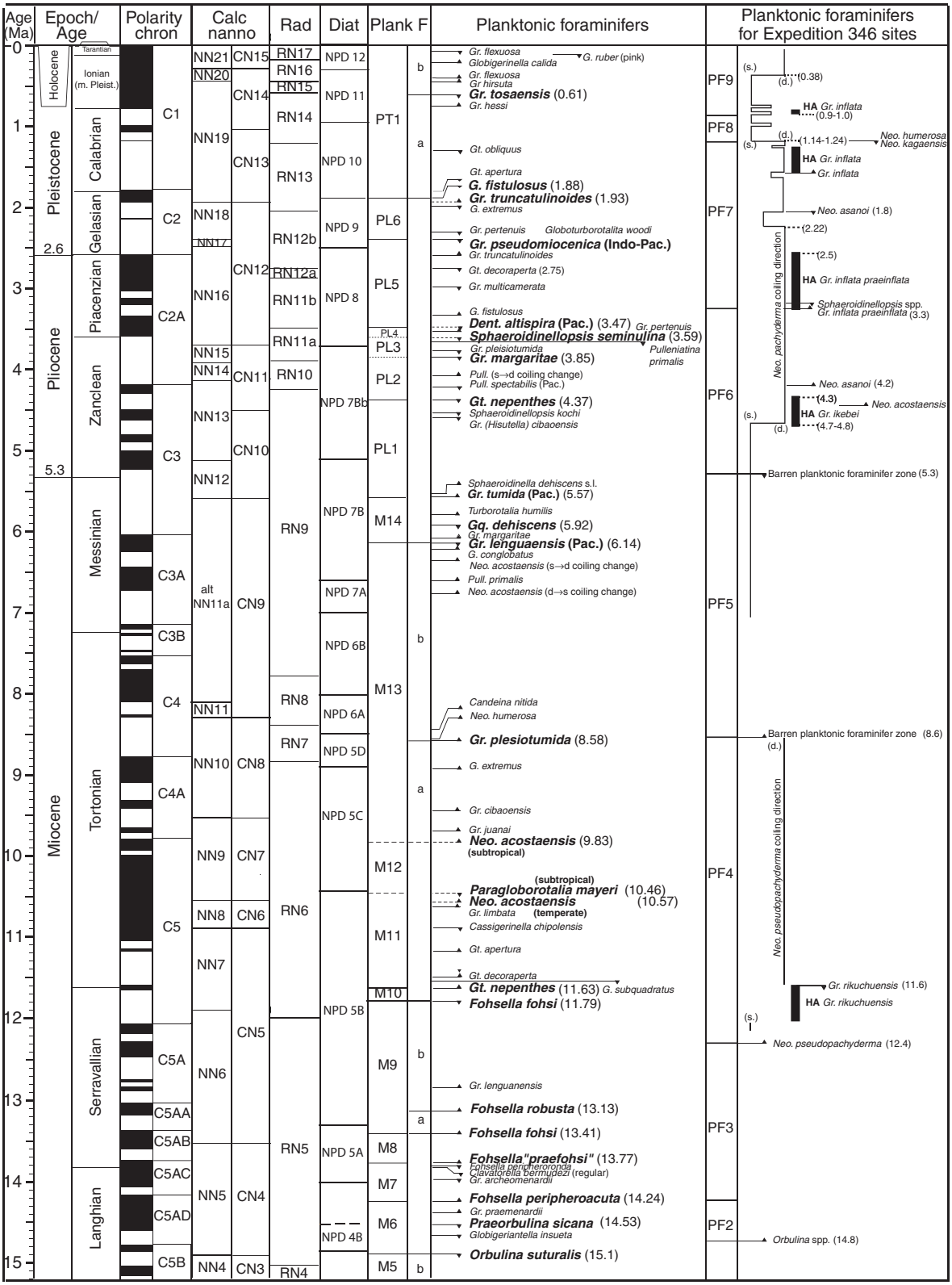

Figure F12. A. Diagram of coordinate systems used for the archive- and working-half core sections. **B.** Coordinate system used for superconducting rock magnetometer onboard the R/V *JOIDES Resolution*. **C.** Natsuhara-Giken sampling cubes (7 cm^3 volume) with sample coordinate system used during Expedition 346. **D.** Measurement positions, each name (e.g., top-toward) refer to the direction of the up arrow face (gray) with respect to user facing the magnetometer in the sample loading area and direction of the up arrow with respect to the magnetometer +*z*-axis.

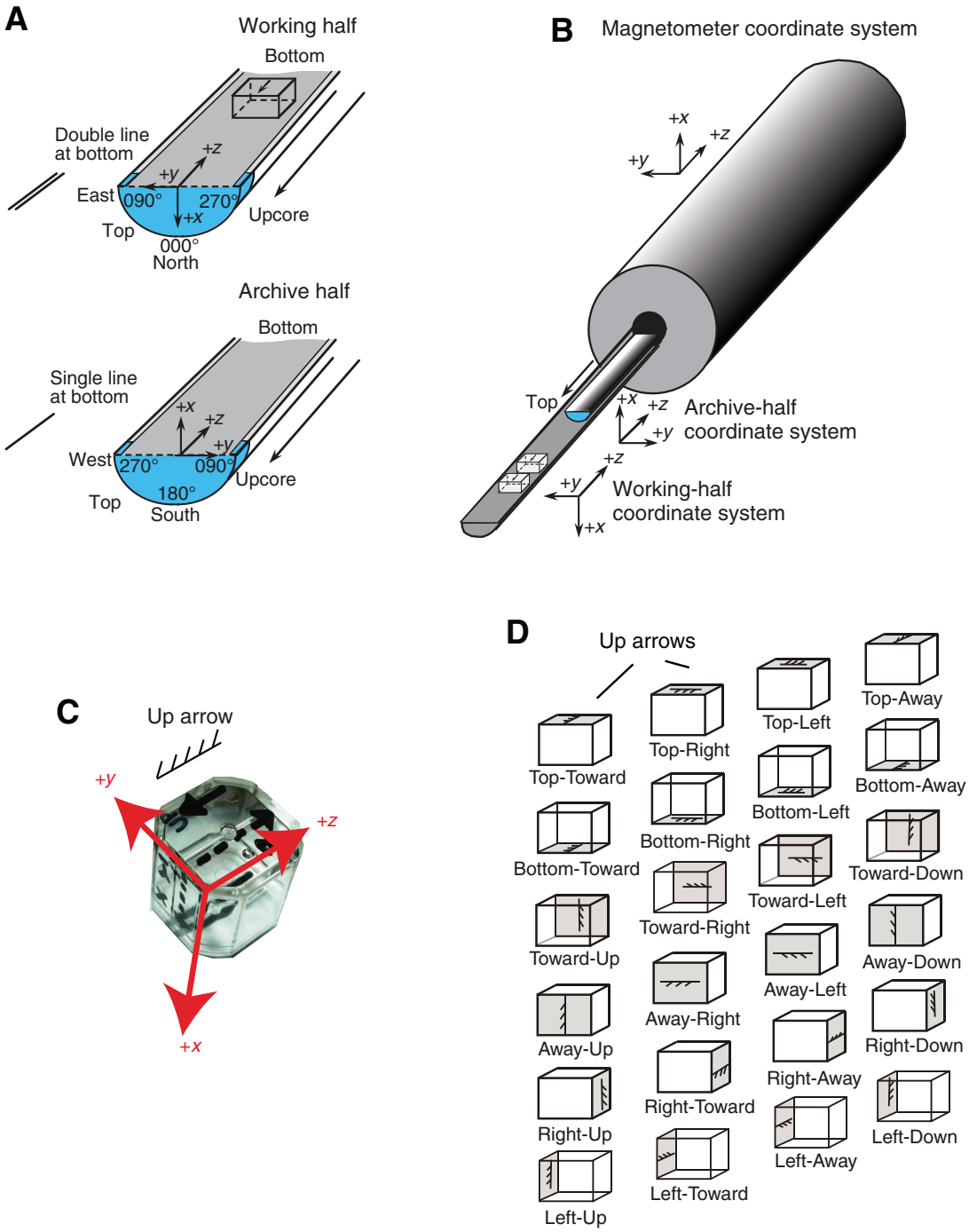

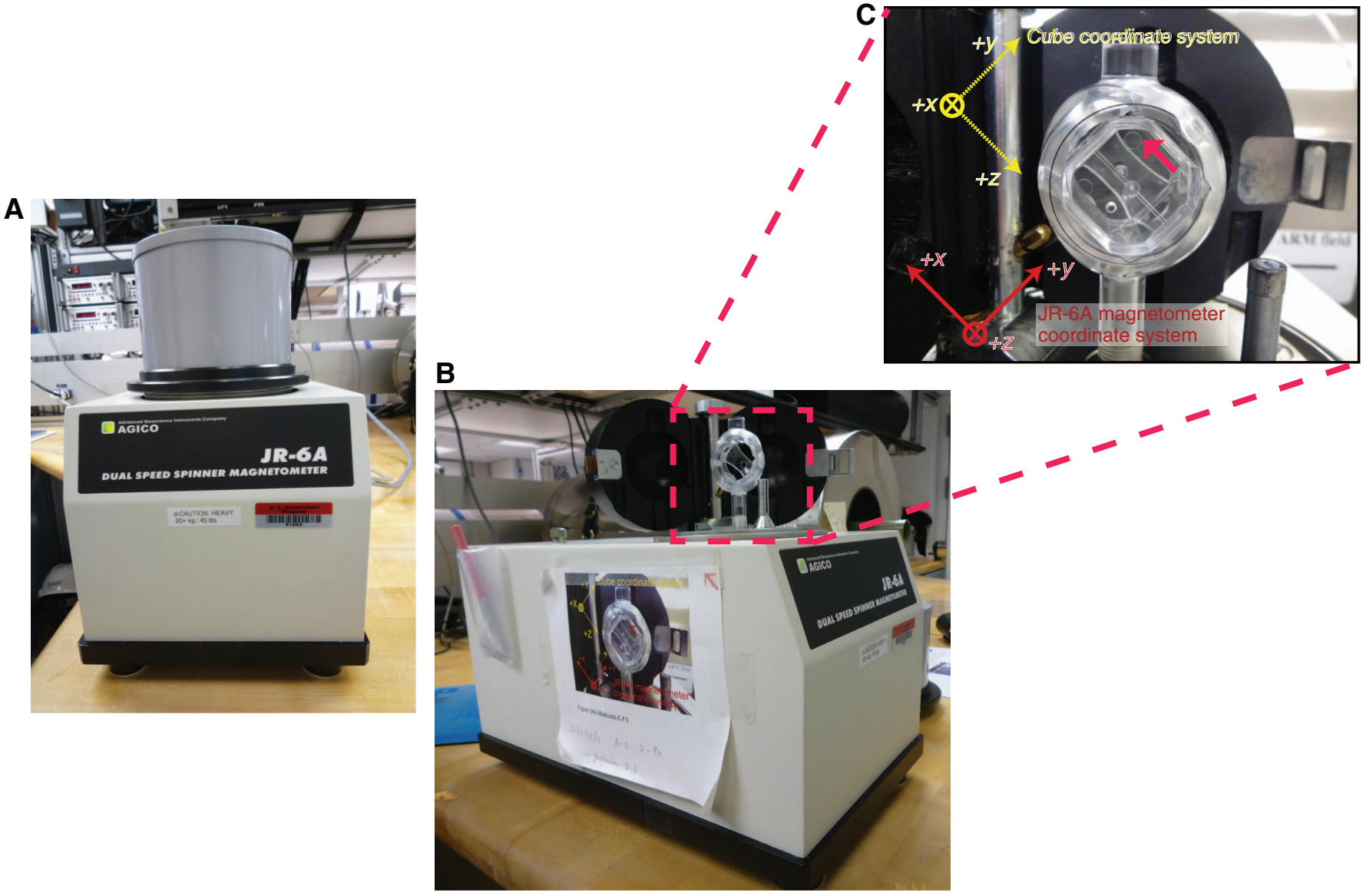

Figure F13. A. Photograph of JR-6A with the cover closed. **B.** Photograph of JR-6A with the cover opened. **C.** Photograph of the position of discrete samples in the "automatic holder" of the JR-6A magnetometer, Expedition 346. 56

Figure F14. Geomagnetic polarity timescale of Gradstein et al. (2012) used during Expedition 346.

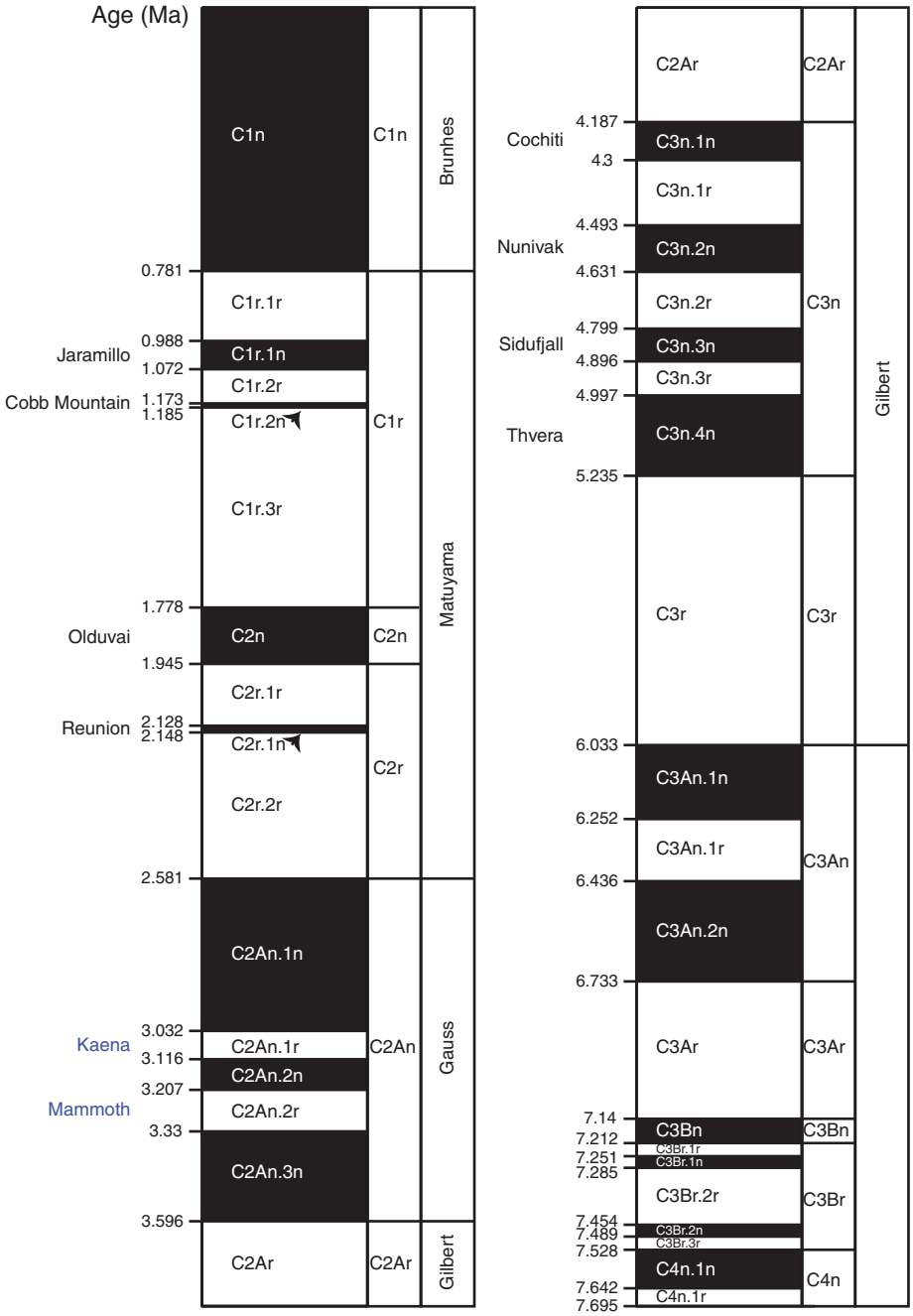

Figure F15. Wireline tool strings used during Expedition 346. For definitions of tool acronyms, see Table T13. LEH-QT = logging equipment head (model QT), EDTC = enhanced digital telemetry cartridge, HRLA = High-Resolution Laterolog Array, HNGS = Hostile Environment Natural Gamma Ray Sonde, HLDS = Hostile Environment Litho-Density Sonde, MSS = Magnetic Susceptibility Sonde, FMS = Formation MicroScanner, DSI = Dipole Shear Sonic Imager, GPIT = General Purpose Inclinometry Tool.

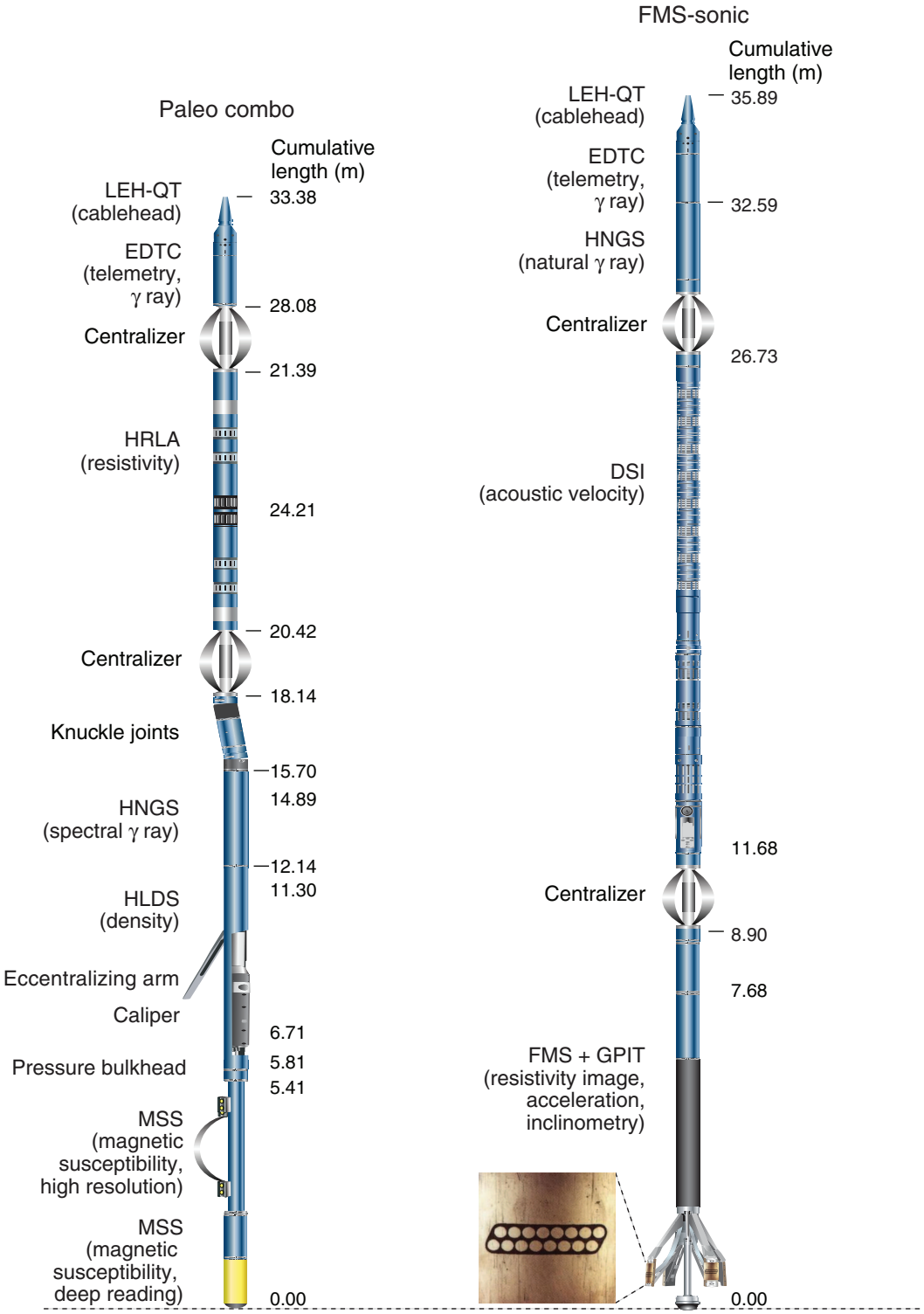

Figure F16. Interrelationship between cored material and the depth scales used in Expedition 346. Blue, brown, and purple intervals represent recovered core. Dashed and dotted lines represent equivalent horizons. Red dashed arrows represent tie points aligning specific, easily recognized features. The CSF-A scale is established by adding the curated core length to the core top DSF depth. Core expansion creates apparent overlaps and stratigraphic reversals when data are plotted on the CSF-A scale. The CCSF-A scale is constructed based on sequential identification of distinct horizons identified in multiple holes at a given site, working from the top of the section downward (red dashed arrows). The primary splice (CCSF-D) is constructed by combining selected intervals between tie points (purple) such that coring gaps and disturbed section are excluded, resulting in a complete stratigraphic section (less any natural, sedimentological hiatuses). CCSF-A depth designations are not necessarily equivalent to CCSF-D for intervals not included in the splice as illustrated by blue dashed lines. The "-A" and "-D" designations differentiate different methods of depth scale construction.

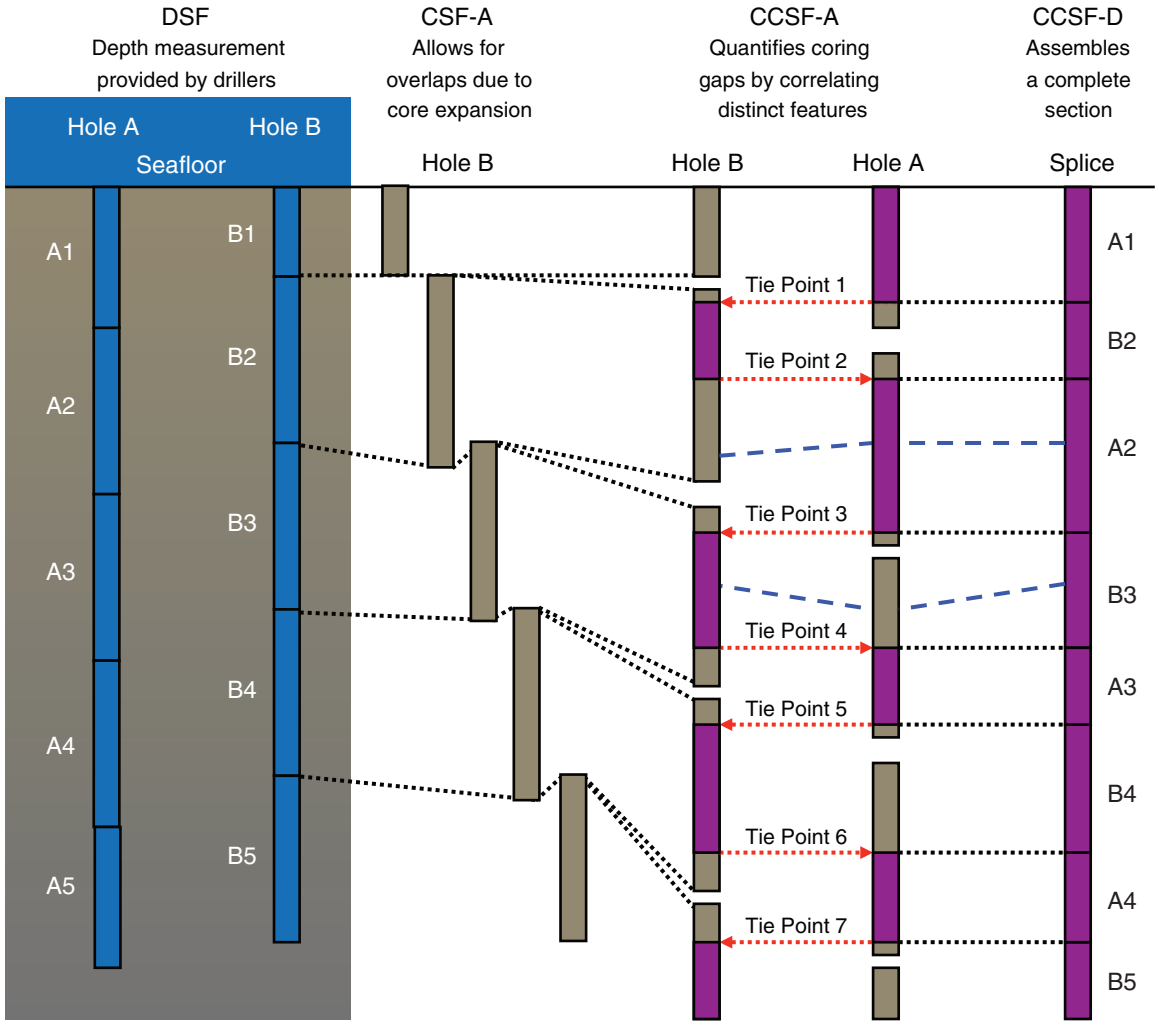

Table T1. Age estimates of calcareous nannofossil datum events considered for Expedition 346.

Event and species	Age (Ma)	Zone/Subzone (base)	Reference
FO *Emiliania huxleyi*	**0.29**	**NN21, CN15**	Gradstein et al., 2012
LO *Pseudoemiliania lacunosa*	**0.44**	**NN20, CN14b**	Gradstein et al., 2012
LO *Reticulofenestra asanoi*	0.91		Gradstein et al., 2012
Br *Gephyrocapsa* (>4 µm)	1.04		Gradstein et al., 2012
FCO *Reticulofenestra asanoi*	1.14		Lourens et al., 2004
LO *Gephyrocapsa* (>5.5 µm)	1.24		Gradstein et al., 2012
LO *Helicosphaera sellii*	1.34		Lourens et al., 2004
LO *Calcidiscus macintyrei*	1.60		Gradstein et al., 2012
FO *Gephyrocapsa* (>5.5 µm)	1.62		Gradstein et al., 2012
FO *Gephyrocapsa* (>4 µm)	1.73		Gradstein et al., 2012
LO *Discoaster brouweri*	**1.93**	**NN19, CN13a**	Gradstein et al., 2012
LO *Discoaster triradiatus*	1.95		Gradstein et al., 2012
FCO *Discoaster triradiatus*	2.14		Lourens et al., 2004
LO *Discoaster pentaradiatus*	**2.39**	**NN18**	Gradstein et al., 2012
LO *Discoaster surculus*	**2.49**	**NN17**	Gradstein et al., 2012
Pliocene/Pleistocene boundary	2.59		Gradstein et al., 2012
LO *Discoaster tamalis*	2.80		Gradstein et al., 2012
LO *Sphenolithus* spp.	3.54		Gradstein et al., 2012
LO *Reticulofenestra pseudoumbilica*	**3.70**	**NN16, CN12**	Gradstein et al., 2012
LO *Amaurolithus tricorniculatus*	**3.92**	**NN15**	Gradstein et al., 2012
FCO *Discoaster asymmetricus*	**4.13**	**NN14**	Gradstein et al., 2012
LO *Amaurolithus primus*	**4.50**	**CN11**	Gradstein et al., 2012
LO *Ceratolithus acutus*	5.04		Gradstein et al., 2012
FO *Ceratolithus rugosus*	**5.12**	**NN13**	Gradstein et al., 2012
LO *Triquetrorhabdulus rugosus*	5.28		Gradstein et al., 2012
Miocene/Pliocene boundary	5.33		Gradstein et al., 2012
FO *Ceratolithus acutus*	5.35		Gradstein et al., 2012
LO *Discoaster quinqueramus*	**5.59**	**NN12, CN10**	Gradstein et al., 2012
LCO *Nicklithus amplificus*	5.94		Gradstein et al., 2012
X *Nicklithus amplificus/T. rugosus*	6.79		Gradstein et al., 2012
FO *Nicklithus amplificus*	6.91		Gradstein et al., 2012
FO *Amaurolithus* spp.	7.42		Gradstein et al., 2012
LO *Discoaster loeblechii*	7.53		Gradstein et al., 2012
FO *Discoaster quinqueramus*	8.12		Gradstein et al., 2012
FO *Discoaster berggrenii*	**8.29**	**NN11, CN9**	Gradstein et al., 2012
LO *Discoaster bollii*	9.21		Gradstein et al., 2012
LO *Catinaster calyculus*	9.67		Gradstein et al., 2012
LO *Discoaster hamatus*	**9.69**	**NN10, CN8**	Lourens et al., 2004
LO *Catinaster coalitus*	9.69		Gradstein et al., 2012
FO *Discoaster hamatus*	**10.55**	**NN9, CN7**	Gradstein et al., 2012
FO *Catinaster calyculus*	10.79		Gradstein et al., 2012
FO *Catinaster coalitus*	**10.89**	**NN8, CN6**	Gradstein et al., 2012
LO *Coccolithus miopelagicus*	10.97		Gradstein et al., 2012
LCO *Discoaster kugleri*	11.58		Gradstein et al., 2012
FCO *Discoaster kugleri*	**11.90**	**NN7**	Gradstein et al., 2012
LO *Coronocyclus nitescens*	12.12		Gradstein et al., 2012
LO *Calcidiscus premacintyrei*	12.38		Gradstein et al., 2012
LCO *Cyclicargolithus floridanus*	13.28		Gradstein et al., 2012
LO *Sphenolithus heteromorphus*	**13.53**	**NN6, CN5**	Gradstein et al., 2012
LO *Helicosphaera ampliaperta*	**14.91**	**NN5, CN4**	Gradstein et al., 2012

FO = first occurrence, LO = last occurrence, FCO = first common occurrence, LCO = last common occurrence, Br = base reentrance, X = abundance crossover. Bold = zonal markers.

Table T2. Age estimates of radiolarian datum events for the East China Sea considered for Expedition 346.

Event and species	GTS2012 converted age (Ma)	Zone (base)	Reference
FO *Buccinosphaera invaginata* Haeckel	0.18	RN17	Expedition 342 Scientists, 2012
LO *Stylatractus universus* Hays	0.44	RN16	Expedition 342 Scientists, 2012
FO *Collosphaera tuberosa* Haeckel	0.59	RN15	Expedition 342 Scientists, 2012
FO *Axoprunum stauraxonium* Haeckel	0.71		Kamikuri et al., 2009
LO *Didymocyrtis avita* (Riedel)	0.85		Kamikuri et al., 2009
FO *Pterocorys hertwigii* (Haeckel)	1.12		Kamikuri et al., 2009
LO *Anthocyrtidium angulare* Nigrini	1.21	RN14	Expedition 342 Scientists, 2012
FO *Lamprocyrtis nigrininae* (Caulet)	1.31		Expedition 320/321 Scientists, 2010a
LO *Theocorythium vetulum* Nigrini	1.33		Expedition 320/321 Scientists, 2010a
LO *Lamprocyrtis heteroporos* (Hays)	1.76		Expedition 320/321 Scientists, 2010a
FO *Theocorythium trachelium trachelium* (Ehrenberg)	1.76		Expedition 320/321 Scientists, 2010a
FO *Pterocorys minythorax* (Nigrini)	1.88		Expedition 320/321 Scientists, 2010a
FO *Anthocyrtidium angulare* Nigrini	1.97		Expedition 320/321 Scientists, 2010a
LO *Pterocanium prismatium* Riedel	2.04	RN13	Expedition 342 Scientists, 2012
FO *Didymocyrtis avita* (Riedel)	2.06		Expedition 320/321 Scientists, 2010a
LO *Anthocyrtidium jenghisi* Streeter	2.74		Expedition 342 Scientists, 2012
FO *Cycladophora davisiana* Ehrenberg	2.89		Expedition 320/321 Scientists, 2010a
LO *Stichocorys peregrina* (Riedel)	2.87	RN12	Expedition 342 Scientists, 2012
FO *Lamprocyrtis neoheteroporos* Kling	3.03		Expedition 320/321 Scientists, 2010a
FO *Lamprocyrtis heteroporos* (Hays)	3.23		Expedition 320/321 Scientists, 2010a
LO *Phormostichoartus fistula* Nigrini	3.49		Expedition 342 Scientists, 2012
LO *Phormostichoartus doliolum* (Riedel and Sanfilippo)	3.89	RN11	Expedition 342 Scientists, 2012
FO *Amphirhopalum ypsilon* Haeckel	4.10		Expedition 320/321 Scientists, 2010a
LO *Didymocyrtis penultima* (Riedel)	4.24	RN10	Expedition 342 Scientists, 2012
FO *Spongaster tetras tetras* Ehrenberg	4.11		Expedition 320/321 Scientists, 2010a
FO *Pterocanium prismatium* Riedel	4.25		Kamikuri et al., 2009
FO *Liriospyris reticulata* Ehrenberg	4.43		Kamikuri et al., 2009
FO *Theocorythium vetulum* Nigrini	5.41		Kamikuri et al., 2009
LO *Siphostichartus corona* (Haeckel)	6.63		Kamikuri et al., 2009
LO *Stichocorys johnsoni* Caulet	6.63		Kamikuri et al., 2009
LO *Calocycletta cladara* Sanfilippo and Riedel	6.69		Kamikuri et al., 2009
ET *Stichocorys delmontensis* (Campbelland Clark)—*S. peregrina*	7.78	RN09	Expedition 342 Scientists, 2012
LCO *Diartus hughesi* (Campbell and Clark)	8.39	RN08	Expedition 342 Scientists, 2012
ET *Diartus petterssoni* (Riedel and Sanflippo)—*D. hughesi*	8.84	RN07	Expedition 342 Scientists, 2012
ET *Didymocyrtis laticonus* (Riedel)—*D. antepenultima* (Riedel and Sanfilippo)	8.84		Expedition 342 Scientists, 2012
LO *Stichocorys wolffii* Haeckel	8.87		Expedition 342 Scientists, 2012
FO *Phormostichoartus doliolum* (Riedel and Sanfilippo)	8.87		Expedition 342 Scientists, 2012
LO *Cyrtocapsella japonica* (Nakaseko)	9.86		Expedition 342 Scientists, 2012
LO *Cyrtocapsella cornuta* (Haeckel)	12.19		Expedition 342 Scientists, 2012
LO *Cyrtocapsella tetrapera* Haeckel	12.19		Expedition 342 Scientists, 2012
LO *Dorcadospyris alata* (Riedel)	12.5		Expedition 342 Scientists, 2012
FO *Diartus petterssoni* (Riedel and Sanflilippo)	12.6	RN06	Expedition 342 Scientists, 2012
LO *Calocycletta virginis* (Riedel and Sanfilippo)	13.67		Expedition 342 Scientists, 2012
LO *Calocycletta costata* (Riedel)	15		Expedition 342 Scientists, 2012
LO *Didymocyrtis tubaria* (Haeckel)	15		Expedition 342 Scientists, 2012
LO *Didymocyrtis violina* (Haeckel)	15		Expedition 342 Scientists, 2012
LO *Dorcadospyris forcipata* (Haeckel)	15.03		Expedition 342 Scientists, 2012
ET *Dorcadospyris dentata* Haeckel—*D. alata*	15.03	RN05	Expedition 342 Scientists, 2012

FO = first occurrence, LO = last occurrence, FCO = first common occurrence, LCO = last common occurrence, ET = evolutionary transition, RI = rapid increase, RD = rapid decrease.

Table T3. Age estimates of radiolarian datum events considered for Expedition 346.

Event and species	Age (Ma)	Zone (base)	Reference
LO *Lychnocanoma sakaii* (Morley and Nigrini)	0.05		Itaki et al., 2007
LO *Amphimelissa setosa* (Cleve)	0.08		Itaki et al., 2007
LO *Spongodiscus* sp. Kling (1973)	0.29		Matul et al., 2002
LO *Stylatractus universus* Hays	0.43	*B. aquilonaris*	Motoyama, 2014
LO *Eucyrtidium matuyamai* Hays	1.03	*S. universus*	Motoyama, 2014
FO *Eucyrtidium matuyamai* Hays	1.98	*E. matuyamai*	Motoyama, 2014
LO *Lamprocyrtis heteroporos* (Hays)	1.98		Kamikuri et al., 2004
LO *Axoprunum acquilonium* (Hays)	1.2–1.7		Alexandrovich, 1992
LO *Cycladophora sakaii* Motoyama	2.30		Kamikuri et al., 2004
FCO *Cycladophora davisiana* (Ehrenberg)	2.70		Motoyama, 2014
LO *Hexacontium parviakitaensis* Kamikuri	2.70		Motoyama, 2014
LO *Dictyophimus bullatus* Morley and Nigrini	3.9–4.3	*C. sakaii*	Motoyama, 2014
FO *Hexacontium parviakitaensis* Kamikuri	3.9–4.3		Motoyama, 2014
FO *Dictyophimus bullatus* Morley and Nigrini	4.40	*D. bullatus*	Motoyama, 2014
RD *Siphocampe arachnea* (Ehrenberg) group	4.46		Kamikuri et al., 2004
RI *Siphocampe arachnea* (Ehrenberg) group	4.71		Kamikuri et al., 2004
LO *Lipmanella redondoensis* (Campbell and Clark)	5.06		Kamikuri et al., 2004
FCO *Thecosphaera pseudojaponica* Nakaseko	5.11		Motoyama, 1996
FO *Larcopyle pylomaticus* (Riedel)	5.30	*L. pylomaticus*	Motoyama, 2014
RD *Lithelius barbatus* Motoyama	5.30		Motoyama, 2014
FO *Thecosphaera japonica* Nakaseko	6.10		Motoyama, 2014
LO *Lychnocanoma parallelipes* Motoyama	6.10	*A. acquilonium*	Motoyama, 2014
FO *Axoprunum acquilonium* (Hays)	7.00		Motoyama, 2014
RI *Lithelius barbatus* Motoyama	7.00	*L. barbatus*	Motoyama, 2014
LO *Cycladophora nakasekoi* Motoyama	7.40		Motoyama, 2014
LO *Cycladophora funakawai* Kamikuri	7.40		Kamikuri, 2010
LO *Lychnocanoma magnacornuta* Sakai	7.40		Motoyama, 2014
FO *Lychnocanoma parallelipes* Motoyama	7.40	*L. parallelipes*	Motoyama, 2014
FO *Cycladophora sakaii* Motoyama	8.45		Kamikuri et al., 2004
LC *Lychnocanoma magnacornuta* Sakai	9.00	*L. redondoensis*	Motoyama, 2014
FO *Cycladophora nakasekoi* Motoyama	10.10		Motoyama, 2014
LO *Cyrtocapsella japonica* Nakaseko	10.10		Motoyama, 2014
LO *Dendrospyris uruyaensis* Kamikuri	10.10		Motoyama, 2014
LO *Eucyrtidium inflatum* Kling	11.80		Motoyama, 2014
LO *Cyrtocapsella tetrapera* (Haeckel)	11.80		Motoyama, 2014
LO *Lithopera renzae* Sanfilippo and Riedel	11.80		Kamikuri et al., 2007
FO *Dendrospyris uruyaensis* Kamikuri	11.80		Motoyama, 2014
FO *Lychnocanoma magnacornuta* Sakai	11.80	*L. magnacornuta*	Motoyama, 2014
RD *Cyrtocapsella tetrapera* (Haeckel)	12.60		Motoyama, 2014
LO *Stylosphaera magnaporulosa* (Nakaseko)	13.10		Motoyama, 2014
LO *Eucyrtidium asanoi* Sakai	13.80		Motoyama, 2014
LO *Stichocorys armata* (Haeckel)	14.69		Kamikuri et al., 2004
LO *Dendrospyris sakaii* Sugiyama and Furutani	14.83		Kamikuri et al., 2004
LO *Pentactinosphaera hokurikuensis* (Nakaseko)	14.99		Kamikuri et al., 2004
FO *Eucyrtidium asanoi* Sakai	15.30		Motoyama, 2014
FO *Eucyrtidium inflatum* Kling	15.30	*E. inflatum*	Motoyama, 2014

FO = first occurrence, LO = last occurrence, FCO = first common occurrence, ET = evolutionary transition, RI = rapid increase, RD = rapid decrease.

Table T4. Age estimates of diatom datum events considered for Expedition 346.

Diatom and species	Age in Yanagisawa and Akiba (1998) (Ma)	Age converted Gradstein et al., 2012 (Ma)	Zone (base)	Reference
LO *Proboscia curvirostis*	**0.31**	**0.31**	**NPD 12**	Yanagisawa and Akiba, 1998
LO *Actinocyclus oculatus*	**1.10**	**1.10**	**NPD 11**	Yanagisawa and Akiba, 1998
LO *Neodenticula koizumii*	**2.00**	**2.00**	**NPD 10**	Yanagisawa and Akiba, 1998
FO *Neodenticula seminae*	2.40	2.40		
LO *Neodenticula kamtschatica*	**2.6–2.7**	**2.60–2.70**	**NPD 9**	Yanagisawa and Akiba, 1998
FO *Neodenticula koizumii*	**3.5–3.9**	**3.40–3.93**	**NPD 8**	
FO *Actinocyclus oculatus*	4.00	4.03		
LO *Thalassiosira jacksonii* (*plicate*)	4.80	4.81		Yanagisawa and Akiba, 1998
FO *Thalassiosira jacksonii* (*plicate*)	5.20	5.21		Yanagisawa and Akiba, 1998
LO *Thalassiosira temperei*	5.40	5.44		Yanagisawa and Akiba, 1998
FO *Shionodiscus oestrupii*	**5.50**	**5.56**	**NPD 7Bb**	Yanagisawa and Akiba, 1998
FO *Thalassiosira praeoestrupii*	6.10	6.22		Yanagisawa and Akiba, 1998
LCO *Rouxia californica*	**6.40**	**6.57**	**NPD 7Ba**	Yanagisawa and Akiba, 1998
FCO *Neodenticula kamtschatica*	6.40	6.57		Yanagisawa and Akiba, 1998
LCO *Thalassionema schraderi*	**7.60**	**7.67**	**NPD 7A**	Yanagisawa and Akiba, 1998
LO *Denticulopsis katayamae*	**8.50**	**8.70**	**NPD 6B**	Yanagisawa and Akiba, 1998
LO *Denticulopsis dimorpha*	**9.20**	**9.30**	**NPD 6A**	Yanagisawa and Akiba, 1998
FO *Denticulopsis dimorpha* v. *dimorpha*	**10.00**	**9.70**	**NPD 5D**	Yanagisawa and Akiba, 1998
LCO *Denticulopsis hustedii*	10.10	10.20		Yanagisawa and Akiba, 1998
LCO *Denticulopsis praedimorpha*	**11.50**	**11.50**	**NPD 5C**	Yanagisawa and Akiba, 1998
FO *Denticulopsis praedimorpha* v. *minor*	**12.90**	**12.70**	**NPD 5B**	Yanagisawa and Akiba, 1998
FCO *Denticulopsis simonsenii*	13.10	13.10		Yanagisawa and Akiba, 1998
LCO *Denticulopsis hyalina*	**13.10**	**13.10**	**NPD 5A**	Yanagisawa and Akiba, 1998
FO *Denticulopsis simonsenii*	**14.5–14.6**	**13.80**	**NPD 4Bb**	Yanagisawa and Akiba, 1998
FO *Denticulopsis hyalina*	**14.90**	**14.40**	**NPD 4Ba**	Yanagisawa and Akiba, 1998
FO *Denticulopsis lauta*	**15.90**	**15.90**	**NPD 4A**	Yanagisawa and Akiba, 1998

LO = last occurrence, FO = first occurrence, LCO = last common occurrence, FCO = first common occurrence. Bold = primary Neogene North Pacific diatom biohorizons, regular = secondary Neogene North Pacific diatom biohorizons used (see Yanagisawa and Akiba, 1998, for a complete list).

Table T5. Age estimates of planktonic foraminiferal datum events for the Pacific Ocean considered for Expedition 346. (Continued on next page.)

Event and species	Age (Ma)	Zone/Subzone (base)	Reference[†]
LO *Globorotalia flexuosa*	0.07	PT1b	Berggren et al., 1995a
LO* *Globigerinoides ruber* (pink)	0.12	PT1b	Thompson et al., 1979
FO *Globigerinella calida*	0.22	PT1b	Chapronière et al., 1994
FO *Globorotalia flexuosa*	0.40	PT1b	Berggren et al., 1995a
FO *Globorotalia hirsuta*	0.45	PT1b	Pujol and Duprat, 1983
LO *Globorotalia* (*Truncorotalia*) *tosaensis*	**0.61**	**PT1b/PT1a**	Mix et al., 1995
FO *Globorotalia hessi*	0.75	PT1a	Chapronière et al., 1994
X* *Pulleniatina* coiling change random to dextral	0.80	PT1a	Pearson, 1995
LO *Globoturborotalita obliquus*	1.30	PT1a	Chaisson and Pearson, 1997
LO *Globoturborotalita apertura*	1.64	PT1a	Chaisson and Pearson, 1997
LO *Globigerinoides fistulosus*	**1.88**	**PT1a/PL6**	Shackleton et al., 1990
LO *Globigerinoides extremus*	1.98	PL6	Chaisson and Pearson, 1997
LO *Globoturborotalita woodi*	2.30	PL6	Chaisson and Pearson, 1997
LO *Globorotalia pertenuis*	2.30	PL6	Chaisson and Pearson, 1997
LO* *Globorotalia pseudomiocenica*	**2.39**	**PL6/PL5**	Berggren et al., 1995a
Pliocene/Pleistocene boundary	2.59		Gradstein et al., 2012
LO *Globoturborotalita decoraperta*	2.75	PL5	Chaisson and Pearson, 1997
LO *Globorotalia* (*Menardella*) *multicamerata*	2.98	PL5	Chaisson and Pearson, 1997
FO *Globigerinoides fistulosus*	3.33	PL5	Berggren et al., 1995a
LO* *Dentoglobigerina altispira*	**3.47**	**PL5/PL4**	Chaisson and Pearson, 1997
FO *Globorotalia pertenuis*	3.52	PL4	Chaisson and Pearson, 1997
LO* *Sphaeroidinellopsis seminulina*	**3.59**	**PL4/PL3**	Chaisson and Pearson, 1997
LO *Pulleniatina primalis*	3.66	PL3	Berggren et al., 1995a
LO *Globorotalia plesiotumida*	3.77	PL3	Chaisson and Pearson, 1997
LO *Globorotalia* (*Hirsutella*) *margaritae*	**3.85**	**PL3/PL2**	Chaisson and Pearson, 1997
X *Pulleniatina* coiling change sinistral to dextral	4.08	PL2	Chaisson and Pearson, 1997
LO* *Pulleniatina spectabilis*	4.21	PL2	Berggren et al., 1995a
LO *Globoturborotalita nepenthes*	**4.37**	**PL2/PL1**	Chaisson and Pearson, 1997
LO *Sphaerodinellopsis kochi*	4.53	PL1	Chaisson and Pearson, 1997
LO *Globorotalia* (*Hirsutella*) *cibaoensis*	4.60	PL1	Berggren et al., 1995b
Miocene/Pliocene boundary	5.33		Gradstein et al., 2012
FO *Sphaeroidinella dehiscens* s.l.	5.53	PL1	Chaisson and Pearson, 1997
FO* *Globorotalia tumida*	**5.57**	**PL1/M14**	Shackleton et al., 1995
FO *Turborotalita humilis*	5.81	M14	Chaisson and Pearson, 1997
LO *Globoquadrina dehiscens*	5.92	M14	Chaisson and Pearson, 1997
FO *Globorotalia* (*Hirsutella*) *margaritae*	6.08	M14	Chaisson and Pearson, 1997
LO* *Globorotalia lenguaensis*	**6.14**	**M14/M13b**	Berggren et al., 1995b
FO *Globigerinoides conglobatus*	6.20	M13b	Chaisson and Pearson, 1997
X *Neogloboquadrina acostaensis* coiling change sinistral to dextral	6.37	M13b	Berggren et al., 1995b
FO *Pulleniatina primalis*	6.60	M13b	Berggren et al., 1995b
X *Neogloboquadrina acostaensis* coiling change dextral to sinistral	6.77	M13b	Berggren et al., 1995b
FO *Candeina nitida*	8.43	M13b	Berggren et al., 1995b
FO *Neogloboquadrina humerosa*	8.56	M13b	Berggren et al., 1995b
FO *Globorotalia plesiotumida*	**8.58**	**M13b/M13a**	Chaisson and Pearson, 1997
FO *Globigerinoides extremus*	8.93	M13a	Turco et al., 2002
FO *Globorotalia cibaoensis*	9.44	M13a	Chaisson and Pearson, 1997
FO *Globorotalia juanai*	9.69	M13a	Chaisson and Pearson, 1997
FO* *Neogloboquadrina acostaensis* [(sub)tropical]	**9.83**	**M13a/M12**	Chaisson and Pearson, 1997
LO* *Paragloborotalia mayeri* [(sub)tropical]	**10.46**	**M12/M11**	Chaisson and Pearson, 1997
FO* *Neogloboquadrina acostaensis* (temperate)	10.57	M11	Chaisson and Pearson, 1997
FO *Globorotalia limbata*	10.64	M11	Chaisson and Pearson, 1997
LO *Cassigerinella chipolensis*	10.89	M11	Turco et al., 2002
FO *Globoturborotalita apertura*	11.18	M11	Chaisson and Pearson, 1997
FO *Globoturborotalita decoraperta*	11.49	M11	Chaisson and Pearson, 1997
LO *Globigerinoides subquadratus*	11.54	M11	Turco et al., 2002
FO *Globoturborotalita nepenthes*	**11.63**	**M11/M10**	Turco et al., 2002
LO *Globorotalia* (*Fohsella*) *fohsi* s.l. (includes lobata and robusta)	**11.79**	**M10/M9b**	Chaisson and Pearson, 1997
FO *Globorotalia lenguaensis*	12.84	M9b	Turco et al., 2002
FO *Globorotalia* (*Fohsella*) *foshi robusta*	**13.13**	**M9b/M9a**	Chaisson and Pearson, 1997
FO *Globorotalia* (*Fohsella*) *fohsi* s.l.	**13.41**	**M9a/M8**	Chaisson and Pearson, 1997
FO *Globorotalia* (*Fohsella*) *praefohsi*	**13.77**	**M8/M7**	Turco et al., 2002
LO *Globorotalia* (*Fohsella*) *peripheroronda*	13.80	M7	Turco et al., 2002
LO *Clavatorella bermudezi*	13.82	M7	Shackleton et al., 1999
LO *Globorotalia archeomenardii*	13.87	M7	Turco et al., 2002
FO *Globorotalia* (*Fohsella*) *peripheroacuta*	**14.24**	**M7/M6**	Pearson and Chaisson, 1997
FO *Globorotalia praemenardii*	14.38	M6	Pearson and Chaisson, 1997

Table T5 (continued).

Event and species	Age (Ma)	Zone/Subzone (base)	Reference†
LO *Praeorbulina sicana*	14.53	M6	Shackleton et al., 1999
LO *Globigerinatella insueta*	14.66	M6	Pearson and Chaisson, 1997
FO *Orbulina suturalis*	**15.10**	**M6/M5b**	Shackleton et al., 1999

* = regional age only, † = references are available in Wade et al. (2011). LO = last occurrence, FO = first occurrence, X = change in coiling direction. Bold = zonal markers.

Table T6. Age estimates of planktonic foraminiferal datum events considered for Expedition 346.

Event and species	Berggren et al., 1985a and 1985b age (Ma)	Cande and Kent, 1992 age (Ma)	GTS2012 age (Ma)	Zone (Maiya, 1978)	References
X *Neogloboquadrina pachyderma* coiling change dextral to sinistral	0.37	0.37	0.38	PF9	Lyle et al., 1997
LO *Neogloboquadrina kagaensis*			0.7	PF7	Kucera and Kennett, 2000
FO Temporally high abundance of *Globorotalia inflata* (#1 bed)			**0.9–1.0**	**PF9/PF8**	**Miwa, 2014**
X *Neogloboquadrina pachyderma* coiling change sinistral to dextral			**1.14–1.24**	**PF8/PF7**	**Miwa, 2014**
FO *Neogloboquadrina humerosa*	1.1	1.2	1.22	PF7	Lyle et al., 1997
LO Temporally high abundance of *Globorotalia inflata* (#2 bed)			1.24–1.34	PF7	Miwa, 2014
FO *Globorotalia inflata*			1.46–1.67	PF7	Miwa, 2014
LO *Neogloboquadrina asanoi*			1.8	PF7	Motoyama et al., 2004
X *Neogloboquadrina pachyderma* coiling change dextral to sinistral			1.8	PF7	Miwa, 2014
X *Neogloboquadrina pachyderma* coiling change sinistral to dextral			2.22	PF7	Miwa, 2014
LO Temporally high abundance of *Globorotalia inflata praeinflata*			**2.5**	**PF7**	**Miwa, 2014**
FO *Globorotalia tosaensis*	3	3.1	3.09	PF7	Lyle et al., 1997
LO *Sphaeroidinellopsis* spp.	3.1	3.2	3.19	PF7	Lyle et al., 1997
FO Temporally high abundance of *Globorotalia inflata praeinflata* (#3 bed)			3.25	PF7/PF6	Miwa, 2014
FO *Globorotalia inflata praeinflata*	3.2	3.3	3.3	PF6	Lyle et al., 1997
FO *Neogloboquadrina asanoi*			4.2	PF6	Miwa, 2014
LO Temporally high abundance of *Globorotalia ikebei*			4.3	PF6	Miwa, 2014
FO *Neogloboquadrina acostaensis*	4	4.2	4.4	PF6	Lyle et al., 1997
X *Neogloboquadrina pachyderma* coiling change dextral to sinistral			4.7–4.8	PF6	Miwa, 2014
FO Temporally high abundance of *Globorotalia ikebei*			4.7–4.8	PF6	Miwa, 2014
LO *Globorotalia puncticulata*	4.4	4.6	4.789	PF6	Lyle et al., 1997
LO Barren of planktonic foraminifers			**5.3**	**PF6/PF5**	**Miwa, 2014**
FO Barren of planktonic foraminifers			**8.6**	**PF5/PF4**	**Miwa, 2014**
X *Neogloboquadrina pseudopachyderma* coiling change sinistral to dextral			**8.6**	**PF5/PF4**	**Miwa, 2014**
X *Neogloboquadrina pseudopachyderma* coiling change dextral to sinistral			11.6	PF4	Miwa, 2014
LO *Globorotalia rikuchuensis*			11.6	PF4	Miwa, 2014
FO *Neogloboquadrina pseudopachyderma*			**12.4**	**PF4/PF3**	**Miwa, 2014**
FO *Orbulina* spp.			**14.8**	**PF2/PF1**	**Shackleton et al., 1999**

FO = first occurrence, LO = last occurrence, X = changes in coiling direction. Bold = zonal markers.

Table T7. Taxonomic list for planktonic foraminiferal datums considered for Expedition 346. (Continued on next page.)

Species	Taxon author
Candeina nitida	(d'Orbigny, 1839)
Cassigerinella chipolensis	(Cushman and Ponton, 1932)
Clavatorella bermudezi	(Bolli, 1957); Blow, 1965
Dentoglobigerina altispira	(Cushman and Jarvis, 1936); Blow, 1979
Globigerina angustiumbilicata	Bolli, 1957
Globigerina bulloides	(d'Orbigny, 1826)
Globigerina praebulloides	Blow, 1959
Globigerina quinqueloba	Natland, 1938
Globigerinatella insueta	(Cushman and Stainforth, 1945)
Globigerinella calida	Parker, 1962
Globigerinoides conglobatus	(Brady, 1879)
Globigerinoides extremus	Bolli and Bermudez, 1965
Globigerinoides fistulosus	(Schubert, 1910); Kennett and Srinivasan, 1983
Globigerinoides ruber	(d'Orbigny, 1839)
Globigerinoides sicanus	De Stefani, 1950
Globigerinoides subquadratus	Brönimann, 1954
Globoquadrina dehiscens	(Chapman, Parr, and Collins, 1934); Finlay, 1947
Globoquadrina venezuelana	(Hedberg, 1937)
Globorotalia (*Fohsella*) *peripheroacuta*	Blow and Banner, 1966; Kennett and Srinivasan, 1983
Globorotalia (*Fohsella*) *peripheroronda*	Blow and Banner, 1966; Kennett and Srinivasan, 1983
Globorotalia (*Fohsella*) *praefohsi*	Blow and Banner, 1966; Kennett and Srinivasan, 1983
Globorotalia (*Fohsella*) *fohsi*	Cushman and Ellisor, 1939; Kennett and Srinivasan, 1983
Globorotalia (*Fohsella*) *foshi robusta*	Bolli, 1950; Kennett and Srinivasan, 1983
Globorotalia (*Hirsutella*) *cibaoensis*	Bermudez, 1949; Kennett and Srinivasan, 1983
Globorotalia (*Hirsutella*) *margaritae*	Bolli and Bermudez, 1965; Kennett and Srinivasan, 1983
Globorotalia (*Menardella*) *multicamerata*	Cushman and Jarvis, 1930; Kennett and Srinivasan, 1983
Globorotalia (*Truncorotalia*) *tosaensis*	Takayangi and Saito, 1962
Globorotalia (*Truncorotalia*) *truncatulinoides*	(d'Orbigny, 1839); Blow, 1969
Globorotalia archeomenardii	(Bolli, 1957)
Globorotalia cibaoensis	Bermudez, 1949
Globorotalia flexuosa	(Koch, 1923)
Globorotalia hessi	(Bolli and Premoli Silva, 1973)
Globorotalia hirsuta	(d'Orbigny, 1839)
Globorotalia ikebei	(Maiya et al., 1976)
Globorotalia inflata	(d'Orbigny,1839)
Globorotalia inflata praeinflata	(Maiya et al., 1976)
Globorotalia juanai	Bermudez and Bolli, 1969
Globorotalia lenguaensis	(Bolli, 1957)
Globorotalia limbata	(Fornasini, 1902, as *Rotalia*)
Globorotalia miozea conoidea	Walters, 1965
Globorotalia miozea miozea	Finlay, 1939
Globorotalia orientalis	(Maiya et al., 1976)
Globorotalia pertenuis	(Beard, 1969)
Globorotalia plesiotumida	(Blow and Banner, 1965)
Globorotalia praemenardii	(Cushman and Stainforth, 1945)
Globorotalia pseudomiocenica	Bolli and Bermudez, 1965
Globorotalia quinifalcata	Saito and Maiya, 1973
Globorotalia rikuchuensis	Takayanagi and Oba, 1966
Globorotalia tumida	(Brady 1877); Banner and Blow, 1960
Globoturborotalita apertura	Cushman, 1918
Globoturborotalita decoraperta	(Takayangi and Saito, 1962); Chaisson and Pearson, 1997
Globoturborotalita nepenthes	(Todd, 1957); Hofker, 1977
Globoturborotalita obliquus	Bolli, 1957
Globoturborotalita woodi	(Jenkins, 1960); Hofker, 1977
Neogloboquadrina acostaensis	(Blow, 1959); Kennett and Srinivasan, 1983
Neogloboquadrina asanoi	(Maiya et al., 1976)
Neogloboquadrina dutertrei	(d'Orbigny, 1839)
Neogloboquadrina himiensis	(Maiya et al., 1976)
Neogloboquadrina humerosa	(Gervais, 1996)
Neogloboquadrina incompta	(Ciefelli, 1961)
Neogloboquadrina kagaensis	(Maiya et al., 1976)
Neogloboquadrina pachyderma (d)	(Ehrenberg, 1861)
Neogloboquadrina pachyderma (s)	(Ehrenberg, 1861)
Neogloboquadrina pseudopachyderma	(Cita and Premoli Silva, 1965)
Orblina universa	(d'Orbigny, 1839)
Orbulina suturalis	Brönnimann, 1951
Paragloborotalia mayeri	(Cushman and Ellisor, 1939); Spezzaferri, 1991
Praeorbulina circularis	(Blow, 1956)

Table T7 (continued).

Species	Taxon author
Praeorbulina sicana	(de Stefani, 1952); Jenkins, 1981
Pulleniatina obliquiloculata	(Parker and Jones, 1865)
Pulleniatina primalis	(Parker and Jones, 1865)
Pulleniatina spectabilis	(Parker, 1965)
Sphaerodinellopsis kochi	(Caudri, 1934)
Sphaeroidinella dehiscens	(Parker and Jones, 1865); Banner and Blow, 1960
Sphaeroidinellopsis seminulina	(Schwager, 1866); Banner and Blow, 1970
Turborotalita humilis	(Brady, 1884); Banner and Blow, 1962

Globorotalia pseudomiocenica has been maintained as per Bolli and Saunders (1985), rather than being assigned to the *Globorotalia* subgenus *Menardella*, because Kennett and Srinivasan (1983) regarded this species as a junior synonym of *G.* (*Menardella*) *limbata* and so did not formally place this species in the subgenus *Menardella*.

Table T8. Taxonomic list for benthic foraminifers including source references considered for Expedition 346. (Continued on next page.)

Benthic foraminifers	Taxon author	Reference
Agglutinated		
Ammobaculites agglutinans	(d'Orbigny, 1846)	Hanagata, 2003
Ammodiscus anguillae	Høglund, 1947	Jones, 1994
Cribrostomoides subglobosus	(Cushman, 1910)	Jones, 1994
Eggerella bradyi	(Cushman, 1911)	Holbourn et al., 2013
Glomospira charoides	(Jones and Parker, 1860)	Holbourn et al., 2013
Haplophragmoides sphaeriloculum	Cushman, 1910	Jones, 1994
Hyperammina elongata	Brady, 1878	Hanagata, 2003
Karreriella baccata japonica	Asano, 1938	Kato, 1992
Karrerulina coniformis	(Gryzbowski, 1898)	Hanagata, 2003
Karrerulina conversa	(Gryzbowski, 1901)	Hanagata, 2003
Lagenammina compressa	Cushman and McCulloch, 1939	Hanagata, 2003
Martinottiella communis	(d'Orbigny, 1826)	Holbourn et al., 2013
Miliammina echigoensis	Asano and Inomata, 1952	Kato, 1992; Hanagata et al., 2001
Paratrochammina challengeri	Brönimann and Whittaker, 1988	Jones, 1994
Reophax scorpiusus	de Montfort, 1808	Jones, 1994
Reophax spiculifer	Brady, 1879	Jones, 1994
Sigmoilopsis schlumbergeri	(Silvestri, 1904)	Kato, 1992
Spirosigmoilinella compressa	Matsunaga, 1955	Kato, 1992; Hanagata et al., 2001
Calcareous hyaline		
Amphicoryna scalaris	(Batsch, 1791)	Holbourn et al., 2013
Ammonia takanabensis	(Ishizaki, 1948)	
Asterorotalia gaimardii	(d'Orbigny, 1906)	Hoiles et al., 2012
Bolivina decussata	Brady, 1881	Holbourn et al., 2013
Bolivina pacifica	Cushman and McCulloch, 1942	Kato, 1992; Usami et al., 2013
Bolivina robusta	Brady, 1881	Hanagata, 2003
Bolivina subspinescens	Cushman, 1922	van Marle, 1991
Bolivinita quadrilatera	(Schwager, 1866)	Holbourn et al., 2013
Brizalina alata	(Seguenza, 1862)	Jones, 1994
Brizalina pacifica	(Cushman and McCullough, 1942)	Usami et al., 2013
Bulimina aculeata	d'Orbigny, 1826	Holbourn et al., 2013
Bulimina marginata	d'Orbigny, 1826	Holbourn et al., 2013
Buliminia mexicana	(Cushman, 1922)	Holbourn et al., 2013
Cassidulina japonica	Asano and Nakamura, 1937	Kato, 1992
Cassidulina laevigata	d'Orbigny, 1826	Holbourn et al., 2013
Cassidulina norvangi	Thalmann, 1950	Kato, 1992
Cassidulina norcrossi	(Cushman, 1933)	Usami et al., 2013
Cassidulinoides tenuis	Phleger and Parker, 1951	Kato, 1992
Chilostomella oolina	Schwager, 1878	Holbourn et al., 2013
Cibicidoides lobatulus	(Walker and Jacob, 1798)	Holbourn et al., 2013
Cibicidoides pachyderma	Rzehak, 1886	Holbourn et al., 2013
Cibicidoides refulgens	de Monfort, 1808	Holbourn et al., 2013
Cibicidoides mundulus	(Brady, Parker, and Jones, 1888)	Holbourn et al., 2013
Cibicidoides robertsonianus	(Brady, 1881)	Holbourn et al., 2013
Discorbinella berthelotti	d'Orbigny, 1839	Jones, 1994
Epistominella exigua	(Brady, 1884)	Holbourn et al., 2013
Epistominella pulchella	Husezima and Maruhasi, 1944	Kato, 1992
Eubuliminella exilis	(Brady, 1884)	Holbourn et al., 2013
Fursenkoina bradyi	(Cushman, 1922)	Jones, 1994
Fursenkoina seminuda	(Natland, 1938)	Brunner, 1992
Gavelinopsis lobatulus	(Parr, 1950)	van Marle, 1991
Glandulina laevigata	(d'Orbigny, 1826)	Kato, 1992
Globobulimina pacifica	Cushman, 1927	Holbourn et al., 2013
Globobulimina pupoides	(d'Orbigny, 1846)	Hanagata, 2003
Globobulimina spinescens	Brady, 1884	Kato, 1992
Globocassidulina subglobosa	(Brady, 1881)	Holbourn et al., 2013
Gyroidinoides nitidus	(Reuss, 1851)	Brunner, 1992
Gyroidinoides orbicularis	(d'Orbigny, 1826)	Brunner, 1992
Hoeglundina elegans	(d'Orbigny, 1826)	Holbourn et al., 2013
Hyalinea balthica	(Schroeter, 1783)	Holbourn et al., 2013
Melonis barleeanus	Williamson, 1858	Mohan et al., 2011
Melonis pompilioides	(Fichtel and Moll, 1798)	Holbourn et al., 2013
Neolenticulina peregrina	(Schwager, 1866)	Holbourn et al., 2013
Nonion japonicum	Asano, 1938	Kato, 1992
Nonionella globosa	Ishiwada, 1950	Kato, 1992
Nonionella turgida	(Williamson, 1958)	Holbourn et al., 2013
Nonionellina labradorica	(Dawson, 1860)	Holbourn et al., 2013
Oridorsalis umbonatus	(Reuss, 1851)	Holbourn et al., 2013

Table T8 (continued).

Benthic foraminifers	Taxon author	Reference
Orthomorphina challengeriana	(Thalmann, 1937)	Jones, 1994
Planulina wuellerstorfi	(Schwager, 1866)	Holbourn et al., 2013
Planularia australis	(Chapman, 1915)	Jones, 1994
Pleurostomella brevis	Schwager, 1866	Holbourn et al., 2013
Procerolagena gracillima	(Sequenza, 1862)	Jones, 1994
Pullenia bulloides	(d'Orbigny, 1846)	Holbourn et al., 2013
Pullenia quinqueloba	(Reuss, 1851)	Holbourn et al., 2013
Robertinoides bradyi	Cushman and Parker, 1936	Jones, 1994
Sphaeroidina bulloides	d'Orbigny, 1826	Holbourn et al., 2013
Stilostomella abyssorum	(Brady, 1884)	Holbourn et al., 2013
Trifarina angulosa	(Williamson, 1858)	Holbourn et al., 2013
Trifarina bradyi	Cushman, 1927	Holbourn et al., 2013
Uvigerina havanensis	Cushman and Bermúdez, 1936	Holbourn et al., 2013
Uvigerina hispida	Schwager, 1866	Holbourn et al., 2013
Uvigerina peregrina	Cushman, 1923	Boersma, 1984
Uvigerina proboscidea	Schwager, 1866	Holbourn et al., 2013
Uvigerina yabei	Asano, 1938	Kato, 1992
Valvulineria sadonica	Asano, 1951	Kato, 1992
Porcellaneous		
Pyrgo lucernula	(Schwager, 1866)	Holbourn et al., 2013
Pyrgo murrhina	(Schwager, 1866)	Holbourn et al., 2013
Pyrgo serrata	(Bailey, 1861)	Holbourn et al., 2013
Quinqueloculina akneriana	d'Orbigny, 1846	Brunner, 1992
Triloculina tricarinata	d'Orbigny, 1826	Holbourn et al., 2013
Triloculina trigonula	(Lamarck, 1804)	Holbourn et al., 2013

Table T9. Interstitial water analyses and budget, Expedition 346.

Analytes	Method	Model of instrument	IW volume (mL)	Priority
Salinity	Digital refractometer	Index Instruments Ltd.	0.1	H
pH	Gran titration	Brinkman pH electrode Metrohm 794 basic Titrino autotitrator	3	H
Alkalinity				
Cl^-	Titration against silver nitrate	Metrohm 785 DMP Titrino autotitrator	0.1	H
SO_4^{2-}	Ion chromatography	Metrohm 850 professional ion chromatograph	0.1	H
Br^-				
Cl^-				
Ca	ICP-AES/Ion chromatography	Teledyne Prodigy high-dispersion ICP-AES/Metrohm 850 professional ion chromatograph	4	H
K				
Mg				
Na				
Ba	ICP-AES	Teledyne Prodigy high-dispersion ICP-AES		
B				
Fe				
Li				
Mn				
Si				
Sr				
NH_4^+	Spectrophotometry	Agilent Cary 100 UV-VIS spectrophotometer	3	H
PO_4^{3-}				
$H_4SiO_4^-$				
HS^-			1	H*
Yellowness			1	H*
Isotopes (Mg, K, Ca)	Shore-based water requirements		5	M
$\delta^{34}S$			5	M
$\delta^{13}C$			5	M
Archive IW			5	L

ICP-AES = inductively coupled plasma–atomic emission spectroscopy. IW = interstitial water. UV-VIS = ultraviolet-visible. H = high priority, H* = high priority in shallow sediment of gas-rich sequences, M = medium priority, L = low priority.

Table T10. Approximate chemical composition of reference seawater and inferred Japan Sea Proper Water, Expedition 346.

Species (i)	Reference SW (S = 35.0)			Japan Sea Proper Water (S = 34.06)		
	x_i (mmol/kg_{sw})	m_i (mmol/kg_{wat})	M_i (mol/L_{sw})	x_i (mmol/kg_{sw})	m_i (mmol/kg_{wat})	M_i (mol/L_{sw})
Na^+	469.0	486.1	481.2	456.4	473.0	467.9
Mg^{2+}	52.82	54.74	54.19	51.40	53.27	52.70
Ca^{2+}	10.28	10.66	10.55	10.01	10.37	10.26
K^+	10.21	10.58	10.47	9.93	10.30	10.18
Sr^{2+}	0.0907	0.0940	0.0931	0.0883	0.0915	0.0905
Cl^-	545.9	565.8	560.1	531.3	550.6	544.7
SO_4^{2-}	28.24	29.26	28.97	27.48	28.48	28.17
DIC	1.96	2.03	2.01			
Br^-	0.842	0.873	0.864	0.819	0.849	0.840
ΣB	0.4151	0.4303	0.4259			

Reference seawater (SW) composition (Millero et al., 2008). Japan Sea Proper Water salinity (S) = 34.06 (Sudo, 1986). Japan Sea Proper Water total alkalinity = 2.37 and dissolved inorganic carbon (DIC) = 2.30 (Chen et al., 2005). Blank cells = not applicable.

Table T11. Geomagnetic polarity timescale used during Expedition 346.

Geological age	Base age (Ma)	Chron	Subchron	Age top (Ma)	Age base (Ma)	Duration (m.y.)	Remarks
Neogene							
Holocene	11.5 ka						
Pleistocene		C1	C1n (Brunhes)	0	0.781	0.781	Base of middle Pleistocene (Ionian) is base of Brunhes Chron
Late (Tarantian)	0.126		C1r.1r (Matuyama)	0.781	0.988	0.207	
Middle (Ionian)	0.781		C1r.1n (Jaramillo)	0.988	1.072	0.084	
			C1r.2r	1.072	1.173	0.101	
			C1r.2n (Cobb Mountain)	1.173	1.185	0.012	Cobb Mountain cryptochron is within early part of Matuyama (C1r) Chron
			C1r.3r	1.185	1.778	0.593	
Early (Calabrian)	1.806	C2	C2n (Olduvai)	1.778	1.945	0.167	Base of Calabrian is in lower part of Olduvai Chron
			C2r.1r	1.945	2.128	0.183	
			C2r.1n (Reunion)	2.128	2.148	0.020	
			C2r.2r (Matuyama)	2.148	2.581	0.433	Base of Pleistocene is near base of Matuyama Chron
(Gelasian)	2.588						
Pliocene		C2A	C2An.1n (Gauss)	2.581	3.032	0.451	"Gauss Normal Chron" (C2An) contains two reversed intervals: Kaena (2An.1r) and Mammoth (2An.2r)
			C2An.1r (Kaena)	3.032	3.116	0.084	
			C2An.2n	3.116	3.207	0.091	
			C2An.2r (Mammoth)	3.207	3.330	0.123	
Late (Piacenzian)	3.600		C2An.3n (Gauss)	3.330	3.596	0.266	Base of Piacenzian is base of Chron C2An.3n
			C2Ar (Gilbert)	3.596	4.187	0.591	"Gilbert Reversed Chron" spans Chrons C2Ar through C3r
		C3	C3n.1n (Cochiti)	4.187	4.300	0.113	
			C3n.1r	4.300	4.493	0.193	
			C3n.2n (Nunivak)	4.493	4.631	0.138	
			C3n.2r	4.631	4.799	0.168	
			C3n.3n (Sidufjall)	4.799	4.896	0.097	
			C3n.3r	4.896	4.997	0.101	
Early (Zanclean)	5.332		C3n.4n (Thvera)	4.997	5.235	0.238	Base of Miocene is in uppermost Chron C3r
Miocene			C3r (Gilbert)	5.235	6.033	0.798	
		C3A	C3An.1n	6.033	6.252	0.219	
			C3An.1r	6.252	6.436	0.184	
			C3An.2n	6.436	6.733	0.297	
			C3Ar	6.733	7.140	0.407	
		C3B	C3Bn	7.140	7.212	0.072	
Late (Messinian)	7.246		C3Br.1r	7.212	7.251	0.039	Base of Messinian is in lowermost Chron C3Br.1r
			C3Br.1n	7.251	7.285	0.034	
			C3Br.2r	7.285	7.454	0.169	
			C3Br.2n	7.454	7.489	0.035	
			C3Br.3r	7.489	7.528	0.039	
		C4	C4n.1n	7.528	7.642	0.114	
			C4n.1r	7.642	7.695	0.053	
			C4n.2n	7.695	8.108	0.413	

Table T12. Downhole measurements made by wireline tool strings, Expedition 346.

Tool string	Tool	Measurement	Sampling interval (cm)	Approximate vertical resolution (cm)
Paleo combo	EDTC	Total gamma ray	5 and 15	30
	HRLA	Resistivity	15	30
	HNGS	Spectral gamma ray	15	20–30
	HLDS	Bulk density and caliper	2.5 and 15	38
	MSS	Magnetic susceptibility	4	12–36
Formation MicroScanner-sonic	EDTC	Total gamma ray	5 and 15	30
	GPIT	Tool orientation and acceleration	3.8	15
	DSI	Acoustic velocity	15	107
	FMS	Microresistivity and caliper	0.25	1

All tool and tool string names, except the MSS, are trademarks of Schlumberger. For definitions of tool acronyms, see Table T13.

Table T13. Acronyms and units used for downhole wireline tools and measurements, Expedition 346.

Tool	Output	Description	Unit
EDTC		Enhanced digital telemetry cartridge	
	GR	Total gamma ray	gAPI
	ECGR	Environmentally corrected gamma ray	gAPI
	EHGR	High-resolution environmentally corrected gamma ray	gAPI
HNGS		Hostile Environment Natural Gamma Ray Sonde	
	HSGR	Standard (total) gamma ray	gAPI
	HCGR	Computed gamma ray (HSGR minus uranium contribution)	gAPI
	HFK	Potassium	wt%
	HTHO	Thorium	ppm
	HURA	Uranium	ppm
HLDS		Hostile Environment Litho-Density Sonde	
	RHOM	Bulk density	g/cm^3
	PEFL	Photoelectric effect	barn/e^-
	LCAL	Caliper (measure of borehole diameter)	Inch
	DRH	Bulk density correction	g/cm^3
HRLA		High-Resolution Laterolog Array	
	RLA1-5	Apparent resistivity from computed focusing Mode 1–5	Ωm
	RT	True resistivity	Ωm
	MRES	Borehole fluid resistivity	Ωm
MSS		Magnetic Susceptibility Sonde	
	LSUS	Magnetic susceptibility, deep reading	Uncalibrated units
	HSUS	Magnetic susceptibility, high resolution	Uncalibrated units
FMS		Formation MicroScanner	
	C1, C2	Orthogonal hole diameters	Inch
	P1AZ	Pad 1 azimuth	°
		Spatially oriented resistivity images of borehole wall	
GPIT		General Purpose Inclinometry Tool	
	DEVI	Hole deviation	°
	HAZI	Hole azimuth	°
	F*x*, F*y*, F*z*	Earth's magnetic field (three orthogonal components)	°
	A*x*, A*y*, A*z*	Acceleration (three orthogonal components)	m/s^2
DSI		Dipole Shear Sonic Imager	
	DTCO	Compressional wave slowness	µs/ft
	DTSM	Shear wave slowness	µs/ft
	DT1	Shear wave slowness, lower dipole	µs/ft
	DT2	Shear wave slowness, upper dipole	µs/ft

For the complete list of acronyms used in IODP and for additional information about tool physics, consult IODP-USIO Science Services, LDEO, at **iodp.ldeo.columbia.edu/TOOLS_LABS/tools.html.**